Double Spin Asymmetries in Single Hadron Quasi-Real Photoproduction at HERMES

Diplomarbeit

Patricia Liebing
Humboldt-Universität zu Berlin
Institut für Physik

Accomplished at DESY, IfH Zeuthen

January 8, 2001

Contents

Introduction 4

1 Theoretical Aspects 6

1.1 Polarized Deep Inelastic Scattering 6

1.1.1 The Inclusive Cross Section 6

1.1.2 Decomposition of the Nucleon Spin 8

1.1.3 Semi-inclusive Measurements 9

1.2 Ways to Measure the Gluon Polarization 9

1.2.1 Q^2 Evolution of the Polarized Structure Functions 9

1.2.2 Photon-Gluon Fusion and Charm Production 10

1.2.3 Photoproduction of High-p_T Hadrons 11

2 The HERMES Experiment 16

2.1 The Positron Beam 16

2.2 The Internal Gas Target 16

2.3 The Spectrometer 17

2.3.1 The Spectrometer Magnet 19

2.3.2 The Tracking Devices 19

2.3.3 The Particle Identification Devices 19

2.3.4 The Luminosity Monitor 20

2.4 Data Acquisition System (DAQ) and Software 20

3 Analysis on Double Spin Asymmetries 22

3.1 Data Quality 22

3.1.1 Data Quality Cuts 22

3.1.2 Experimental Conditions 23

3.2 Track Selection and Tracking Method 27

3.2.1 Kinematic Cuts 27

3.2.2 Comparison of Different Tracking Methods 29

3.3 Results for the 1996 and 1997 Hadron Asymmetries 29

3.3.1 Asymmetries and Kinematic Correlations 29

3.3.2 Systematic Errors and Normalization Uncertainty 33

3.4 Systematic Studies on the 1996 and 1997 Asymmetries 34

3.4.1 Effects of the Experimental Environment on $A_{\|}$ 34

3.4.2 Flux Correction to the PID Detector Likelihoods 36
3.4.3 PID Cut Efficiency and Positron Contamination 39
3.4.4 PID Detector Responses 40
3.4.5 Merging of the Hadron Asymmetries 45

4 Results and Interpretation **50**
4.1 Further Studies on the Charged Hadron Asymmetries 50
4.1.1 Invariant Mass 51
4.1.2 Sensitive Kinematic Regions of the Asymmetries 51
4.1.3 Q^2 dependence of the Asymmetries 55
4.2 Comparison of the Data with Different Theoretical Models 56
4.2.1 Theoretical Calculations 56
4.2.2 Monte Carlo Simulations 58

Summary and Outlook **63**

Bibliography **64**

Introduction

Over the last decades, deep inelastic lepton-nucleon scattering (DIS) has proved to be a successful experimental technique to probe the internal structure of the nucleon. The kinematic region which defines the DIS regime is that of large momentum and energy transfer to the nucleon by the exchanged virtual photon. These are needed to break up the nucleon so that its internal constituents can be resolved. In this region, the momentum and the spin distribution of the electrically charged constituents of the nucleon, the quarks, can be described by unpolarized and polarized structure functions, respectively. With inclusive unpolarized DIS it has been established that only about 50% of the nucleon momentum is being carried by the quarks [Hal84]. The remaining nucleon momentum can be assigned to gluons as has been confirmed experimentally [Bra80].
The polarized structure functions can be accessed by experiments like HERMES using a polarized beam and a polarized target. The inclusive measurements of polarized DIS showed that the polarization of the quarks can only account for a fraction of 30% to 50% of the nucleon spin [Vet98]. In contrast to the unpolarized case, not only the polarization of the gluons can contribute to the spin of the nucleon but also the orbital angular momenta of quarks and gluons. As an important step to understand the spin composition of the nucleon it is essential to determine the gluon polarization.

In the unpolarized case the scaling violation of the unpolarized structure functions has been used to measure the gluon density. 'Scaling violation' refers to the dependence of the structure functions on the virtuality of the photon. It is not possible yet to do the same for the *polarized* structure functions to infer the gluon polarization by such an indirect method. With the data presently available there will be almost no constraints to even predict the sign of the gluon polarization [Geh96], not even speaking about its shape.
A more direct approach would be to select subprocesses sensitive to strong (QCD) interactions and thus give access to the gluonic part of the nucleon structure. This has proven successful in the unpolarized case. There are several methods to isolate these subprocesses, especially Photon-Gluon Fusion (PGF). To measure spin asymmetries of charmed hadrons or J/ψ's would be one possibility. Also pairs of light charged hadrons with high transverse momentum p_T can be produced in subprocesses sensitive to the gluon polarization. To some extent, also the detection of inclusive single, high-p_T hadrons can provide access to QCD subprocesses.

These processes are presently studied at HERMES in quasi-real photoproduction, where the relevant scale characterizing them is not the virtuality of the photon anymore but rather the transverse momentum in the QCD subprocess. This introduces some difficulties. The more technical problem is that the scattered lepton stays undetected in the beam pipe, so that the precise information on the kinematics of the event is lost. The theoretical problem is that for a photon with low virtuality it is more likely that it will fluctuate into a virtual vector meson or a quark-antiquark pair which can then interact hadronically with the partons of the nucleon. The hard QCD subprocesses cannot be uniquely identified. Rather one has to consider a mixture of subprocesses contributing to the cross section. In order to resolve the contributions of different QCD subprocesses to the total cross section a correct model of the internal structure of the photon and of the hadronic cross section is required. First results on double spin asymmetries in the quasi-real photoproduction of

high-p_T hadron pairs have recently been published by HERMES [Air00].

The subject of this thesis is the analysis of single high-p_T hadrons in the quasi-real photoproduction regime and the extraction of double spin asymmetries as a function of p_T and p for positive and negative hadrons separately. The main part of the analysis consists of systematic and stability checks on the asymmetries. The results of these studies are presented in Chapter 3. Chapter 2 outlines the main features of the HERMES experiment.
Monte Carlo studies need to be performed in order to find the photon-proton interaction model which best describes the data. As HERMES is a fixed target experiment this is a nontrivial task because its center of mass energy is too low to allow for mostly perturbative calculations. First results of the Monte Carlo studies are shown in Chapter 4. The underlying theoretical model is described in Chapter 1.

Chapter 1

Theoretical Aspects

1.1 Polarized Deep Inelastic Scattering

1.1.1 The Inclusive Cross Section

Deep inelastic scattering (DIS) can be used to investigate the structure of the nucleon. A pointlike probe, such as an electron or a positron, interacts with constituents (quarks) of the nucleon by exchanging a virtual photon. Also muons or neutrinos can be used as probes. The quark absorbs

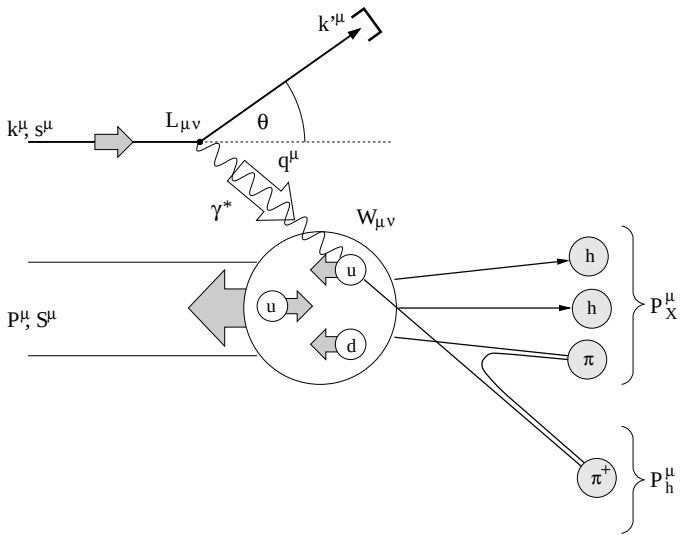

Figure 1.1: Sketch of the deep inelastic scattering process as seen in the laboratory system. The big arrows indicate the spins of the particles.

the virtual photon, the nucleon breaks up and the struck quark and the target remnant fragment into hadrons (figure 1.1). In inclusive DIS only the lepton is detected in the final state. Its energy and momentum determine the kinematics of the event. The following variables are used for the description of DIS processes:

$(E, \vec{k})$	four momentum vector of the incoming lepton
$(E', \vec{k'})$	four momentum vector of the outgoing lepton
$\nu = E - E'$	energy transfer to the virtual photon
$q = k - k'$	four momentum transfer to the virtual photon
$Q^2 = -q^2 \stackrel{\text{lab}}{\simeq} 4EE' \sin^2 \frac{\theta^2}{2}$	virtuality of the photon, θ = lepton scattering angle in the lab frame
$y = \frac{p \cdot q}{p \cdot k} \stackrel{\text{lab}}{=} \frac{\nu}{E}$	fractional energy transfer to the nucleon
$x = \frac{-q^2}{2p \cdot q} \stackrel{\text{lab}}{=} \frac{Q^2}{2M\nu}$	Bjorken scaling variable, fraction of the nucleon momentum carried by the struck quark
$W^2 = (p+q)^2 \stackrel{\text{lab}}{=} M_p^2 + 2M_p\nu - Q^2$	energy in the photon-nucleon center-of-mass system
$z = \frac{p \cdot p_h}{p \cdot q} \stackrel{\text{lab}}{=} \frac{E_h}{\nu}$	fraction of the virtual photon energy carried by a hadron h
$p_{\parallel} = \frac{\vec{p}_h \cdot \vec{q}}{\lvert\vec{q}\rvert}$	longitudinal momentum of a hadron h in the $\gamma^* - N$ center-of-mass system
$x_F = \frac{2p_{\parallel}}{W}$	Feynman scaling variable, scaled longitudinal momentum of a hadron h

The cross section may be expressed as a product of the leptonic tensor $L_{\mu\nu}$ and the hadronic tensor $W^{\mu\nu}$:

$$\frac{d^2\sigma}{d\Omega dE'} = \frac{\alpha^2}{2M_p Q^4} \frac{E'}{E} L_{\mu\nu} W^{\mu\nu} \tag{1.1}$$

$L_{\mu\nu}$ can be calculated exactly from QED, it describes the emission of a virtual photon by the pointlike lepton. $W^{\mu\nu}$ on the other hand describes the absorption of the virtual photon by the nucleon, therefore it must contain all the information concerning the structure of the nucleon. This tensor is unknown. Symmetry considerations and conservation laws reduce the most general $W^{\mu\nu}$ to a form where it can be parametrized by four independent structure functions F_1, F_2, g_1 and g_2. The structure functions F_1 and F_2 are spin independent whereas g_1 and g_2 only contribute to the cross section if both the beam and the target are polarized. In general these functions depend on ν and Q^2, but if the scattering occurs off pointlike constituents, they only depend on the momentum fraction x of those constituents. This is called the 'scaling' behavior of the structure functions. In the so-called 'naive' quark-parton model (QPM), F_1 is the sum of the charge weighted quark distributions in the nucleon:

$$F_1(x) = \frac{1}{2} \sum_f e_f^2 q_f(x). \tag{1.2}$$

The sum runs over all quarks and antiquarks with flavor f. For spin 1/2 particles F_2 is related to F_1 by the Callan-Cross-Relation: $F_2 = 2xF_1$. The polarized structure function g_1 can be interpreted as the charge weighted difference between the distribution functions $q(x)$ of quarks with spin parallel (q_f^+) and that with spin antiparallel (q_f^-) to the nucleon spin at a given x:

$$g_1(x) = \frac{1}{2} \sum_f e_f^2 \left(q_f^+(x) - q_f^-(x) \right) \equiv \frac{1}{2} \sum_f e_f^2 \Delta q(x). \tag{1.3}$$

In the naive QPM, $g_2 \simeq 0$ because it describes transverse degrees of freedom which do not exist in this model. Figure 1.2 shows how g_1 can be sensitive to the quark spin. The incoming lepton emits a circularly polarized, or 'transverse', virtual photon with helicity ± 1. The polarization of the incoming lepton beam transfers to that of the photons with a depolarization factor $D(y, Q^2)$, which takes into account the loss of polarization from the lepton to the virtual photon in this process. A photon can only be absorbed by a quark which has a spin projection opposite to its own because the final state must still be a quark with spin 1/2. If the nucleon spin is opposite

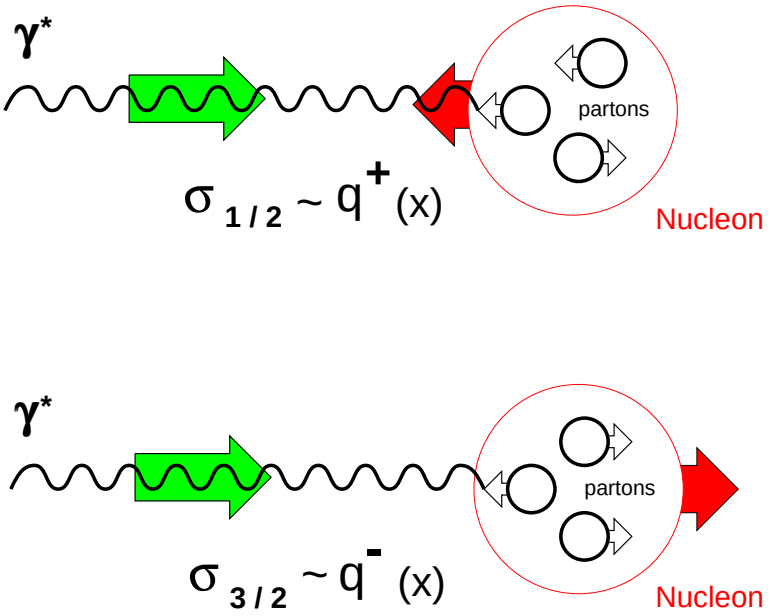

Figure 1.2: The simple QPM explanation of the sensitivity of polarized DIS to the polarized quark distributions.

to that of the lepton, the quark spin must be parallel to that of the nucleon. Thus by measuring the cross section for beam and target spin antiparallel, $\sigma^{\rightleftarrows}$, one is sensitive to q^+. If target and beam spins are parallel to each other, $(\sigma^{\rightrightarrows})$, one measures the distribution of quarks q^- with spin orientation antiparallel to the nucleon spin. The spin structure function g_1 can then be deduced from the polarization asymmetry [Vet98]:

$$A_{\parallel} = \frac{\sigma^{\rightleftarrows} - \sigma^{\rightrightarrows}}{\sigma^{\rightleftarrows} + \sigma^{\rightrightarrows}} \simeq D\frac{g_1}{F_1}. \tag{1.4}$$

1.1.2 Decomposition of the Nucleon Spin

The QPM is formulated in a frame, where the nucleon moves with infinite momentum. The quarks inside the nucleon are massless, non-interacting and their transverse momenta are neglected. In a non-relativistic model all the spin of the nucleon or, more precisely, its helicity ($S_z = 1/2$) comes from the valence and sea quarks, i.e.

$$\frac{1}{2} = \frac{1}{2}\Delta\Sigma = \frac{1}{2}\left(\Delta q_v + \Delta q_s\right). \tag{1.5}$$

In a *relativistic* QPM the expectation for $\Delta\Sigma$ is about 0.6. Global fits to the world data on g_1 led to $\Delta\Sigma \approx 0.2 - 0.3$, only about 50% of the expected value. If interactions between quarks are allowed in the QCD-inspired QPM, the helicity of the nucleon will be composed of several components:

$$\frac{1}{2} = \frac{1}{2}\Delta\Sigma + \Delta G + L_z, \tag{1.6}$$

where ΔG denotes the gluon contribution and L_z is the orbital angular momentum carried by quarks and gluons. Inclusive and semi-inclusive DIS have only been used to measure $\Delta\Sigma$ so far. It has been proposed that DIS measurements of azimuthal hadron asymmetries in the exclusive limit or in Deeply Virtual Compton Scattering (DVCS) may be sensitive to the quark angular momentum. For the determination of ΔG one can select other processes than DIS that directly probe the photon-gluon interaction, or infer ΔG indirectly from the measured scaling violations of g_1.

1.1.3 Semi-inclusive Measurements

Besides the scattered lepton modern DIS experiments can also detect the produced hadrons. In a so-called semi-inclusive analysis a hadron of a given type and charge can provide information about the flavor of the struck quark. The quark from the hard scattering process fragments into a hadron before leaving the nucleon. For instance, if a π^+ ($|u\bar{d}\rangle$) is detected, it is likely to contain the struck u quark. Because of the factor e_q^2 in the cross section and the u quark dominance in the proton ($|uud\rangle$), most of the (charged) hadrons produced in HERMES are π^+. The cross section for semi-inclusive DIS, normalized to the total inclusive DIS cross section σ^{tot}, in the QPM is:

$$\frac{1}{\sigma^{tot}}\frac{d\sigma^h(x,Q^2,z)}{dz} = \frac{\sum_f e_{q_f}^2 q_f(x,Q^2) D_{q_f}^h(z,Q^2)}{\sum_f e_{q_f}^2 q_f(x,Q^2)}. \tag{1.7}$$

The fragmentation functions $D_{q_f}^h$ represent the probability that a hadron h is produced if a quark q_f is struck. The fragmentation functions depend on z, the energy fraction carried by the hadron, but not primarily on the kinematics of the inclusive scattering process itself. If QCD corrections to lowest order DIS processes are considered, the quark structure functions as well as the fragmentation functions become logarithmically dependent on Q^2.
In polarized DIS, the semi-inclusive asymmetries can be expressed as:

$$A_{\parallel}^h = D\frac{\sum_f e_{q_f}^2 \Delta q_f(x,Q^2) D_{q_f}^h(z,Q^2)}{\sum_{f'} e_{q_{f'}}^2 q_{f'}(x,Q^2)}, \tag{1.8}$$

which gives access to the helicity dependent parton distributions $\Delta q(x)$ for each individual quark flavor.

1.2 Ways to Measure the Gluon Polarization

If the QPM is extended within the framework of QCD, the quarks can interact via gluon exchange. This induces the scaling violations in the structure functions, because e.g. the quark distributions at a given x are now not only made up of quarks with that momentum fraction but also of virtual quark-antiquark pairs which have been produced from a gluon with a momentum fraction $x' > x$. How many of them are 'visible', depends on the resolution given by Q^2 (in the infinite momentum frame and using the quantum mechanical uncertainty relation $\Delta\lambda\Delta q \geq 1$, the resolution is $1/\lambda = \sqrt{Q^2}$). In lowest order (LO) QCD three processes contribute to the evolution of the parton distributions:

1. A quark q can radiate a gluon g, leaving a quark and a gluon with lower momenta.
2. A gluon can create a quark-antiquark pair.
3. A gluon can create a pair of gluons.

The probability that a parton i in the final state with momentum fraction x originates from a parton j in the initial state with momentum fraction x' is proportional to $\alpha_s(Q^2)P_{ij}$, where the P_{ij} are the so called splitting functions. They depend on the ratio $\frac{x}{x'}$. The Q^2 evolution of the parton distributions to each other is described by the DGLAP (Dockshitzer-Gribov-Lipatov-Altarelli-Parisi) evolution equations [Hal84].

1.2.1 Q^2 Evolution of the Polarized Structure Functions

For the polarized parton distributions the splitting functions are replaced by helicity dependent kernels $P_{i\pm j\pm}$, where $\pm$ denote the helicities of the partons. The spin dependent DGLAP equations

are:

$$\frac{d\Delta q_f(x,Q^2)}{d\ln Q^2} = \frac{\alpha_s(Q^2)}{2\pi}\int_x^1 \frac{dx'}{x'}\left(\Delta q_f(x',Q^2)\Delta P_{qq}\left(\frac{x}{x'}\right)+\Delta G(x',Q^2)\Delta P_{qg}\left(\frac{x}{x'}\right)\right)$$
$$\frac{d\Delta G(x,Q^2)}{d\ln Q^2} = \frac{\alpha_s(Q^2)}{2\pi}\int_x^1 \frac{dx'}{x'}\left(\sum_f \Delta q_f(x',Q^2)\Delta P_{gq}\left(\frac{x}{x'}\right)+\Delta G(x',Q^2)\Delta P_{gg}\left(\frac{x}{x'}\right)\right), \quad (1.9)$$

with $\Delta P_{ij} = P_{i+j+} - P_{i+j-}$. In principle a measurement of the Q^2 dependence of the polarized quark distributions can lead to a determination of ΔG by comparing the data at different Q^2 with the evolution of $g_1(Q_0^2)$ to $Q^2 > Q_0^2$. However, the parametrizations of $g_1(Q_0^2)$ are model dependent, and the data do not yet have sufficient statistical precision and are still consistent with $\Delta G = 0$ within the statistical uncertainties of the fits.[Geh96].

1.2.2 Photon-Gluon Fusion and Charm Production

Another possibility to measure the gluon polarization is to select QCD processes which depend on the helicity of the gluon involved. One of these processes is the production of charm quarks by Photon-Gluon Fusion (PGF, see figure 1.3). Because of their high mass, the content of charm

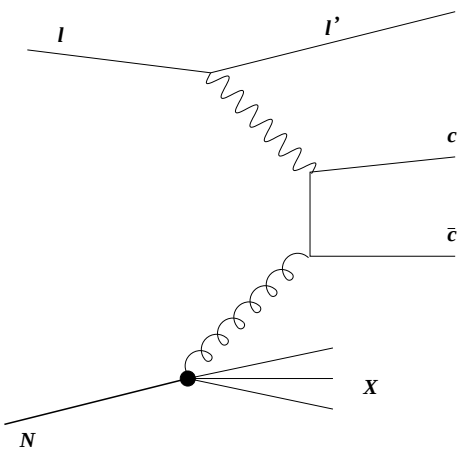

Figure 1.3: The Photon-Gluon Fusion diagram for charm leptoproduction. The virtual photon and the gluon interact through an intermediate $c\overline{c}$-pair. The scale at which the gluon structure function enters the cross section for this process is set by the charm mass, $2m_c \simeq 3.1$ GeV.

quarks in the nucleon wave function is negligible, and the contribution of the normal DIS diagram to charm production is suppressed [Ing97]. The detection of mesons containing charm quarks is a 'tag' for the PGF process. 'Hidden charm', i.e. the recombination of the $c\overline{c}$-pair leads to J/ψ-meson production, while in 'open charm' production two charmed particles (D^0, D^*, Λ_c) are produced. The asymmetry for a PGF process can be calculated as

$$A_{\parallel}(z,p_T) = \hat{a}_{\parallel}\frac{\Delta G}{G}. \quad (1.10)$$

Here, $\hat{a}_{\parallel}$ is the asymmetry of the hard scattering process and p_T is the transverse momentum of the charm meson. The value of the subprocess asymmetry depends on the production mechanism. If a J/ψ is produced in PGF, another gluon must be radiated off so that the meson is in a color singlet state. Two models exist for this mechanism, the color singlet model, which predicts $\hat{a}_{\parallel} \approx 0.5$ for HERMES kinematics, and the color octet model for which $\hat{a}_{\parallel} = 1$ [Gup97]. Since the J/ψ is a neutral vector meson, it can also be produced through diffractive processes, which is found to be the dominant production mechanism at HERMES . The HERMES c.m. energy of 7.4 GeV is just above the threshold for J/ψ production. The inclusive J/ψ asymmetry has been measured at HERMES, although with low statistical precision, and was found to be consistent with zero. Several upgrades of the experiment will help to increase the number of J/ψs detected in the years since 1998 [Ama97]. An iron wall to absorb hadrons has been set up behind the calorimeter, followed

by a scintillator hodoscope. This will improve muon identification and allow better J/ψ detection via the $J/\psi \to \mu^+\mu^-$ channel. A Forward Quadrupole Spectrometer (FQS) will be able to detect electrons scattered at very small angles which would allow the full kinematic reconstruction of events and help to separate diffractive J/ψ events from events sensitive to ΔG . These events are expected to be in the range of $0.7 < z < 0.9$ [Jap99].
The open charm production has an about ten times larger cross section than J/ψ production. It is possible to find D^0 and $\overline{D}^0$ via their decay channels into $K^+\pi^-$ and $K^-\pi^+$ respectively. The combinatorial background can be significantly reduced by separating K/π, which at HERMES can be done using the RICH (since 1998), and also by tagging D^*, where an additional soft pion from $D^* \to D\pi$ is required.

1.2.3 Photoproduction of High-p_T Hadrons

Because of the low center-of-mass energies available at most fixed target experiments, the access to PGF processes with charm production is limited by statistics. It has been suggested that the photoproduction of light $q\overline{q}$-pairs, leading to outgoing single [Afa98], or pairs of hadrons [Bra98], with high p_T can be sensitive to the PGF process as well. Here the term 'photoproduction' refers to the low Q^2 region of lepton-nucleon scattering, meaning that a quasi-real photon beam is used. There are four different ways of how hadrons can acquire transverse momentum in DIS:

1. The intrinsic k_T of the struck quark. According to the uncertainty relation quarks confined in the nucleon must have an intrinsic momentum of ≈ 0.4 GeV. In the absence of other processes generating p_T the cross section for hadrons produced in lepton-nucleon interactions would fall exponentially in p_T^2.

2. The struck quark can multiply radiate soft gluons.

3. Hard QCD subprocesses (e.g. gluon radiation) can generate large p_T.

4. p_T can be accumulated in the fragmentation process.

Only the hard QCD subprocesses can account for sufficiently large p_T. In order to suppress the usual $\gamma^* q$ scattering one can require a large p_T of the outgoing hadron. Requiring the photon to have low virtuality (Q^2) helps because photoabsorption as described in the naive parton model is kinematically impossible at $Q^2 = 0$. At low $Q^2 \to 0$ however, one has to consider the hadronic structure of the photon which will be the dominant source of strong interaction with the proton.

The Structure of the Photon

Only in a first approximation the photon is a pointlike particle. Quantum mechanically it may fluctuate into a (charged) fermion-antifermion pair. The major part of the γp cross section comes from fluctuations $\gamma \leftrightarrow q\overline{q}$. The virtuality scale of the fluctuations is given by the transverse momentum k_T of the (photonic) partons. Fluctuations with low virtualities enter a domain of non-perturbative QCD, whereas high virtuality fluctuations can be calculated perturbatively. The low virtuality part can be approximated with the Vector Meson Dominance (VMD) ansatz where one sums over the low mass vector meson states. The real photon wave function can be written as:

$$|\gamma\rangle = c_{bare}|\gamma_{bare}\rangle + \sum_{V=\rho^0,\omega,\phi,J/\psi} c_V|V\rangle + \sum_{q=u,d,s,c,b} c_q|q\overline{q}\rangle + \sum_{l=e,\mu,\tau} c_l|l^+l^-\rangle. \qquad (1.11)$$

Just like the nucleon structure functions, the coefficients $c_{q,l}$ depend on the scale μ used to probe the photon which is usually taken to be the transverse momentum of the $2 \to 2$ parton level process. A cutoff parameter k_0 is introduced to separate the low- and high virtuality parts of the $q\overline{q}$ fluctuations, such that $c_q^2 \approx (\alpha_{em}/2\pi)2e_q^2 \ln(\mu^2/m_q^2)$. The parameter k_0 has been determined

from data to be $\simeq 0.6$ GeV. The low virtuality fluctuations (VMD) are below k_0 and thus do not depend on μ. The probability for $\gamma \to V$ is proportional to c_V^2 with $c_V^2 = 4\pi\alpha_{em}/f_V^2$, where $f_V^2/4\pi$ has been determined from data. The leptonic fluctuations (the fourth term in 1.11) are negligible for γp because they only contribute to interactions in second order. Finally, c_{bare} is obtained using unitarity: $c_{bare}^2 = 1 - \sum c_V^2 - \sum c_q^2 - \sum c_l^2$. With this description of the photon structure, three event classes in γp interactions can be defined:

a) VMD processes, where the photon turns into a vector meson and therefore all processes allowed in hadronic physics may occur (elastic and diffractive scattering, low- and high p_T non-diffractive events).

b) Direct processes, where the bare photon interacts with a parton from the proton.

c) Anomalous processes, where the photon branches into a $q\overline{q}$ pair (perturbatively) and one of the quarks then interacts with a parton from the proton.

Figure 1.4 shows schematically the different event classes. The classification of these processes

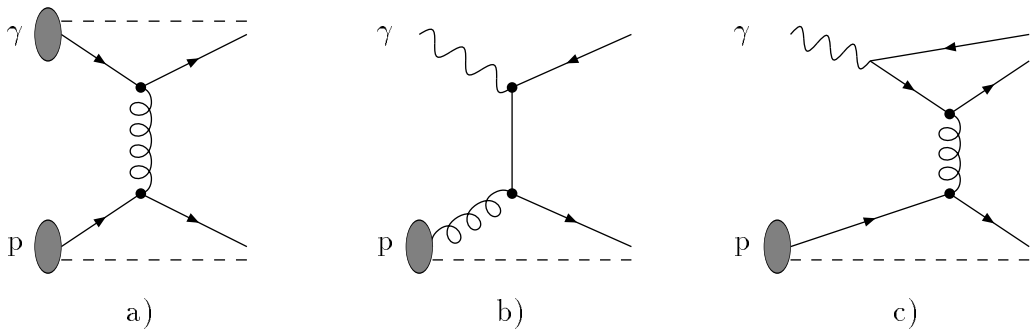

Figure 1.4: Contributions to hard γp interactions: a) VMD, b) direct, and c) anomalous. The presence of spectator jets has been indicated by dashed lines, while full lines show partons that (may) give rise to high-p_T jets.

according to the different scales involved and their contribution to the total cross section is described in detail in [Fri00]. Which of these event classes is the dominating one depends on the c.m. energy. In principle there are two different transverse momentum scales, k_T and $\hat{p}_T$, involved in these processes. k_T is related to the $\gamma \to q\overline{q}$ vertex while $\hat{p}_T$ is the scale of the hardest QCD subprocess involved. If $k_T < k_0$, i.e. small transverse momentum at the $\gamma \to q\overline{q}$ vertex, VMD is dominating. For $k_T > k_0$, the distinction between anomalous and direct processes is made at $k_T = \hat{p}_T$. If $\hat{p}_T > k_T$, the process is anomalous, if $k_T > \hat{p}_T$, it is direct.

For the low HERMES center-of-mass energy, $\sqrt{s} \simeq 7$ GeV, models involving only real photons predict VMD to contribute a very large fraction $> 90\%$ to the total cross section for *single* hadrons [Afa99]. For *pairs* of high-p_T hadrons Monte Carlo simulations using PYTHIA (version 5.7) showed that the direct photon cross section dominates if both hadrons have sufficiently large p_T [Mar00]. Anomalous processes contribute only at significantly higher energies. The total (real) photoproduction cross section can be decomposed as:

$$\sigma_{tot}^{\gamma p}(s) = \sigma_{VMD}^{\gamma p} + \sigma_{direct}^{\gamma p} + \sigma_{anomalous}^{\gamma p}. \tag{1.12}$$

A finite virtuality of the photon itself, $Q^2 > 0$ introduces another scale dependence into the cross section, because now also the 'ordinary' DIS process will contribute. The photon can still resolve into vector meson or $q\overline{q}$ states, but with a reduced probability given by dipole factors $\left(\frac{m_V^2}{m_V^2+Q^2}\right)^2$ or $\left(\frac{4k_T^2}{4k_T^2+Q^2}\right)^2$ for the vector meson and $q\overline{q}$ states respectively. The quasi-real photoproduction cross

section is then:

$$\sigma_{tot}^{\gamma^* p}(s) = \sigma_{VMD}^{\gamma^* p} + \sigma_{direct}^{\gamma^* p} + \sigma_{anomalous}^{\gamma^* p} + \sigma_{DIS}^{\gamma^* p}. \tag{1.13}$$

The DIS cross section needs to be parametrized such that it is at least finite, or even vanishing, at low $Q^2 \to 0$. At higher Q^2 the resolved photon processes are strongly suppressed, but the direct processes are no longer dominating the unresolved photon cross section. They will rather be treated as a NLO correction to DIS.

Asymmetries in High-p_T, Low Q^2 Hadron Production

In polarized quasi-real photoproduction the VMD processes are believed to be insensitive to spin, the spin asymmetry $\Delta\sigma_{VMD}/\sigma_{VMD} \approx 0$. However, if these processes contribute to the total cross section, they dilute the asymmetry $\Delta\sigma_{tot}/\sigma_{tot}$. At $Q^2 = 0$ the only direct processes possible are Photon-Gluon Fusion $\gamma g \to q\overline{q}$ and the QCD Compton (QCDC) scattering $\gamma q \to qg$, because the DIS process $\gamma q \to q$ is kinematically not allowed. The Feynman diagrams for these processes are shown in figure 1.5. At nonzero Q^2 DIS becomes possible, but may be suppressed by requiring high p_T of the outgoing hadron. The cross sections are given by:

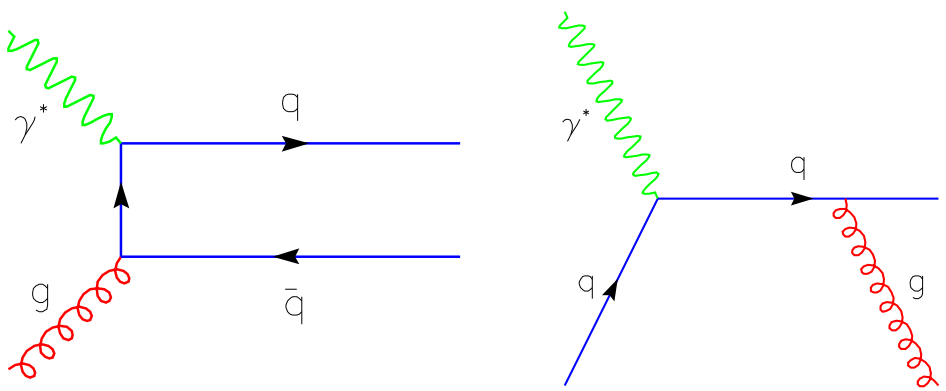

Figure 1.5: Feynman diagrams for the two LO QCD subprocesses Photon-Gluon Fusion (left) and QCD Compton scattering (right).

$$\begin{aligned}
\frac{d\sigma_{PGF}}{d\hat{t}} &= \frac{\pi e_q^2 \alpha_{em}\alpha_s}{\hat{s}^2}\left(\frac{\hat{u}}{\hat{t}} + \frac{\hat{t}}{\hat{u}} - \frac{2\hat{s}Q^2}{\hat{t}\hat{u}}\right), \\
\frac{d\sigma_{QCDC}}{d\hat{t}} &= \frac{8\pi e_q^2 \alpha_{em}\alpha_s}{3\hat{s}^2}\left(-\frac{\hat{u}}{\hat{s}} - \frac{\hat{s}}{\hat{u}} + \frac{2\hat{t}Q^2}{\hat{s}\hat{u}}\right).
\end{aligned} \tag{1.14}$$

These equations are valid for massless quarks and gluons. The Mandelstam invariants $\hat{s}$, $\hat{t}$, $\hat{u}$ are defined at the subprocess level, they are connected to the photon virtuality by $\hat{s}+\hat{t}+\hat{u} = -Q^2$. In electroproduction there is a kinematic lower limit on Q^2 for a given photon energy ν: $Q^2_{min} = \frac{m_e^2\nu^2}{E(E-\nu)}$ because of the finite electron mass. To obtain the cross section for ep one needs to multiply the $\gamma^* p$ cross section with the virtual photon flux $\Gamma(Q^2, y)$. For $Q^2 \to 0$ the scale of the hard subprocess is set to $\hat{p}_T^2 = \hat{s}\hat{t}\hat{u}/(\hat{s}+Q^2)^2$, the transverse momentum of the outgoing partons in the center-of-mass frame. For $Q^2 \to 0$ the polarized cross sections and subprocess asymmetries become:

$$\begin{aligned}
\frac{d\Delta\sigma_{PGF}}{d\hat{t}} &= -\frac{\pi e_q^2 \alpha_{em}\alpha_s}{\hat{s}^2}\left(\frac{\hat{u}}{\hat{t}} + \frac{\hat{t}}{\hat{u}}\right) \implies \hat{a}_{PGF} = \frac{d\Delta\sigma_{PGF}/d\hat{t}}{d\sigma_{PGF}/d\hat{t}} = -1 \\
\frac{d\Delta\sigma_{QCDC}}{d\hat{t}} &= \frac{8\pi e_q^2 \alpha_{em}\alpha_s}{3\hat{s}^2}\left(\frac{\hat{u}}{\hat{s}} - \frac{\hat{s}}{\hat{u}}\right) \implies \hat{a}_{QCDC} = \frac{d\Delta\sigma_{QCDC}/d\hat{t}}{d\sigma_{QCDC}/d\hat{t}} = \frac{\hat{s}^2 - \hat{u}^2}{\hat{s}^2 + \hat{u}^2}.
\end{aligned} \tag{1.15}$$

The fact that $\hat{a}_{PGF} = -1$ means that the process can only take place if the photon and gluon helicities are opposite to each other. For electroproduction the asymmetries need to be multiplied by $D(y) \simeq \frac{\Delta\Gamma(Q^2,y)}{\Gamma(Q^2,y)}$, the virtual-photon depolarization factor. The cross section for the direct processes $\gamma^* + a \to c + d$ with small Q^2 can then be written as:

$$\sigma_{dir} = \Gamma(Q^2, y) \sum_{a,c,d} \int F_{a/N}(x, \hat{p}_T^2) \frac{d\sigma}{d\hat{t}}(\gamma + a \to c + d)\, D_c^h(z) dx d\hat{t} dz, \tag{1.16}$$

where $F_{a/N}$ denotes the appropriate structure function ($q(x, \hat{p}_T^2)$ or $G(x, \hat{p}_T^2)$). Using different models for polarized quark- and gluon distributions, Afanasev et al. [Afa98, Afa99] calculated asymmetries for the inclusive, quasi-real photoproduction of pions. The results are different when different combinations of parton distributions are used. At low to moderate energies and not too low transverse momenta of the outgoing hadrons differences in the calculated asymmetries are mainly due to the differences in the input polarized gluon distributions. Especially π^- production off a proton target should show an asymmetry most sensitive to ΔG. At higher momenta, where by the kinematics of the experiment also x becomes large, the gluons in the target do not contribute to asymmetries but the data may be used instead to discriminate among various polarized quark distributions. The contribution from soft processes dilutes the asymmetries especially at low hadron momenta, which for the HERMES acceptance also correspond to lower transverse momenta.

The subject of this thesis is to measure spin asymmetries in inclusive, quasi-real photoproduction of charged single high-p_T hadrons as proposed by Afanasev et al. and to test the sensitivity of the HERMES data to the underlying parton distributions.
Based upon the above discussed appearance of subprocesses (PGF, QCDC, VMD) and assuming that DIS does not contribute in the region of phase space probed, the asymmetry for the process $eN \to hX$ can be decomposed as follows:

$$A_{\parallel}^{eN\to hX} \simeq \langle D(y) \rangle \left(\langle \hat{a}_{PGF} \rangle \left\langle \frac{\Delta G(x)}{G(x)} \right\rangle f_{PGF} + \langle \hat{a}_{QCDC} \rangle \left\langle \frac{\Delta q(x)}{q(x)} \right\rangle f_{QCDC} \right). \tag{1.17}$$

The factors f_i are fractions of unpolarized cross section for events originating from the subprocess i:

$$f_i = \frac{\int d\sigma_i^{eN\to hX}}{\int d\sigma_{tot}^{eN\to hX}}. \tag{1.18}$$

By determining the f_i and the average values of the kinematic variables per bin using Monte Carlo simulations the polarization of gluons can be extracted through:

$$\frac{\Delta G}{G}(\langle x \rangle) \simeq \left\langle \frac{\Delta G(x)}{G(x)} \right\rangle = \frac{A_{\parallel} - \langle D(y) \rangle \langle \hat{a}_{QCDC} \rangle \left\langle \frac{\Delta q(x)}{q(x)} \right\rangle f_{QCDC}}{\langle D(y) \rangle \langle \hat{a}_{PGF} \rangle f_{PGF}}. \tag{1.19}$$

Depending on the statistics available the binning in x_{gluon} will be chosen. The quark polarizations $\Delta q/q$ are known from the HERMES semi-inclusive results. They can be calculated using Monte Carlo according to the known flavor composition of the target nucleon. Note that so far it is assumed that the asymmetry for hadrons from resolved photon processes is $\simeq 0$. Measurements of double spin asymmetries in exclusive ρ meson production yielded $A_{\parallel}^{\rho} = 0.12 \pm 0.05$ at $Q^2 > 1$ GeV^2 [Mei00]. If the asymmetry for ρ production in the photoproduction regime would also turn out to be nonzero and the contribution from VMD is very large, the formula 1.19 given above has to be modified appropriately. The same is true if it turns out that the contribution from DIS is larger than expected even at high p_T.

A similar approach to the determination of $\delta G/G$ is to tag pairs of charged hadrons h^+h^-, where both hadrons have high p_T. By this requirement background from VMD and quark scattering

is strongly suppressed. This analysis was done at HERMES using the 1997 data and yielded the result $\Delta G/G = 0.41 \pm 0.18(\text{stat}) \pm 0.03(\text{exp. syst.})^{+0.42}_{-0.06}(\text{model})$ at $\langle x_G \rangle = 0.17$ at the hard scale $\langle \hat{p}_T^2 \rangle = 2.1$ GeV^2 [Mar00].

Chapter 2

The HERMES Experiment

HERMES is one of the four experiments using the HERA storage ring at DESY in Hamburg. HERA consists of two rings, one of which contains 27.5 GeV positrons or electrons and the other one stores counter rotating protons at 900 GeV. Only the positrons (electrons) are used by HERMES. The experiment has been designed for precision measurements of polarized DIS asymmetries. Therefore high beam and target polarizations are required.

2.1 The Positron Beam

The positron beam is self-polarizing through the Sokolov-Ternov effect. The polarization is induced by a small asymmetry in the emission of synchrotron radiation by positrons moving in a plane perpendicular to a uniform magnetic field. Over time positron states with spin orientation parallel to the magnetic field direction become more populated than those with antiparallel spin orientation. The resulting *transverse* polarization develops in time as an exponential:

$$P_B(t) = P_{max}\left(1 - e^{-\frac{t}{\tau}}\right). \tag{2.1}$$

Here P_{max} is the asymptotic polarization and τ is the rise-time constant. Both quantities are effective values for a real machine, where depolarizing effects reduce the theoretically achievable maximum polarization P_{ST} and rise time τ_{ST}:

$$P_{ST} = \frac{8}{5\sqrt{3}} = 92.38\%, \qquad \tau_{ST} = \frac{8}{5\sqrt{3}}\frac{m_e^2 c^2 \rho^3}{e^2 \hbar \gamma^5} = 37 \text{ min}. \tag{2.2}$$

These values are calculated for an average HERA bending radius ρ =707 m and for 27.5 GeV positrons [Bar94]. Empirical optimization of the positron orbit is employed to reduce depolarizing effects such as magnetic field imperfections and kinks in the positron orbit induced by synchrotron emission. Up to 70% polarization with a rise time of about 20 minutes can be achieved. A transverse (TPOL) and a longitudinal (LPOL) polarimeter provide precise polarization measurements using Compton backscattering of circularly polarized photons off the positrons. To provide *longitudinal* polarization for HERMES two spin rotators are placed in the arcs close to the experiment. The rotator before HERMES turns the spin into the axis of the beam momentum whereas the one behind the experiment turns it back to the transverse direction. A schematic picture of the storage ring is shown in figure 2.1.

2.2 The Internal Gas Target

HERMES uses a gas target internal to the positron beam. In order to increase its areal density the gas is fed into a storage cell. The storage cell is an open ended elliptical tube (40 cm long, 29

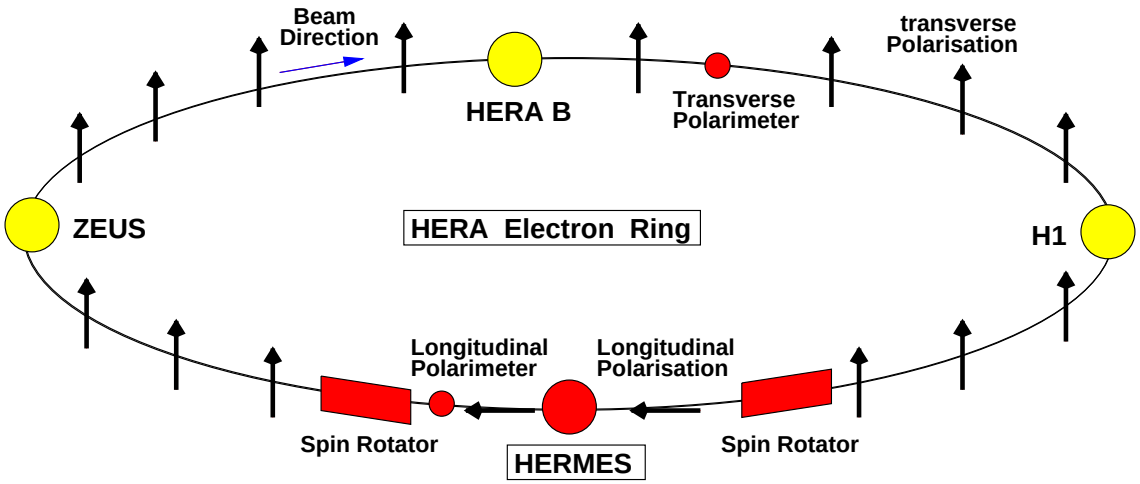

Figure 2.1: Sketch of the HERA positron storage ring with the four experiments. The spin rotators around HERMES turn the positron spin from transverse to longitudinal and back. Also shown are the polarimeters where the transverse and longitudinal polarization is measured in the ring.

mm wide and 9.8 mm high) made of thin (75 μm) ultra pure aluminium. It is being cryogenically cooled in order to reduce the thermal velocities of the gas atoms inside. A feed tube through which the polarized gas atoms are injected into the cell is installed perpendicular to the beam axis in the center of the cell. The atoms perform wall collisions and diffuse into the ultra high vacuum of the positron beam line, where they are being pumped away by a high speed differential pumping system. During the diffusion process the atoms cross the positron beam many times and thus increase the areal target density by two orders of magnitude compared to an atomic beam. Polarized hydrogen is provided by an Atomic Beam Source (ABS). A 13.56 MHz radio frequency field dissociates molecular hydrogen into atoms. A beam is being formed which passes through a collimator into a vacuum chamber where five sextupole magnets polarize the electron spins with respect to the beam axis by Stern-Gerlach separation. The electron spin polarization is then being transfered to nuclear polarization by a radio frequency field inducing hyperfine transitions. A magnetic holding field of 335 mT along the beam axis is generated by a superconducting magnet. By changing the frequency of the RF transition it is possible to select states in either proton spin direction within seconds. At HERMES the proton spin is being flipped randomly on the time scale of a minute, fast enough to reduce systematic influences on asymmetry measurements to a minimum and slow enough to avoid synchronization problems in the data acquisition. In 1998 the ABS was modified as a polarized deuteron source.
To measure the atomic polarization a small fraction of the target gas is extracted through a sampling tube and analyzed in a Breit-Rabi-Polarimeter (BRP). A system of sextupole magnets and RF transitions allows to separate the different hyperfine states which then enter a quadrupole mass spectrometer. The polarization can be calculated by measuring the relative occupation numbers of the hyperfine states. The Target Gas Analyzer (TGA) is being used to measure the degree of recombination of the hydrogen atoms to molecules. It is mounted in front of the entrance to the BRP at an angle of 7° to the sampling tube. Figure 2.2 shows a schematic view of the target region with the ABS and BRP.

2.3 The Spectrometer

The HERMES detector is an open forward magnetic spectrometer consisting of two identical halves above and beneath the HERA beam pipes. The location of the various detectors is shown in figure

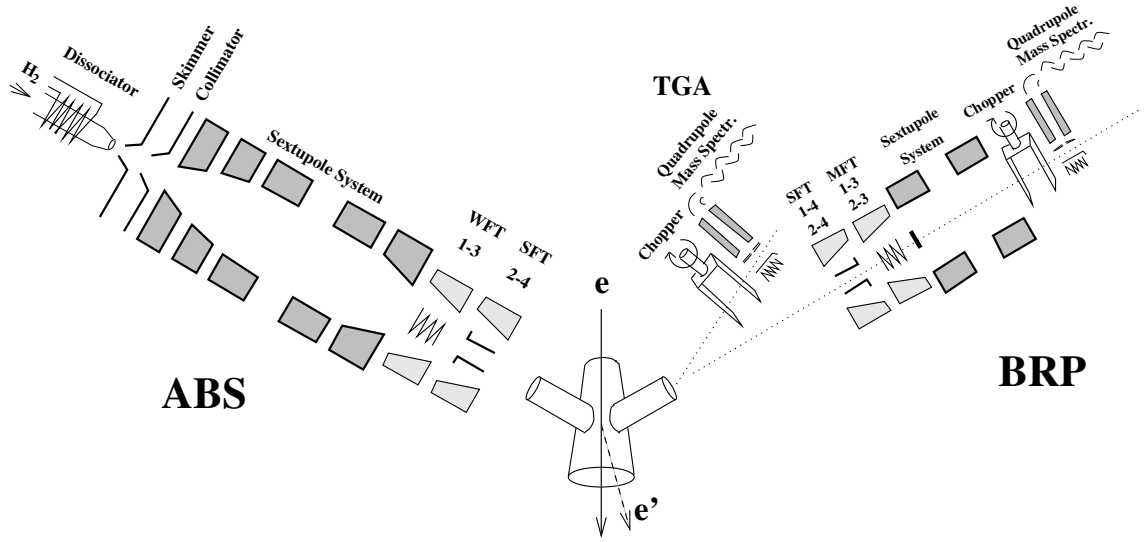

Figure 2.2: Representation of the Atomic Beam Source (ABS), Breit-Rabi-Polarimeter (BRP) and Target Gas Analyzer (TGA) with the storage cell in the center.

2.3. The z-axis of the HERMES coordinate system is defined by the beam momentum, the y-direction goes vertically upward, whereas the x-axis lies in the ring plane such that the positive x-direction points away from the center of the ring.

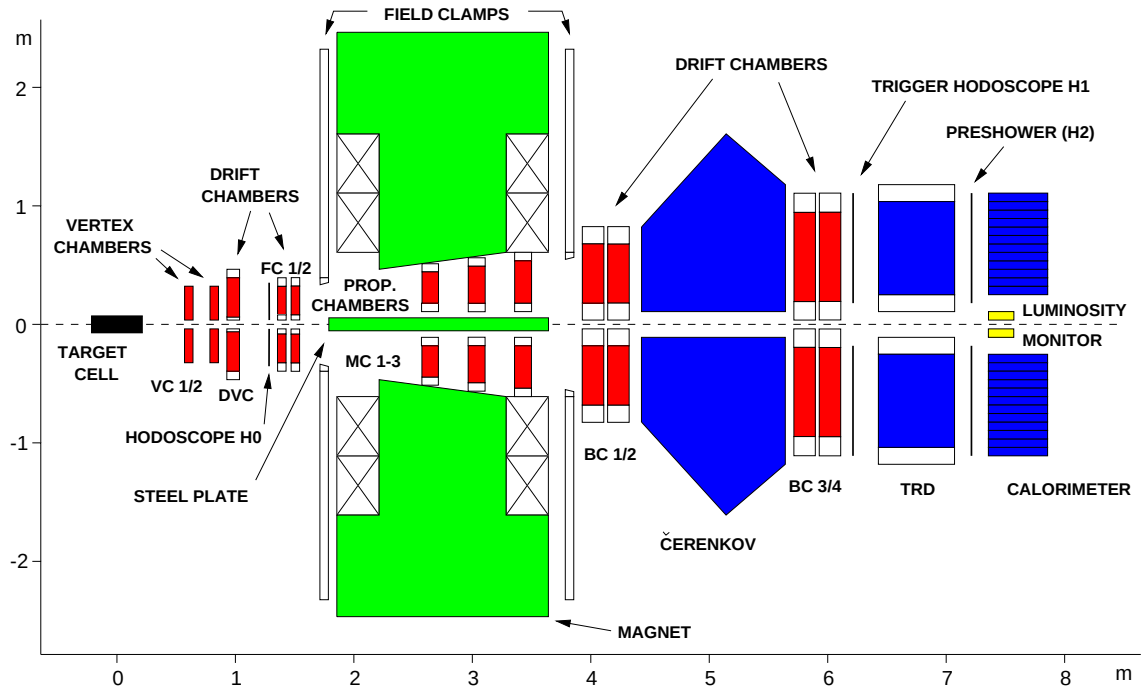

Figure 2.3: A two dimensional cut of the HERMES spectrometer in the 1996/97 configuration. In 1998 the Cherenkov detector was replaced by a dual radiator Ring Imaging Cherenkov (RICH), and an iron wall with tracking hodoscopes was installed behind the calorimeter for muon identification.

2.3.1 The Spectrometer Magnet

During data taking the spectrometer magnet is operated at a deflecting power of $\int B\,dl = 1.3$ Tm. The magnetic dipole field is oriented in the vertical direction, deflecting charged particles horizontally. The magnet encloses the geometrical acceptance of the spectrometer to ± 140 mrad in the vertical and ± 170 mrad in the horizontal direction. To maintain good acceptance for low momentum particles the acceptance of the detector in the horizontal plane is increased by ± 100 mrad starting from the center of the magnet. The lower limit on the vertical acceptance of ± 40 mrad is given by the massive shielding plate in the horizontal plane.

2.3.2 The Tracking Devices

The first set of tracking chambers next to the target are the Vertex Chambers (VC), two modules of microstrip gas chambers (MSGC) with three planes each. The strip pitch is very small compared to conventional wire chambers resulting in higher resolution, but also in a large number of channels to be read out. Special readout electronics for this task are implemented in so-called Analog Pipeline Chips (APCs). In 1995 these chips did not work stably enough. Only after replacing these chips with a newer version the VCs could be used for event reconstruction in 1997. Because of the initial problems of the VCs a set of drift vertex chambers (DVC) were installed 1.1 m downstream of the target between the 1996 and 1997 data taking periods. They consist of six planes of conventional drift chambers with a wire spacing of 6 mm. Next to them, at about 1.6 m from the target center, just in front of the magnet, are the Front Chambers (FC). They are drift chambers like the DVCs, arranged in two modules of six planes each. Behind the magnet there is a set of four drift chambers, the so-called Back Chambers (BC), combined into two groups in front of and behind the Cherenkov detector. The front and back partial tracks are reconstructed independently and then matched together in the center of the magnet using a fitting procedure. To resolve ambiguities in the track matching three modules of multi-wire proportional chambers are installed inside the magnet (MC). They are particularly useful to track low energy particles which leave the acceptance of the backward part of the detector or hit the magnet side walls. Overall tracking efficiencies larger than 95 % are achieved with a momentum resolution of 0.7 to 1.25% over the kinematic range of the experiment and an uncertainty in the scattering angle θ lower than 0.6 mrad.

2.3.3 The Particle Identification Devices

Four different particle identification (PID) detectors provide a very clean separation of the scattered positron from hadrons. The electromagnetic calorimeter consisting of 420 lead glass blocks in each half is located at the downstream end of the spectrometer. It is used to measure the total energy of positrons and photons. The length of the lead glass blocks of 50 cm corresponds to 18 radiation lengths. A positron passing through the calorimeter deposits nearly all its energy there. The energy loss of hadrons is dominated by nuclear interaction and ionization losses $\frac{dE}{dx}$. Since the nuclear interaction length is significantly longer than the radiation length, a hadron deposits only a fraction of its energy in the calorimeter. The ratio of deposited energy and momentum $\frac{E_{calo}}{p}$ of a particle can be used to separate hadrons from positrons.
Two hodoscopes (H1 and H2) are installed in the HERMES back region. They form an essential part of the HERMES trigger, together with the front hodoscope H0 which is installed in front of the FCs. H2, right in front of the calorimeter, is also used as a preshower detector for particle identification by a plate of 11 mm thick lead surrounded by 1.3 mm steel sheets that is placed in front of the scintillator paddles. Positrons may initiate electromagnetic showers that deposit energy in the scintillators whereas hadrons only produce a minimum ionizing signal.
The third PID detector in front of H2 is a transition radiation detector (TRD). Transition radiation (TR) is created when a charged particle crosses the boundary between two media with different dielectric constants ϵ. The threshold for the HERMES TRD to generate a significant amount of TR is set by a Lorentz factor of $\gamma \simeq 500$. At HERMES energies only positrons are above this

threshold. Other particles can only deposit energy due to ionization losses. The TRD consists of six modules in each detector half. The modules themselves are MWPCs with a 6.35 mm radiator in front. The radiators are formed from layers of loosely packed polyethylene/polypropylene fibres, providing many boundaries for the positron to traverse. The combination of the six modules allows to identify positrons with a pion rejection factor (PRF = the number of pions divided by the number of pions misidentified as positrons) of ≈ 300 at a positron identification efficiency of 90%. The HERMES threshold Cherenkov counter is used to provide positron identification below the threshold momentum for pions. The two modules consist of a gas radiator and a system of 20 spherical mirrors and 20 matching photomultiplier tubes mounted on the outside of the aluminium enclosure that contains the mirrors and the gas. The threshold velocity of a charged particle to radiate Cherenkov light in a medium with refractive index n is given by:

$$v \geq \frac{c}{n} \quad \text{corresponding to} \quad p_{th} = \beta_{th}\gamma_{th}m_0 = m_0\sqrt{\frac{1}{n^2-1}}. \tag{2.3}$$

Here p_{th} is the threshold momentum for a particle with mass m_0. The radiator gas is a mixture of 70% N_2 and 30% C_4F_{10}, resulting in a p_{th} of 20.9 MeV for $e^{\pm}$, 3.8 GeV for pions and 13.9 GeV for kaons. If the other PID detectors identify a track as a hadron, Cherenkov radiation can be used to identify pions in a momentum range from 3.9 to 13.9 GeV.

2.3.4 The Luminosity Monitor

To measure the luminosity, HERMES uses two small calorimeters on both sides of the beam pipe in the horizontal plane, about 7.2 m downstream of the target. They are particularly sensitive to Bhabha scattering ($e^+e^- \rightarrow e^+e^-$) and annihilation processes ($e^+e^- \rightarrow \gamma\gamma$) between beam positrons and target electrons. These events may be separated from background by requiring coincident high energy clusters in each calorimeter. The calorimeters consist of 3×4-arrays of $NaBi(WO_4)_2$ crystals, each of which is read out by an individual photomultiplier. From the known cross section for e^+e^- scattering and the coincidence rate the luminosity can be determined.

2.4 Data Acquisition System (DAQ) and Software

The HERMES trigger system efficiently selects events which are interesting for physics analysis. Several triggers are used for different analyses. The main DIS trigger ('trigger 21') selects DIS candidates by requiring coincident signals in the three hodoscopes in one detector half and a minimum energy deposited in the calorimeter. For running with a polarized target the energy threshold was 3.5 GeV until this requirement was changed to 1.4 GeV in the middle of the 1996 running period. Other triggers select e.g. quasi-real photoproduction events with at least one full track in each half of the detector, or are used for more technical purposes such as calibrations etc. Not all of the generated triggers can be accepted by the DAQ. During the time needed for readout, newly generated triggers cannot be accepted, leading to a deadtime of the trigger system. The deadtime is defined as the ratio of rejected trigger requests to the total number of generated triggers. The data acquisition digitizes the analog and timing information for a generated trigger in the ADC and TDC modules located in Fastbus crates. The information from the Fastbus modules is then sent to a cluster of DEC Alpha workstations and stored on hard disks. During the breaks in between HERA fills the data on these disks are copied to tapes for permanent storage. The HERMES DAQ is capable of reading out the detector information at rates up to 500 Hz with deadtimes below 10%.

Several steps are needed to convert the raw detector data into information about track parameters etc. First the data are translated from the EPIO (Experimental Physics Input Output) format to an ADAMO data base format using the HERMES decoder program HDC. The decoded detector information is then passed to the track reconstruction code HRC, and the reconstructed

track data are again stored in ADAMO. For physics analysis so-called μDSTs are produced, where the track information is synchronized with slow control data (information like supply voltages, temperatures etc. which is read out on a time scale of seconds). The μDSTs contain only a reduced data set where loose cuts on events were applied already. The data are grouped in three different levels. The lowest level, an event, contains all the reconstructed tracks in the spectrometer for a generated trigger. On the next level the events are grouped in bursts, corresponding to ten seconds of data taking. These bursts are then grouped into runs. The length of a run (about ten minutes of data taking) correspond to about 450 MB of raw EPIO data volume.

Chapter 3

Analysis on Double Spin Asymmetries

This analysis concentrates on the measurement of double spin asymmetries in inclusive quasi-real photoproduction of single high-p_T hadrons. Afanasev et al. suggested that the polarization asymmetries of positive and negative hadrons may be sensitive to the gluon polarization at low x and to the quark polarization at high x [Afa98]. It is being investigated if with the HERMES data it is possible to distinguish between the different parametrizations for the polarized gluon and quark distributions, respectively.

3.1 Data Quality

For the analysis the 1996 c1 and the 1997 c1 μDST productions were used, the two most up-to-date datasets on polarized hydrogen available. Still, there exist large differences between both years. The target calibration scheme is completely different in 1996 and several of the informations available for 1997 are not yet there for 1996. The experimental conditions varied in time, in general the experiment was much more stable in 1997. The 'good' data in 1996 only amount to about 30 % of those in 1997. In order to ensure their compatibility a number of additional checks were done that are beyond the standard data quality procedure commonly in use at HERMES.

3.1.1 Data Quality Cuts

The usual time scale to read out slow control data at HERMES is about ten seconds, the length of a 'burst'. For 1996 c1 the bursts were marked with a flag in an ADAMO table named g1Quality. A cut on this flag selected bursts with a fully operating detector (top and bottom) and reasonable beam polarization and luminosity conditions. For 1997 the data quality selection goes via a list of bits which are questioned each time a new burst is being processed by the analysis code. In general one asks for a good performance of the top and bottom detector, the target, good external conditions and a stable data acquisition (DAQ). Below the data quality cuts for 1997 are included:

1. **beam polarization**: $0.3 \leq P_B \leq 0.8$;
2. **beam current**: $5\text{mA} \leq I \leq 50\text{mA}$, corresponding to
3. **fitted luminosity rate**: $5\text{Hz} \leq L \leq 60\text{Hz}$, with no dead blocks in the luminosity monitor;
4. **target polarization**: $0.6 \leq P_T \leq 1.5$ (due to statistical fluctuations in the BRP the raw polarization can be higher than 1);
5. **fraction of H-*atoms* in the target**: $\alpha_R \geq 0.7$ (if there was a beam dump in the target cell or the cell temperature is too high, α_R usually drops below that value).
6. **target state**: The target should be in the '2-state flipping' mode; the time when the target is just flipping between spin states is cut out, the target magnet should be working;

7. **averaged DAQ-lifetime**: $0.5 \leq t^D \leq 1$. Under normal conditions during polarized running the lifetime is well above 0.9.

8. **tracking detectors**: no high voltage trips in the front and back chambers (top and bottom);

9. **PID detectors**: fully operating TRD, Cherenkov and preshower, calorimeter (top and bottom), with no dead blocks in the calorimeter and preshower;

10. **synchronization and DAQ**: the first burst of a run is being cut out, the burst number should not jump.

As already stated, the data quality selection was partially different in 1996:

1. **detector, target, DAQ and beam**: usually all the data quality bits are combined as a flag into one variable. By ensuring that the value of this variable is zero for the top and bottom detector basically the same cuts on bursts as in 1997 are imposed. Only two additional cuts are needed:

2. **the target state**: Bursts where the target is just flipping are cut out.

3. **DAQ lifetime**: The cut on the average DAQ-lifetime is the same as in 1997, but also the lifetime for trigger 21 should be in the range from 0.5 to 1.

3.1.2 Experimental Conditions

The measured spin asymmetry is the ratio of the difference to the sum of luminosity weighted and polarization averaged hadron rates in either spin state (see eq.3.10). Although the data quality cuts make sure that the data were produced under well controlled circumstances, and care was taken that those circumstances would not change on a time scale of a spin flip, experimental conditions might still have an effect on the asymmetries. Because of $A_{\parallel} \propto \frac{1}{\langle P_B P_T \rangle}$, the polarizations of beam and target certainly do influence the measurement, but also the performance of PID detectors (contamination of hadrons with leptons) or background (mainly from the proton beam) and, correlated to that, the DAQ lifetime. Tracking efficiencies may have an indirect effect. The calibration of the luminosity should not effect the asymmetry though, since an asymmetry is a ratio of cross sections measured in the same experimental environment at nearly the same time.

Beam Polarization

The main difference between the years is that the bulk part of the data in 1997 was taken with the beam helicity *opposite* to that of 1996. The average beam polarization is 0.53 ± 0.06 in both years with a total relative systematic error of 3.38%. This uncertainty is the squared sum of two contributions:

$$\left(\frac{\Delta P_B}{P_B}\right)_{rise} = 3.26\% \qquad \text{and} \qquad \left(\frac{\Delta P_B}{P_B}\right)_{point} = 0.9\%.$$

The uncertainty in the absolute calibration of the polarimeters is $\Delta P_{B\,rise}$, whereas $\Delta P_{B\,point}$ arises in both years due to uncertainties in the corrections applied to the raw polarization data.

Target Polarization

The Breit-Rabi spectrometer measures the polarization of hydrogen *atoms*. The target gas coming from the Atomic Beam Source is diluted with *molecules* (the atomic fraction is $\alpha_0 \simeq 0.97$ in 1997).

The atoms may partially recombine while they are in the target cell (the fraction of 'surviving' atoms is $\alpha_R \simeq 0.94$). The measured polarization value has to be corrected for the molecular fraction in the BRP. The polarization of the hydrogen molecules is very poorly known. In 1997 this was done using the very precise measurements of α_0 and α_R [Bau98]:

$$P_T{}^{97} = P_{BRP} \cdot \alpha_0 (\alpha_R + (1 - \alpha_R)\beta) \tag{3.1}$$

where

$$\alpha_R = C_\alpha \cdot \alpha_{TGA}. \tag{3.2}$$

The polarization measured by the BRP is P_{BRP}, whereas α_{TGA} is the atomic fraction measured by the target gas analyzing system (TGA). This value is measured from only a small sample of the target gas, which is why it needs to be corrected by the factor C_α [Hen00]. The residual molecule polarization β is not accessible via a direct measurement. An indirect measurement yielded the result $\beta = 0.6 \pm 0.4$ with a large uncertainty [Kol98]. As long as the fraction of molecules $1 - \alpha_R$ is small, this uncertainty does not have a significant effect on the target polarization. This scheme cannot be applied for the 1996 data, since a different target operation at that time led to $1 - \alpha_R = 12\%$, which would result in an unacceptable large systematic error on P_T. Instead the value of the inclusive positron DIS asymmetry $A_\parallel \simeq \frac{g_1}{F_1}$ from the 1996 data was matched to that of 1997 by a scale factor. This scaling led to a recalibration of the target polarization for 1996 [Bec00]

$$P_T^{96} = P_{BRP} \cdot \alpha_0 \cdot \eta_{norm} \tag{3.3}$$

with $\eta_{norm} = 0.929 \pm 0.042$. The uncertainty arises from the statistical errors of both asymmetries. The overall systematic error on the target polarization is thus 4.4% in 1997 and 6.3% in 1996, taking into account the relative uncertainty of η_{norm}.

Luminosity

The luminosity at HERMES is determined using Bhabha scattering of beam positrons on electrons of the target atoms. The luminosity monitor detects coincident e^+e^- pairs. Within 100 seconds a statistical precision of 1% is achieved. The measured rate is then normalized with the known cross section of Bhabha scattering at HERMES, with a systematic uncertainty of 6.5% [Ben98]. Any systematic uncertainty in the luminosity cancels in the determination of $A_\parallel$. Using the raw luminosity rate for the normalization of the hadron yields can lead to a false asymmetry due to large statistical fluctuations on a burst-by-burst level (within 10 seconds), the time scale of the target spin flips. There is also a residual electron polarization of $\approx 3\%$ leading to a Bhabha asymmetry, which can in principle be corrected for. To avoid such difficulties, fitted luminosity values are available for both years. The rate determination may be affected by the beam position and beam slope, because the acceptance of the luminosity monitor changes with the beam slope. The fill-averaged position of the beam on the x-axis is shown in figure 3.1(a,b). The variation of normalized hadron yields per run is a 'measure' of the stability of the experiment, since for high statistics the quantity

$$Y_h = \frac{N^h}{\sum\limits_{bursts} L_i \cdot t_i \cdot {t_i}^D} = \frac{N^h}{L_{run}} \tag{3.4}$$

should be constant. Figures 3.1(c,d) show the normalized hadron yields per fill in both years. The low yields in the beginning of the 1996 running period are due to the higher trigger threshold of 3.5 GeV for the energy deposited in the calorimeter, as opposed to 1.4 GeV for the rest of 1996 and the whole year 1997. It can be seen that the yields are slightly rising with time in 1996, and that in 1997 there are several shifts of about 10%. In figure 3.2 the raw luminosity rate corrected for accidental coincidences L_{acc} is compared to the fitted luminosity L_{fit}. Shown in figure 3.2(a) is the ratio $\frac{L_{fit}}{L_{acc}}$, and in figure 3.2(b) the hadron yield Y_{acc} normalized to L_{acc}. From figure 3.2(b) it

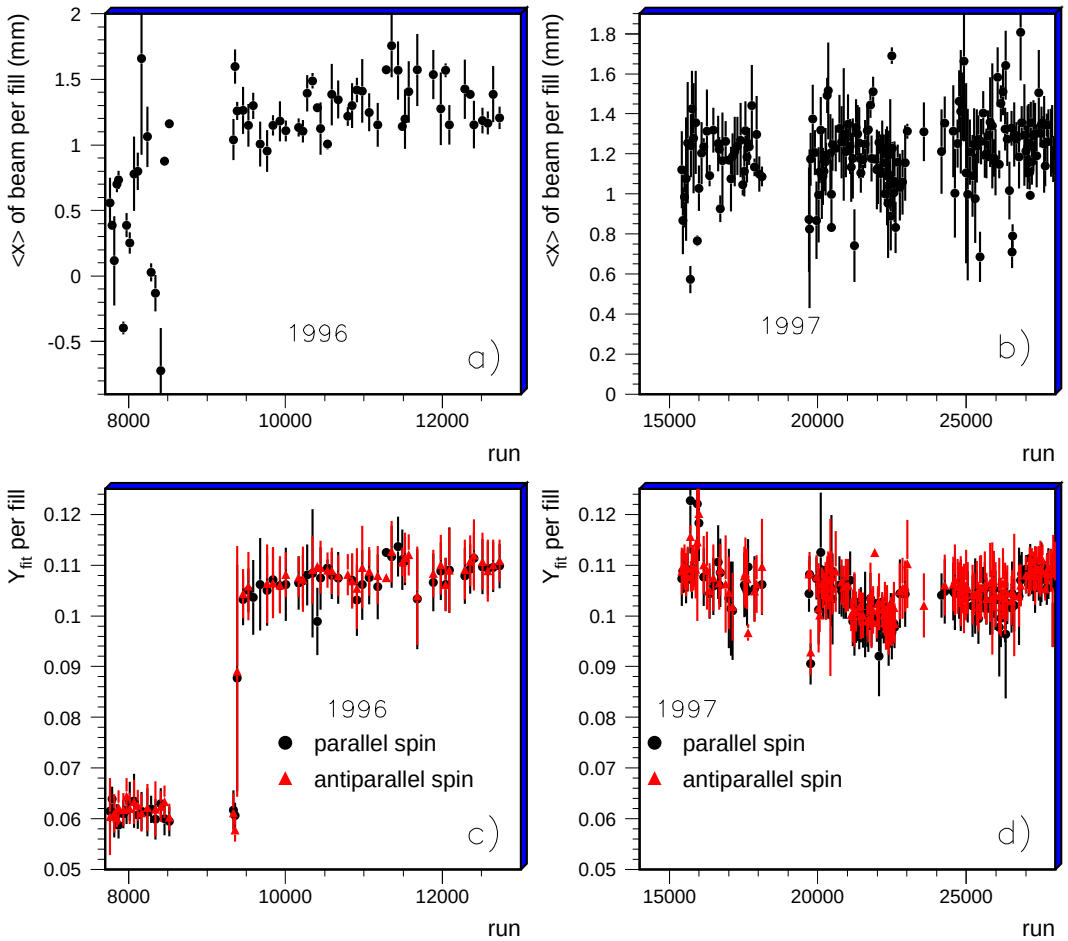

Figure 3.1: Beam position at the luminosity monitor (a and b) and normalized hadron yields (c and d) for 96 and 97, averaged over a fill. The normalization is done using the fitted luminosity rate.

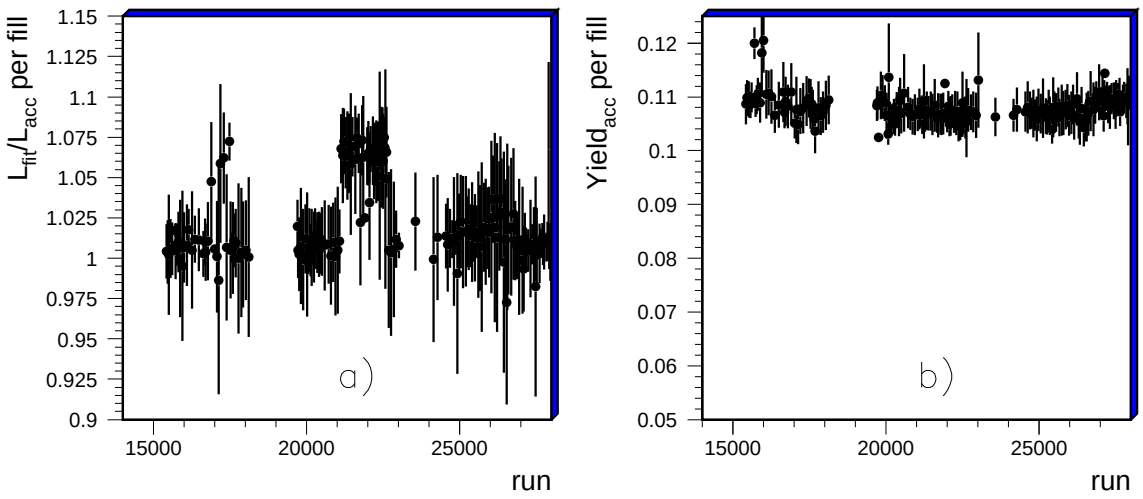

Figure 3.2: Comparison of raw luminosity rate with correction for accidentals L_{acc} and the fitted luminosity L_{fit} for 1997. The correction averaged over a fill is 0.994 ± 0.004. Shown on the left (a) is the ratio L_{fit}/L_{acc}, on the right (b) the yield normalized to L_{acc} can be seen.

is clearly to be seen that the normalization to L_{acc} does not show the large shifts in yields as the normalization to L_{fit} shown in figure 3.1(d). Especially during the 1997 period around run 20000 to 23000 one can suspect a correlation between those shifts and the deviation of the beam from the z-axis as shown in 3.1(b). The raw coincidence rate should in principle be corrected for accidental coincidences and for acceptance effects due to the beam slope and then be fitted according to a function that essentially follows the decrease of the beam current. The information needed to correct for the accidental coincidences is available only for the 1997 data, averaged over a fill it is usually not more than 1%. The decrease of the current during a fill in HERA goes exponentially with a pressure dependent time constant. Since the pressure itself is varying in time, the 'constant' does so, too. Neither this nor the two other effects have been taken into account properly for the fitting of the luminosity rate. That makes it hard to disentangle the reason for the rather large deviation of the fitted luminosity to the acceptance corrected raw luminosity that can be seen in figure 3.2(a). All these normalization uncertainties are not spin dependent, as can be seen in figure 3.1(c,d), and so have no effect on the asymmetries.

Trigger Lifetime

The trigger lifetime is limited by the readout time of the DAQ. If triggers cannot be accepted by the readout system, events are lost. The time integrated luminosity per burst needs to be corrected with the ratio

$$t^D = \frac{T_{accepted}}{T_{generated}} \quad \Longrightarrow \quad \int L\,dt = \sum_{Bursts} L_i t_i t_i^D. \tag{3.5}$$

Usually the lifetime varies over a fill. It is effected by the beam current and proton background. In 1996 the trigger lifetime variation during a fill was much larger than in 1997, also spikes in the deadtime occurred more often.

Proton Background

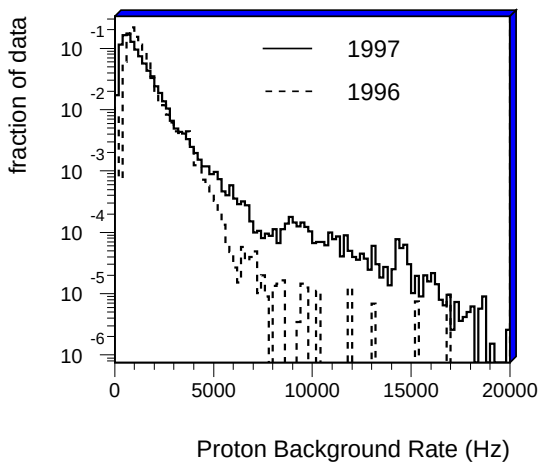

Figure 3.3: The proton background in 1996 and 1997.

The term 'proton background' refers to two different types of background coming from the proton beam in HERA. One type of background are protons which have just slightly less energy than the beam, thus they travel along with the proton beam for a long time. They only get kicked out of the beam at the last dipole before HERMES, and may strike the detector parts at very low angles. The other type of background are actually not protons from the beam but hadronic showers induced by highly energetic protons that hit the beam pipe or other material somewhere along the tunnel. Both types usually only leave tracks in the back part of the detector. The proton veto rate is a measure of the proton background. Under normal conditions this rate is lower than 2000 Hz, but

some (about 10%) of the data were taken under circumstances much worse than this, (see figure 3.3). A possible spin dependence of these data needs to be studied.

3.2 Track Selection and Tracking Method

3.2.1 Kinematic Cuts

To select a clean data sample, exclude background and wrongly reconstructed tracks, and separate hadrons (pions) from positrons a number of kinematic constraints on the tracks found in HERMES is required. The cuts used are:

Track Reconstruction

1. **Vertex**
   Any track seen should come from inside the target cell. In the HERMES coordinate system, the target cell is located at 0, and its extension in the z-direction is ± 20 cm. To ensure that the track originates from there it should have a transverse vertex (distance from the beam axis) of $d_v \leq 0.75$ cm, and a longitudinal vertex (point of intersection with the beam axis) of $|z_v| \leq 18$ cm. This rather stringent cut is due to a significant background coming from hadrons produced in events where a positron scattered on the material of the collimators in front of the target.

2. **Box Acceptance**
   The track position can be everywhere within the geometrical acceptance of the detector. This means that the projection of the scattering angle θ_x onto the x-axis (horizontal) needs to be within ± 170 mrad, and the maximum scattering angle θ_y on the y-axis (vertical) should be not more than ± 140 mrad. The minimum of θ_y is ± 40 mrad because of the shielding plate around the beam pipe being located there. This restricts the (polar) scattering angle θ to $0.04 \text{ rad} \leq \theta \leq 0.22$ rad.

3. **Full Tracks**
   Short tracks in HERMES are tracks with a momentum below 0.5 GeV which therefore do not reach the back region of the detector. For this analysis a full track throughout the detector is required.

4. **Wrongly Reconstructed Tracks**
   The magnetic field of the spectrometer magnet deflects charged particles in the x-z-plane according to [Ack98]

$$\Delta\theta_x = \pm \frac{0.2998}{p_{xz}} \int Bdl \text{ with } \int Bdl \simeq 1.3 \text{ Tm}. \tag{3.6}$$

   The plus sign is for negative, the minus sign for positive particles. In figure 3.4 the deflection angle versus the total momentum is shown for 1997, it looks similar for 1996. Approximately 0.1 % of the data are reconstructed with the wrong momentum or wrong deflection angle. In figure 3.5 the number of wrong tracks is reduced by imposing a cut:

$$\left(\frac{0.2998}{p_{xz}} \cdot 1.3 \text{ Tm} - 0.031\right) \leq \Delta\theta_x \leq \left(\frac{0.2998}{p_{xz}} \cdot 1.3 \text{ Tm} + 0.036\right) \tag{3.7}$$

   for negative particles and a symmetric cut for positive particles.

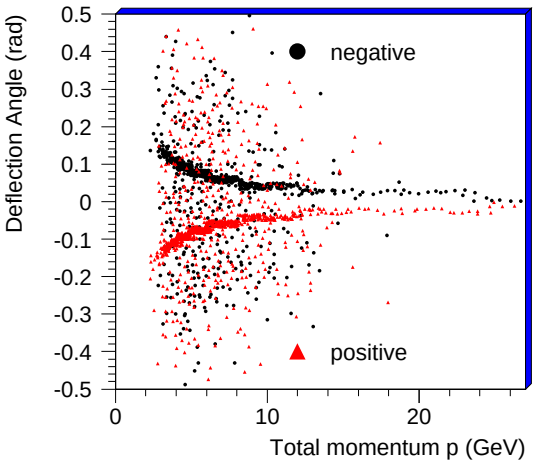

Figure 3.4: The dark bands follow the expected function $\Delta\theta_x(p)$, the flat background comes from wrongly reconstructed tracks.

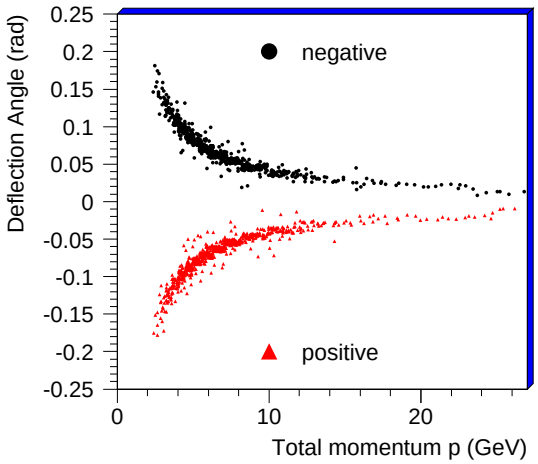

Figure 3.5: After imposing the cuts the background is nearly gone, although it cannot be completely cut out.

Particle Identification

Particle identification is essential for this analysis because of two aspects: the safe separation of hadrons from leptons and the rejection of events with a positron in the detector (see below). To separate hadrons the quantity PID $= \lg \frac{P^e}{P^h} \leq -1$ is used, where $\frac{P^e}{P^h}$ is the ratio of the probabilities that a track is a positron (electron) or a hadron. PID<-1 then means that it is ten times more probable that the track is a hadron than an $e^{\pm}$. To identify $e^{\pm}$, a cut of PID$\geq$0 is applied. The likelihoods are determined from the PID detector responses. If the track hits the edges of the calorimeter, energy gets lost. In order to ensure that the full energy deposition of the particle is being measured, a fiducial volume cut is imposed on the position of the track.

Kinematic Constraints

The hadron sample is dominated by particles with low momentum p and low transverse momentum p_T. In order to reduce this dominance and to enhance the sensitivity to physics other than virtual photon-quark scattering (on average quarks inside the nucleon have a $p_T \simeq 0.4$ GeV, cf. sect. 1.2.3), a cut of $p_T > 0.5$ GeV is imposed on all tracks. Because of the maximum possible θ of 0.22 rad this leads to an implicit momentum cut of $p \geq 2.13$ GeV. The total energy of an event (essentially the sum of the momenta of all tracks) should not be more than 28 GeV. Unfortunately the μDSTs have an intrinsic y-cut on events with track multiplicity one. In 1996 it is $y \leq 0.85$ and in 1997 it is $y \leq 0.93$. This corresponds to $p \geq 4.13$ GeV and $p \geq 1.9$ GeV for single hadron tracks in 1996 and 1997, respectively.
Pions can only be separated from other hadrons by Cherenkov radiation. The Cherenkov threshold for pions is $p^{\pi}_{th} = 3.8$ GeV, the upper limit of pion identification is set by the Kaon Cherenkov threshold $p^{K}_{th} = 13$ GeV [Ack98].
To keep the Q^2 of the event as low as possible, all events with positrons in the detector are rejected. This corresponds to a maximum Q^2 of 1.1 GeV^2 for the case that a hadron with minimum momentum of 2.13 GeV is the only particle in the event, while the average Q^2 is expected to be much lower because of the $1/Q^4$ behavior of the DIS cross section. The upper Q^2-cut is needed to suppress DIS events which are dominating at higher Q^2, and to keep the results comparable to theory. The calculations of [Afa98, Afa99] have only been carried out for low Q^2. However,

loosening the Q^2-cut increases the statistics only by 5%, so there should be hardly any effect on the asymmetries.

3.2.2 Comparison of Different Tracking Methods

The 1997 data have been reconstructed using two different methods for the front partial tracks. The first method is called 'Standard Tracking' and uses the Vertex Chambers (VC), Drift Vertex Chambers (DVC) and Front Chambers (FC), whereas the second method called 'NOVC' uses only the FCs. The standard tracking method gives a factor of two better resolution than the NOVC method [Ack98] . For 1996 only NOVC tracking was performed. To be able to compare the results of the two methods, two different data productions were studied. The 1997 b4 production uses standard tracking while the 1997 c1 production uses NOVC tracking. For both datasets the same slow control information (except for the high voltage trips in the VCs and DVCs) was used. This means that the data quality cuts select the same bursts. The only difference is which tracks are found and their angular and momentum resolution. In figure 3.6 it can be seen that for $p \geq 20$ GeV

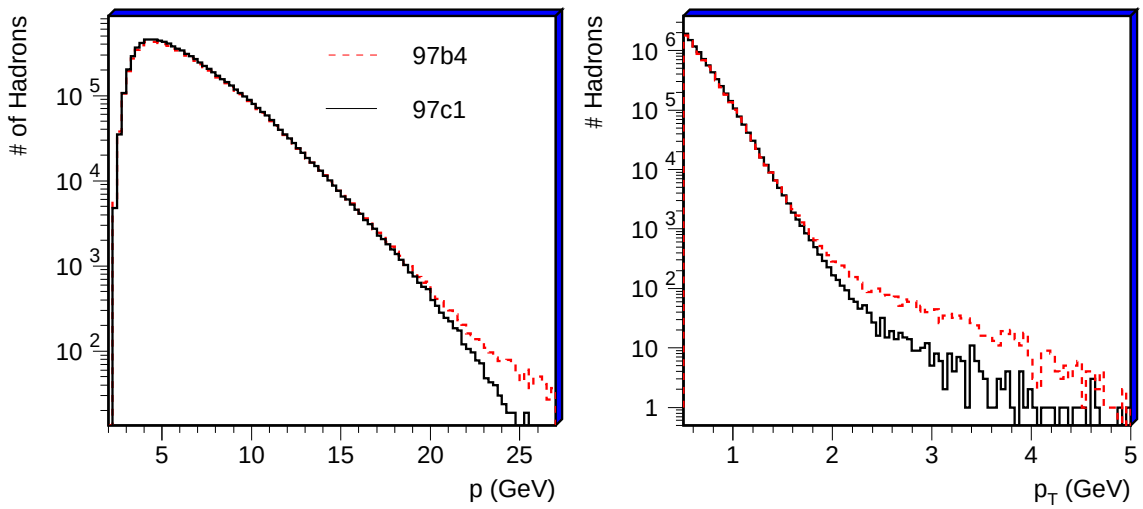

Figure 3.6: Momentum and transverse momentum distribution of hadrons in the 1997 b4 (STD) and 1997 c1 (NOVC) productions. The deviation in the hadron yield in p_T starts at ≈ 1.5 GeV.

and $p_T \geq 1.9$ GeV about twice as many hadrons are found with STD than with NOVC tracking. A study of the kinematic distributions of hadrons in this momentum range revealed that most of the excessive hadron tracks in 1997 b4 are apparently located in a band on the top and bottom edges of the detector. The reason for this excess has not yet been found. Additional studies on DIS positrons and semi-inclusive hadrons have been performed. No such tracks could be found in both cases, probably because of the low average θ of the positrons and the lower average momentum of the semi-inclusive hadrons. Since the bands look very much like an artifact it was decided to continue work with the 1997 c1 production despite its lower angular resolution.

3.3 Results for the 1996 and 1997 Hadron Asymmetries

3.3.1 Asymmetries and Kinematic Correlations

For the final analysis the 1996 c1 and 1997 c1 productions were studied using the data quality and track selection as described in the two previous sections. To reduce the systematics introduced by the different cuts on the μDSTs and trigger thresholds, only the 1996 period with the low calorimeter threshold for trigger 21 is used and a cut of $y \leq 0.85$ is imposed on single hadron tracks in 1997. Since the asymmetry is a ratio of cross sections, the number of hadrons detected in each

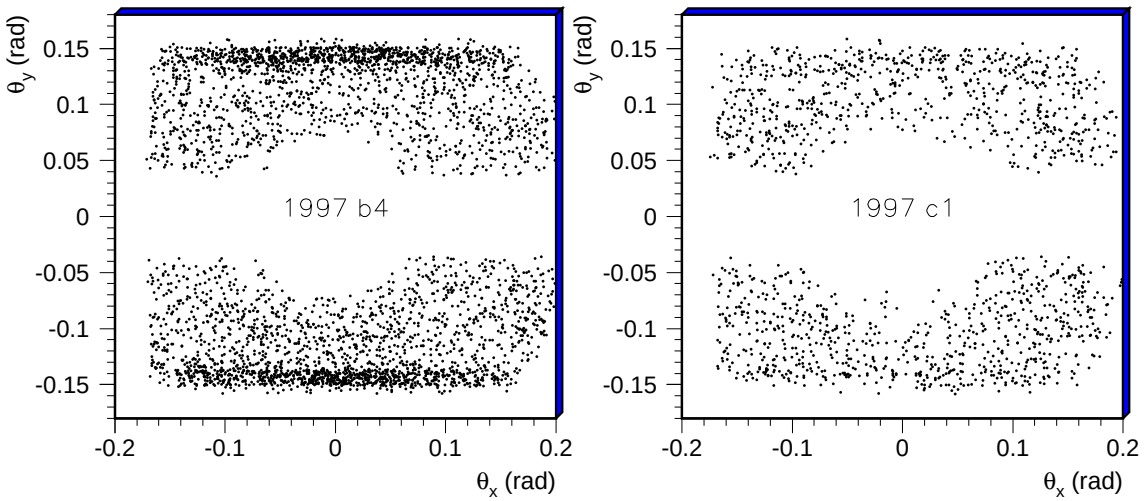

Figure 3.7: This plot shows essentially the geometrical position of each track in the detector requiring $p_T \geq 1.9$ GeV. The bands on the edges at $0.12 < \theta_y < 0.15$ rad are only there in 1997 b4.

spin state needs to be weighted with the integrated luminosity and averaged with the polarization of that spin state. The detector acceptance and efficiencies did not change over the measuring period, so the asymmetry can be calculated using:

$$A_{\parallel} = \frac{N^{\rightleftarrows} L^{\rightrightarrows} - N^{\rightrightarrows} L^{\rightleftarrows}}{N^{\rightleftarrows} P^{\rightrightarrows} + N^{\rightrightarrows} P^{\rightleftarrows}} \tag{3.8}$$

$$\text{where} \quad L^{\rightrightarrows(\rightleftarrows)} = \sum_{bursts^{\rightrightarrows(\rightleftarrows)}} L_i^{\rightrightarrows(\rightleftarrows)} \cdot t_i \cdot t_i^D \tag{3.9}$$

$$\text{and} \quad P^{\rightrightarrows(\rightleftarrows)} = \sum_{bursts^{\rightrightarrows(\rightleftarrows)}} L_i^{\rightrightarrows(\rightleftarrows)} \cdot t_i \cdot t_i^D \cdot P_{Bi} P_{Ti}. \tag{3.10}$$

$N^{\rightleftarrows(\rightrightarrows)}$ is the hadron yield with the target spin being antiparallel (parallel) to the beam spin. The error of the asymmetry is being calculated using Gauss' equation for the error propagation:

$$\Delta A_{\parallel} = \frac{L^{\rightrightarrows} P^{\rightleftarrows} + L^{\rightleftarrows} P^{\rightrightarrows}}{\left(N^{\rightleftarrows} P^{\rightrightarrows} + N^{\rightrightarrows} P^{\rightleftarrows}\right)^2} \sqrt{\left(N^{\rightrightarrows}\right)^2 N^{\rightleftarrows} + \left(N^{\rightleftarrows}\right)^2 N^{\rightrightarrows}}. \tag{3.11}$$

The hadron and pion asymmetries vs. transverse momentum p_T are shown in figure 3.8. In both years, for $p_T \leq 1.0$ GeV ($p_T \leq 1.2$ GeV) the asymmetry is close to zero for positive (negative) particles. At larger p_T it is positive for positive hadrons and slightly negative for negative hadrons. The identified pions, especially the positive ones behave differently (at least in 1997). Approximately 80% of the hadrons in HERMES are pions, so if the same momentum cut is placed on all hadrons as on the pions, their $A_{\parallel}$ should overlap to a large degree. That this is the case, is shown in figure 3.9. As can be seen in figure 3.9, the significance of all asymmetries is considerably reduced if the high-p hadrons are excluded. This suggests that the asymmetry versus p_T is also momentum dependent. The asymmetry versus momentum is shown in figure 3.10, where the transverse momentum has been integrated over. Basically the same behavior as for the p_T-asymmetries is seen. The asymmetry for 1996 is larger in the highest p_T bins, and slightly lower, but still within the statistical error bars in *most* of the p-bins. The issue of the deviations will be investigated below. Because of the limited acceptance and beam energy, and due to the y-cuts on the μDST and the p_T-cut the hadrons are correlated in their kinematical variables. Table 3.1 shows the average values.

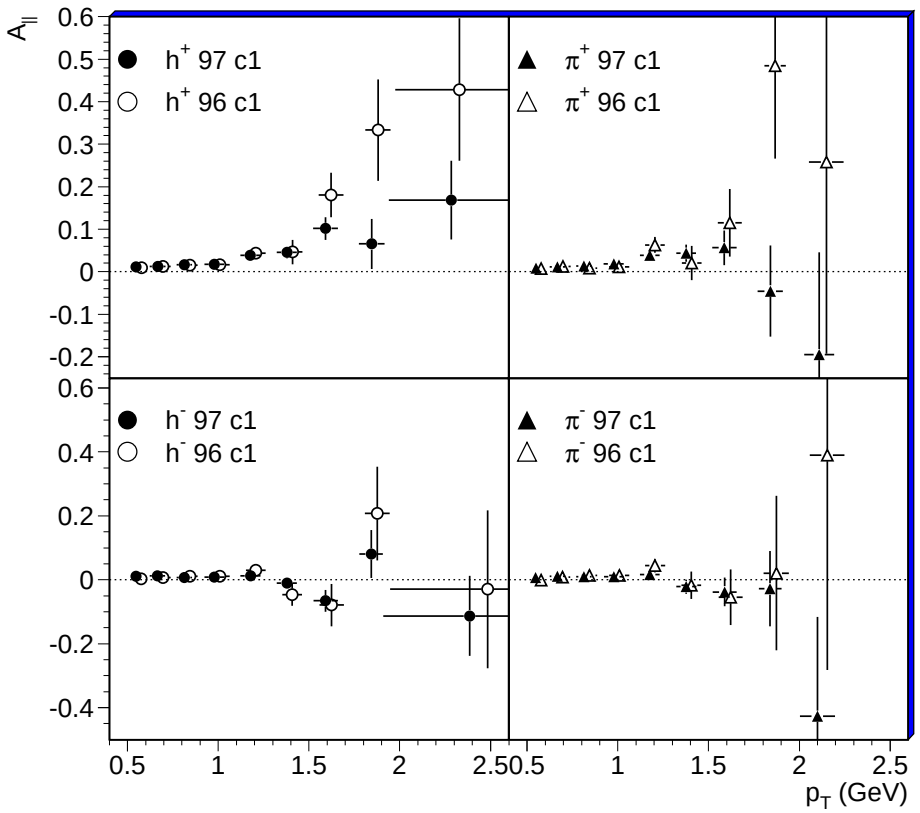

Figure 3.8: Inclusive double spin hadron (pion) asymmetries in quasi-real photoproduction for 1997 and 1996. The pions have $3.8 \leq p \leq 13$ GeV.

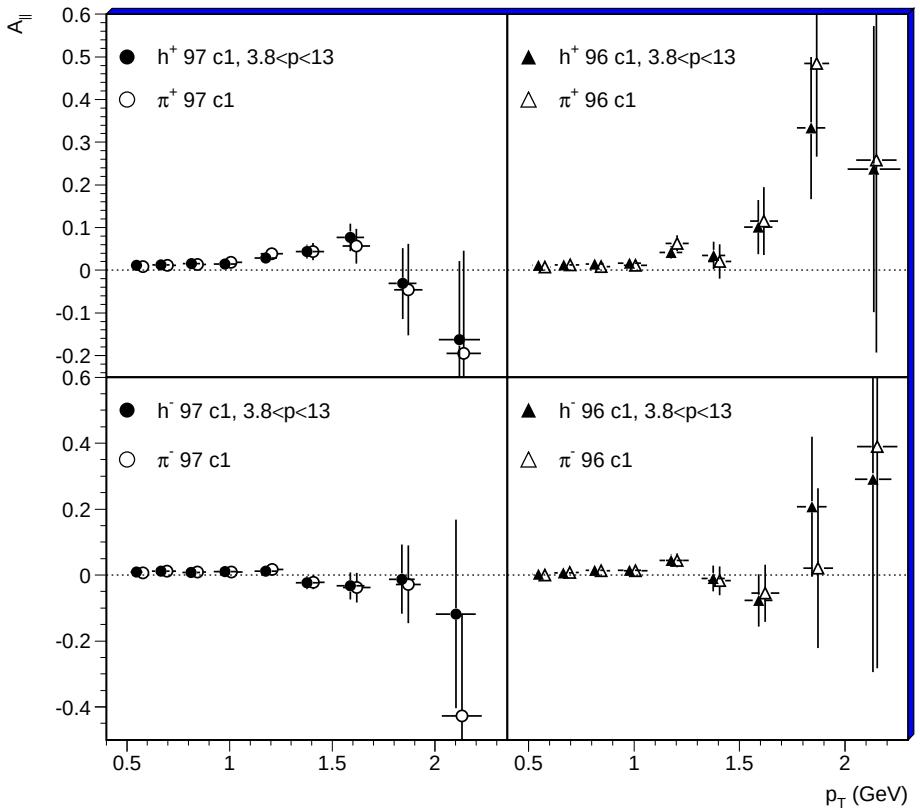

Figure 3.9: $A_{||}$ vs. p_T for pions and hadrons in the same momentum range $3.8 < p < 13$ GeV

.

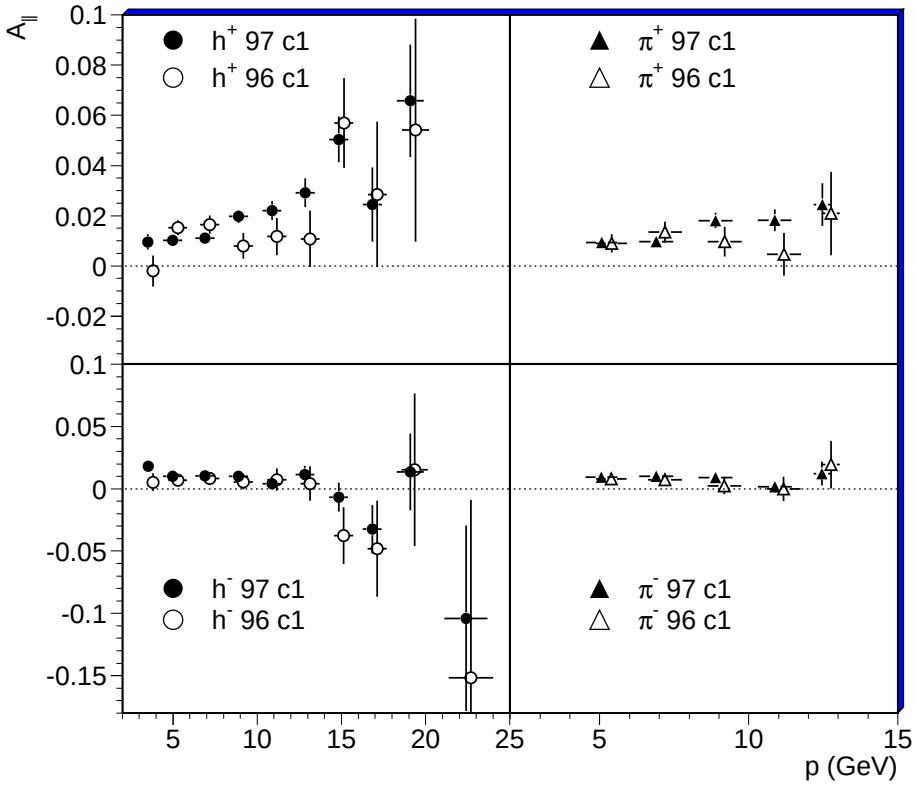

Figure 3.10: $A_{||}$ vs. p for hadrons and pions.

data	p_T-Bin (GeV)	$\langle p \rangle$ (GeV)	$\langle \theta \rangle$ (rad)	p-Bin (GeV)	$\langle p_T \rangle$ (GeV)	$\langle \theta \rangle$ (rad)
1996 c1	0.5-0.6	5.76	0.106	2-3.9	0.561	0.164
1997 c1		5.50	0.111		0.562	0.164
1996 c1	0.6-0.75	6.63	0.112	3.9-6	0.632	0.129
1997 c1		6.44	0.115		0.630	0.130
1996 c1	0.75-0.9	7.66	0.118	6-8	0.694	0.101
1997 c1		7.57	0.119		0.695	0.102
1996 c1	0.9-1.1	8.81	0.122	8-10	0.731	0.083
1997 c1		8.74	0.123		0.731	0.083
1996 c1	1.1-1.3	10.01	0.128	10-12	0.760	0.070
1997 c1		9.95	0.128		0.760	0.070
1996 c1	1.3-1.5	11.03	0.134	12-14	0.812	0.063
1997 c1		11.01	0.133		0.813	0.063
1996 c1	1.5-1.75	12.18	0.139	14-16	0.887	0.059
1997 c1		12.11	0.139		0.887	0.060
1996 c1	1.75-2	13.66	0.142	16-18	0.967	0.057
1997 c1		13.50	0.143		0.964	0.057
1996 c1	2-5	16.80	0.144	18-21	1.050	0.055
1997 c1		16.73	0.144		1.052	0.055
1996 c1				21-27	1.246	0.057
1997 c1					1.231	0.056

Table 3.1: The bins in p_T and p chosen for the asymmetries and the average values of the other kinematic variables in those bins for hadrons. For pions the average angles in p_T-bins are higher because of their restricted momentum range.

3.3.2 Systematic Errors and Normalization Uncertainty

The systematic error on $A_{\parallel}$ due to the beam- and target polarization uncertainties (added in quadrature) is (cf. section 3.1.2.):

$$A_{\parallel} \simeq \frac{1}{\langle P_B P_T \rangle} \Longrightarrow \frac{\Delta A_{\parallel}}{A_{\parallel}} = \sqrt{\left(\frac{\Delta P_B}{P_B}\right)^2_{scale} + \left(\frac{\Delta P_B}{P_B}\right)^2_{point} + \left(\frac{\Delta P_T}{P_T}\right)^2} \tag{3.12}$$

For 1996 the total relative systematic polarization error is 7.2%, for 1997 only 5.5%.
There is a large uncertainty in the determination of the luminosity at HERMES (see section 3.1.2), due to the incomplete fitting procedure and to fluctuations of the yields in high proton background or low lifetime conditions. To check the possibility of false asymmetries due to the luminosity normalization, the influence of different normalization schemes was investigated. As the standard normalization the fitted Bhabha rate corrected by the average trigger lifetime is used. This was replaced by first using the trigger lifetime for only one trigger (the HERMES main DIS 'trigger 21') as a correction to the fitted luminosity and secondly using the raw Bhabha rate instead of the fitted one. Under the assumption that the target density varies only slightly during a fill, it is also possible to use the beam current as a normalization. The deviation of $A_{\parallel}$ normalized in those three ways as compared to the standard normalization can be seen from figure 3.11. Shown is $1 - R$, where R is the ratio of the varied asymmetry ($A_{\parallel}^{rate}, A_{\parallel}^{curr}, A_{\parallel}^{fit-T21}$) to the standard one $A_{\parallel}^{fit}$. deviations from zero exist only in the low p_T-bins, where the asymmetry itself is close to zero and

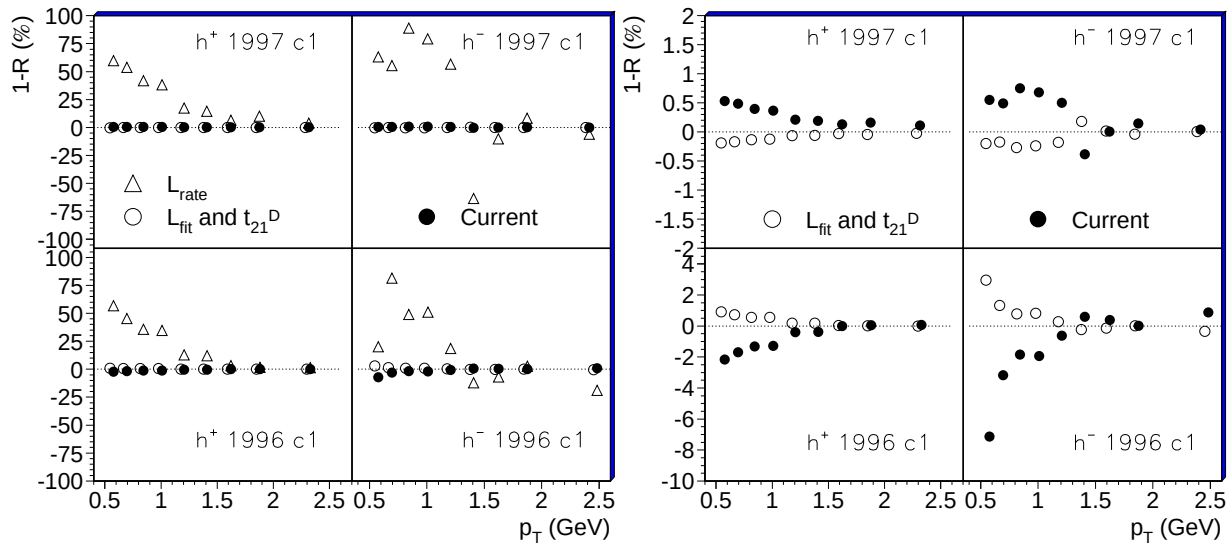

Figure 3.11: The deviation (in %) of $A_{\parallel}$ due to different normalizations. The right plot is blown up in scale, without the raw luminosity.

the ratio of $\frac{N^{\rightrightarrows}}{N^{\rightleftarrows}} \longrightarrow 1$. In this case R is most sensitive to normalization. The largest discrepancy comes from the raw Bhabha rate, which is not a surprise because at low p_T, $A_{\parallel}^{rate}$ is dominated by the Bhabha asymmetry itself (see section 3.1.2). Because of the residual electron polarization of the target electrons the bursts with parallel spins get a different weight than the ones with antiparallel spins, and this difference is of the same order of magnitude as $A_{\parallel}$ at low p_T. The variation of $A_{\parallel}^{curr}$ is at most 1% in 1997, and 3% in 1996 (neglecting the first bin of the negative hadron asymmetry). Overall the deviations are larger in 1996. In 1996 the lifetime of 'trigger 21' per burst sometimes differed from the lifetime averaged over all triggers which results in larger deviations of $A_{\parallel}^{fit-t21}$ in 1996 than in 1997. In general it can be said that normalization uncertainties are negligible in all bins where $A_{\parallel}$ is significantly larger than zero.

3.4 Systematic Studies on the 1996 and 1997 Asymmetries

The asymmetries for the two years look different in some of the p_T-bins, and in many of the p-bins. To check for nonstatistical effects a t-test on the disjunct samples is performed, where t is the ratio of the difference of $A_{\|}$ between the years to its error:

$$t = \frac{A_{\|}^{96} - A_{\|}^{97}}{\sqrt{\sigma_{96}^2 + \sigma_{97}^2}}; \quad \frac{\chi^2}{\nu} = \frac{1}{\nu} \sum_{Bins} \frac{\left(A_{\|}^{96} - A_{\|}^{97}\right)^2}{\sigma_{96}^2 + \sigma_{97}^2}. \tag{3.13}$$

Here ν is the number of degrees of freedom which in this case corresponds to the number of bins. Assuming that the same physics is underlying the data of both years, one would expect the average deviation $\langle t \rangle \simeq 0$ and χ^2 to be small. Figures 3.12 and 3.13 show the result of the test for $A_{\|}$ vs. p_T (9 bins) and p (10 bins) respectively. The negative hadron asymmetries agree quite well, although

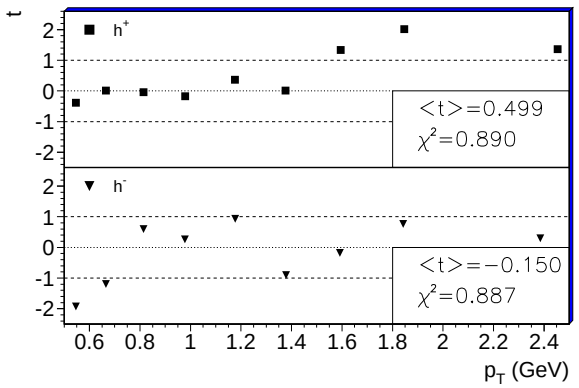

Figure 3.12: t-test for $A_{\|}$ vs. p_T

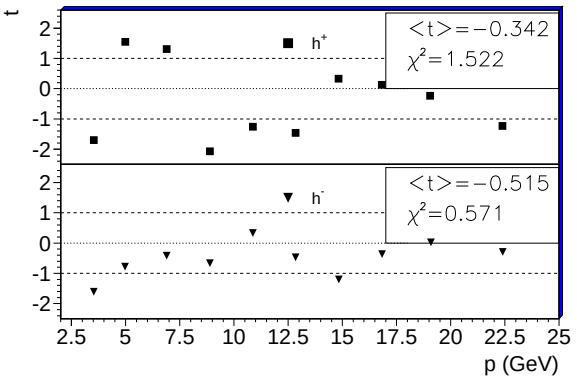

Figure 3.13: t-test for $A_{\|}$ vs. p

versus p the 1996 asymmetry is lower in eight of the ten bins. The positive hadron asymmetries always show a larger discrepancy, the χ^2 of the p-asymmetry of 1.5 means that the data overlap with a probability of only 15 %. Also the deviation of the h^+-asymmetry at high p_T could be a systematic effect. In the previous section it was mentioned that the experimental conditions where quite different in 1996 and 1997. Below studies are described which have been done to investigate if any of those differences could account for these effects. Similar effects have been seen also for the semi-inclusive hadron asymmetries, in particular for *negative* hadrons [Bai99].

3.4.1 Effects of the Experimental Environment on $A_{\|}$

Normalization

In the previous chapter it was shown that the influence of the normalization uncertainty is largest for small values of $A_{\|}$ and that it is only of the order of a few percent. An overall shift of the luminosity calibration can also not account for the deviation since it cancels in the calculation of $A_{\|}$. A polarization uncertainty on the other hand leads to a scale uncertainty in $A_{\|}$. The target polarization of 1996 was calibrated using the asymmetry of DIS positrons – this sample is completely disjunct to the hadron sample used in this analysis. To check if the calibration is the cause for the difference one can try to minimize χ^2 by multiplying one of the asymmetries with a factor f:

$$\frac{\chi'^2}{\nu} = \frac{1}{\nu} \sum_{Bins} \frac{\left(A_{\|}^{97} - f A_{\|}^{96}\right)^2}{\sigma_{96}^2 + \sigma_{97}^2} \tag{3.14}$$

If the scale of $A_{||}$ was to be redefined, a common factor f would minimize χ^2 for *all* the asymmetries measured. f was varied between 0.5 and 1.5, no such common factor was found, indicating that a normalization problem cannot explain the different asymmetries.

Background

The proton background in the HERMES region changes the response of some of the PID detectors. To see if high background also effects $A_{||}$ it would be the best to calculate it separately for different background conditions and check if there is a trend. With the statistics available it is only possible to compare the standard asymmetry with one where only data from low background conditions *pveto* < 1.5 kHz are taken into account. Figure 3.14 shows that the asymmetries with and without the cut on *pveto* basically sit on top of each other. Hence high proton background cannot be the reason for the differences in $A_{||}$ at high p_T. The asymmetries vs. p behave similarly.

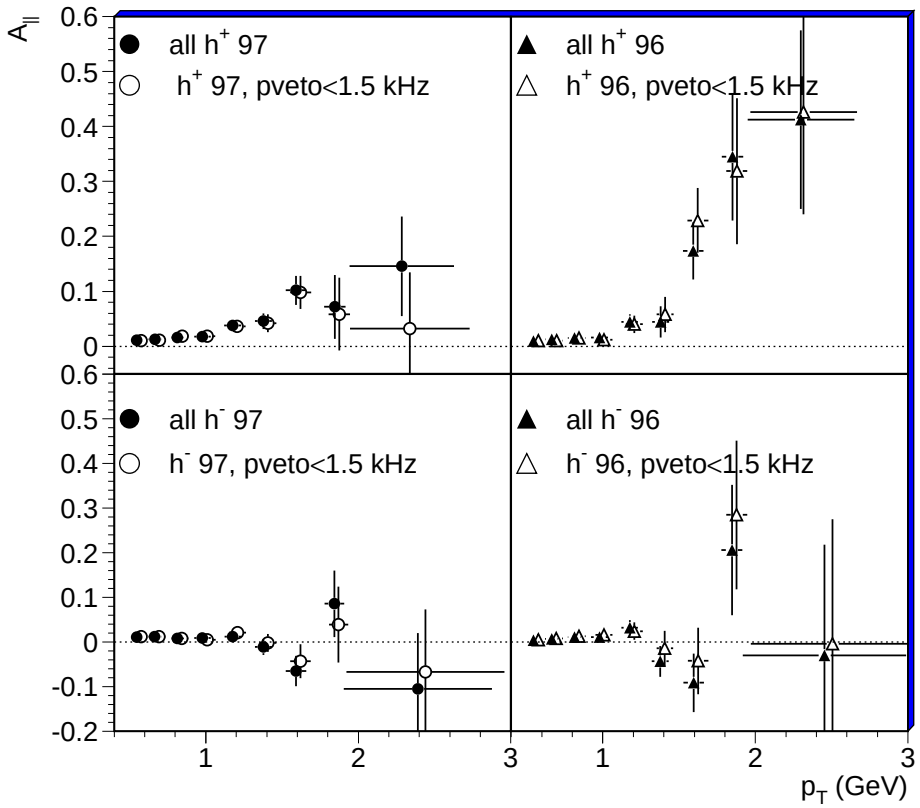

Figure 3.14: The asymmetry vs. p_T for data with low proton background compared to the one including all data. The ratio of low- to high background data is ≈ 3.7 in 1997 and ≈ 3.3 in 1996.

Acceptance and Detector Performance

Tracking efficiencies contribute to $A_{||}$ indirectly via the cut on events with a positron in the detector. If the efficiency for detecting a positron was worse in one year than in the other, more events with positrons not detected would contribute to $A_{||}$ resulting in a higher average Q^2. Since the contribution of different subprocesses to $A_{||}$ depends on Q^2, the asymmetry may be expected to change, although only very slightly because of the much lower statistics at higher Q^2. The tracking efficiency for the hadrons is not relevant as long as it is not spin dependent. For the NOVC tracking method no long term change in the tracking efficiency was observed. The only remaining way in which detection of positrons can be affected and which may be different between the two years

is then through misidentification of positrons as hadrons. In 1996 the Cherenkov detector had a lower efficiency because of some malfunctioning PMTs which were replaced during the shutdown in December 96. Other detectors were recalibrated, and the PID calculation scheme was changed. All this can of course result in different identification efficiencies for positrons. There is another aspect to be considered: The hadron sample will be 'contaminated' by hadrons from DIS events where the positron was scattered at large θ_x, but has $\theta_y \leq 0.04$ rad. In order to estimate the size of this effect and to reduce the dependence of $A_{||}$ to the identification efficiency for positrons, the asymmetry was calculated taking into account *all* hadrons regardless to whether there was a positron or not. If the

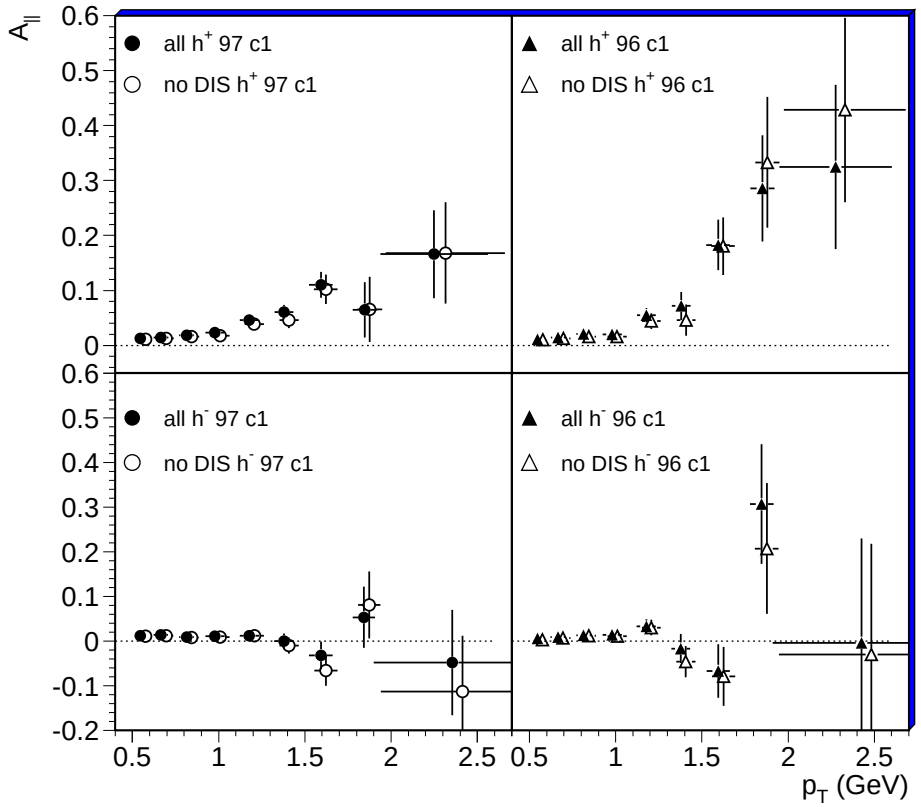

Figure 3.15: The asymmetry taking into account all hadrons regardless to whether there was a positron in the event or not is compared with the one without the 'DIS' events. χ^2 and $\langle t \rangle$ do not change significantly if one compares these asymmetries between the years.

asymmetries were to change with Q^2 and the detection efficiency for positrons differed significantly between 1996 and 1997, the asymmetries without the cut on DIS events should agree better. Figure 3.15 shows that $A_{||}$ is indeed slightly different with and without hadrons from the semi-inclusive events, but this might well be due to the different statistics involved. Nevertheless removing the DIS event cut does not reduce the discrepancies in the hadron asymmetries. The effect of events with higher Q^2 seems to be negligible because the sample is dominated by the photoproduction events. Further studies on the issue of DIS events in the photoproduction sample will be presented in section 4.1.3. For the asymmetry vs. p_T, $\chi^2 = 0.91$ and $\langle t \rangle = 0.537$ for positive hadrons, for negative hadrons $\chi^2 = 0.994$ and $\langle t \rangle = 0.017$. The asymmetry vs. p shows a similar behavior, here for h^+ $\chi^2 = 1.538$, $\langle t \rangle = -0.346$ and for h^- $\chi^2 = 0.395$ and $\langle t \rangle = -0.440$ were found.

3.4.2 Flux Correction to the PID Detector Likelihoods

The standard cut used in HERMES to separate hadrons from leptons (i.e. $e^{\pm}$) is on the value of PID3+PID5, the decadic logarithm of the combined likelihood that the response of the four PID

detectors corresponds to a lepton signal divided by the likelihood that it is a hadron signal:

$$\text{PID3} + \text{PID5} = \lg\left[\left(\frac{\mathcal{L}^e_{calo}\cdot\mathcal{L}^e_{pre}\cdot\mathcal{L}^e_{cer}}{\mathcal{L}^h_{calo}\cdot\mathcal{L}^h_{pre}\cdot\mathcal{L}^h_{cer}}\right)\left(\frac{\mathcal{L}^e_{TRD}}{\mathcal{L}^h_{TRD}}\right)\right]. \tag{3.15}$$

Here *calo*, *pre*, *cer*, and *TRD* denote the calorimeter, the preshower, the Cherenkov and the TRD respectively. $\mathcal{L}_i^{h(e)}$ is the likelihood function that a hadron (electron) causes a certain signal in the detector i. This likelihood ratio should only depend on the momentum of the particle. The left plot in figure 3.16 shows the PID3+PID5-distribution for positive particles for three momentum bins. Because the cross section is highest for small ν, the average momentum of the positrons (the right 'peaks') is higher than that of the hadrons. This is the reason why the minimum in between the peaks shifts to the left with higher momentum. Using a fixed cut for hadron-electron separation one would cut away too many hadrons at low momenta and leave too many positrons at high momentum. The actual *probability* that a signal *was caused* by a hadron (electron) is, according to

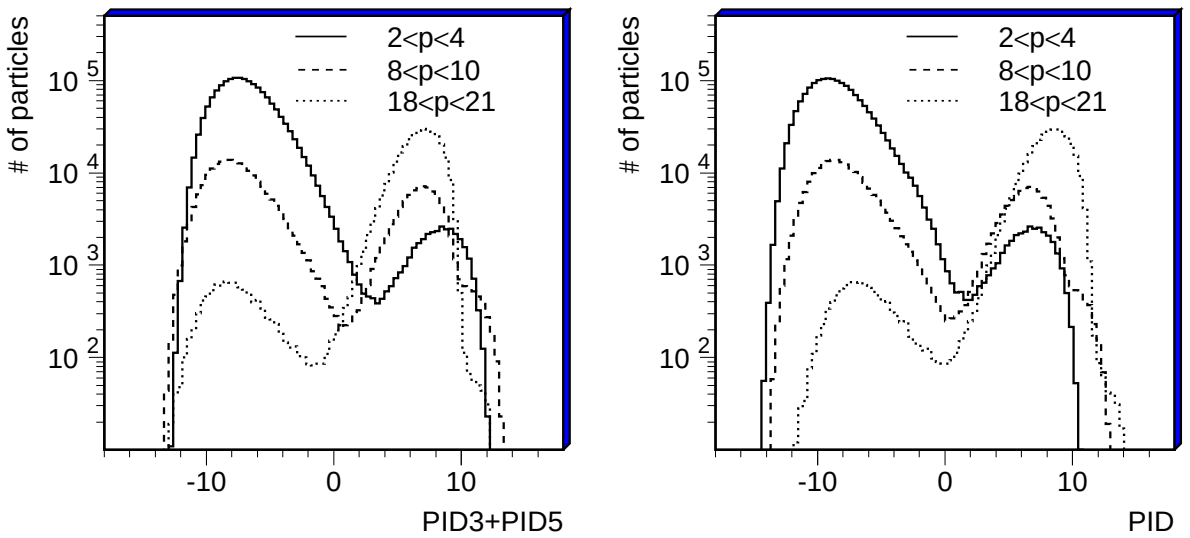

Figure 3.16: The PID distribution for positive hadrons at different momenta. For the left plot only PID3+PID5 is used, the right one uses the flux correction.

Bayes Theorem, the likelihood times the probability that a hadron (electron) was actually in the detector:

$$P_i^{h(e)} = \frac{\mathcal{L}_i^{h(e)}\cdot\Phi^{h(e)}}{\mathcal{L}_i^e\cdot\Phi^e + \mathcal{L}_i^h\cdot\Phi^h} \Longrightarrow \text{PID} \equiv \lg\frac{P^e}{P^h} = \text{PID3} + \text{PID5} - \lg\frac{\Phi^h}{\Phi^e} \tag{3.16}$$

The right plot of figure 3.16 shows that the valley between the two peaks does not shift much with momentum if one uses PID instead of PID3+PID5. The fluxes Φ^e, Φ^h have been calculated in an iterative procedure described in [Kai97], for all triggers. They depend on p and θ. Figure 3.17 shows the result for one θ-bin. The asymmetries are calculated with the smoothed flux correction valid for the corresponding year. It was also checked whether this flux correction has any significant influence on the asymmetries: Neither does the asymmetry of one year change much nor does the discrepancy between the two years become less. The χ^2 and mean t stay the same as without the flux correction. This can be understood from the fact that the correction either cuts away or adds statistics, but is not polarization dependent.
The effect of the flux correction can be seen if yield ratios between positive and negative hadrons are calculated. One would naively expect that the charged hadron ratio $R = \frac{N^+}{N^-}$ in p (p_T) bins would rise with the PID cut. A cut on PID3+PID5$\leq$0 leaves more positrons in the sample as a contamination to positive hadrons than cutting on PID3+PID5$\leq$-4. Looking at figure 3.18 one can see that the effect here is actually reversed if no flux correction is used. The reason is that the

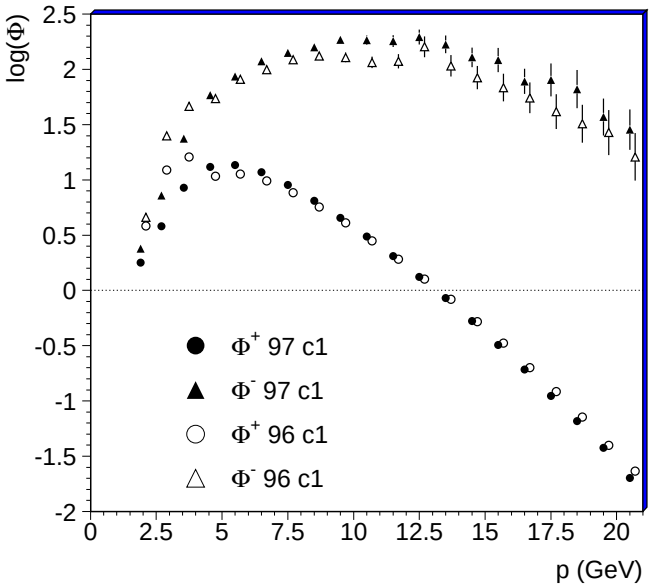

Figure 3.17: Fluxes for θ between 0.04 and 0.075 rad.The positive fluxes agree well between 1996 and 1997, but the negative fluxes for 1997 are systematically higher than the 1996 ones. The disagreement of the fluxes in the low momentum bins $p \leq 5$ GeV is due to the different y-cuts on the μDST level. For the other θ bins a similar behavior is seen.

harder the PID cut imposed the more 'good' negative hadrons are being cut out as compared to the positive ones. The contamination of positive hadrons is always larger because the beam particles are positrons. With the correction the highest ratio is always the one with the loosest PID cut as can be seen in figure 3.19. Between ratios with different PID cuts there are larger systematic differences because cut efficiencies and contamination are different for positive and negative hadrons. By raising the PID cut from -4 to 0 one gains in the cut efficiency but also the contamination will rise. The variation of the contamination with the PID cut is much larger for positive hadrons than for negative ones. Since the scattered DIS positrons have large average momenta the contamination is largest for positive hadrons at high momenta – and correspondingly high p_T. It is of the order of a few percent for PID<0 and drops rapidly if lower cuts are used. The ratios agree quite

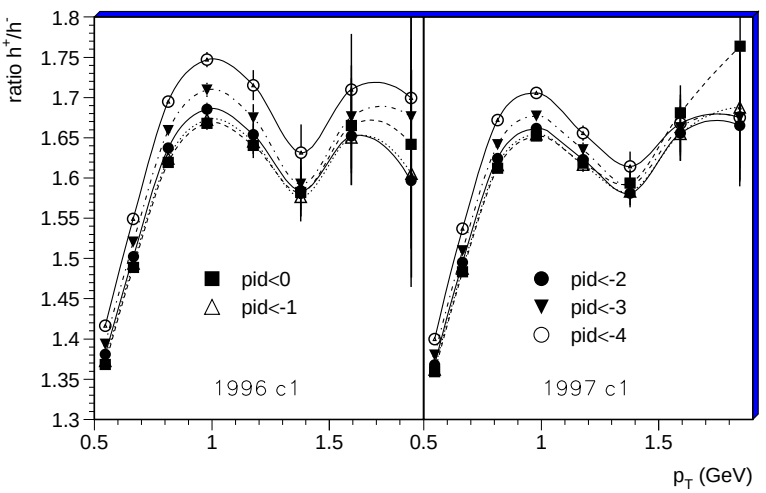

Figure 3.18: The yield ratio between positive and negative hadrons per p_T-bin with PID3+PID5-cut between -4 and 0. The ratios are most sensitive to the PID, because contamination with leptons and cut efficiencies are different for positive and negative hadrons.

well between the years. One can further improve the agreement between the ratios by correcting the yield of hadrons with their PID cut efficiency and contamination (see section 4.3 below). The corrected ratio then becomes:

$$R_{corr} = \frac{N^{h+}}{N^{h-}} = \frac{N^{+}(1-C^{+})\cdot\epsilon^{-}}{N^{-}(1-C^{-})\cdot\epsilon^{+}}. \tag{3.17}$$

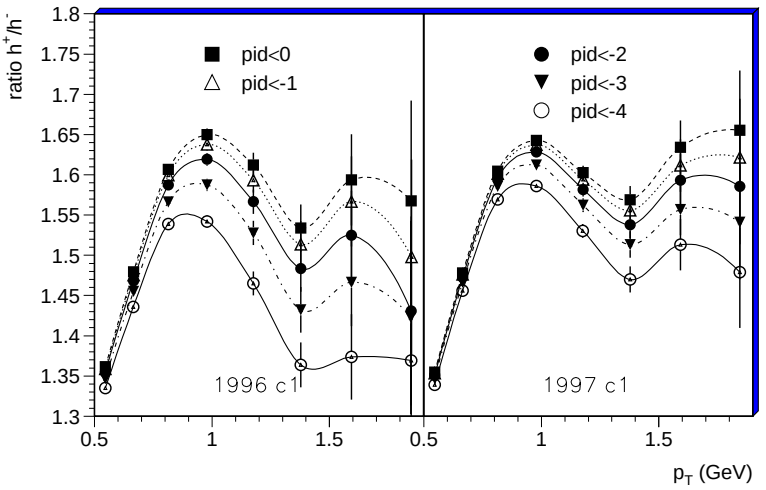

Figure 3.19: The hadron yield ratio with the PID3+PID5 corrected for the fluxes. The change of the ratios in absolute value and relative to each other as compared to the uncorrected ratios is clearly visible. The agreement between the two years is good, the $\langle t \rangle$ is -0.067, the reduced $\chi^2 = 0.799$.

A fraction $C^{\pm} \cdot N^{\pm}$ of the particles are not hadrons but contaminating leptons. Since the efficiency is lower than unity, only a fraction $\epsilon \cdot N^h$ of *all* hadrons is being counted below the PID cut. For the ratio in p-bins, where the dependence on the contamination is largest, the $\langle t \rangle$ reduces from 0.201 to 0.129 and χ^2 changes from 0.573 to 0.510. Overall the effect is small compared to the systematic shifts when varying the PID cuts.

3.4.3 PID Cut Efficiency and Positron Contamination

Every full track in the detector has a PID value assigned. This means, the probability that this track is a hadron is

$$\mathrm{PID} = \lg \frac{P^e}{P^h} \Longrightarrow P^h = \frac{1}{1+10^{PID}}, \quad \text{because } P^e + P^h = 1. \tag{3.18}$$

$P^e + P^h$ is the probability for the particle being either a hadron or a lepton. The probability, that the track is an electron or a positron is then:

$$P^e = \frac{10^{PID}}{1+10^{PID}}. \tag{3.19}$$

Placing a PID cut on a particle sample to select e.g. hadrons means that one would loose in every PID bin *i higher* than the cut a number of hadrons $N_i P^h$, for N_i being the number of particles in the bin. So the efficiency ϵ for finding hadrons with a particular PID cut adds up to [Gär00]:

$$\epsilon = \frac{\sum_{PID-min}^{PID-cut} \langle P^h \rangle_i \, N_i}{\sum_{PID-min}^{PID-max} \langle P^h \rangle_i \, N_i}, \tag{3.20}$$

where $\langle P^h \rangle_i$ is the average hadron probability per bin and PID-min (-max) are the minimum (maximum) PID values, set here to -(+)17. Correspondingly there is a finite probability in every PID bin lower than the cut that the particle is actually a lepton. The contamination C of the hadron sample with leptons can be calculated as follows:

$$C = \frac{\sum_{PID-min}^{PID-cut} \langle P^e \rangle_i \, N_i}{\sum_{PID-min}^{PID-cut} N_i} \tag{3.21}$$

Both quantities depend on momentum and θ, as the PID detector responses are momentum dependent, and the particle fluxes are functions of (p, θ). Since asymmetries are only calculated for one charge, the PID cut efficiency has no influence on them. For the positive hadron asymmetry

the contamination with positrons is important because the positrons (a mixture of DIS positrons and positrons from charge symmetric decays) do have their own asymmetry. If one uses loose PID cuts for hadrons the asymmetry should be corrected for the positron asymmetry. Also electrons from the charge symmetric background have a small asymmetry, but the electron contamination is approximately ten times lower than the positron contamination. The corrected asymmetry can be calculated with the assumption that the number of particles N counted in each spin state consists of positive hadrons N^{h+} and positrons N^{e+}, whose asymmetry is separately measured:

$$A_{\parallel}^{meas} = \frac{N^{e+}}{N} A_{\parallel}^{e+} + \frac{N^{h+}}{N} A_{\parallel}^{h+} \quad \Longrightarrow \quad A_{\parallel}^{h+} = \frac{A_{\parallel}^{meas} - C A_{\parallel}^{e+}}{1 - C} \tag{3.22}$$

The asymmetry for positrons versus p and p_T is shown in figure 3.20. Figure 3.21 shows in percent how large the corrections are which are finally applied to the asymmetry with PID$\leq$-1. The

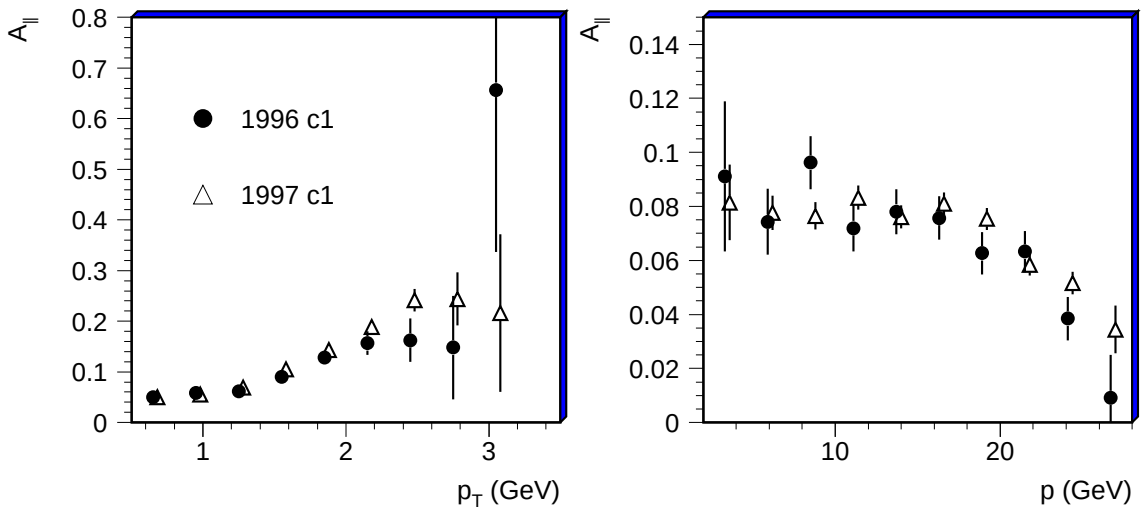

Figure 3.20: The positron asymmetries for 1996 and 1997 vs p_T and p.

contribution of the statistical error of the positron asymmetry to the error of the corrected hadron asymmetry is negligible because it is weighted with the contamination. Although the positron contamination for 1996 is different from 1997, the correction does not change anything with respect to the compatibility of the two datasets. Also the combination of the asymmetries of each year with different PID cuts shows no significant effect. All this takes into account positron contamination within the regular PID scheme used in HERMES. It does not rule out the possibility of a *misidentification* of particles.

3.4.4 PID Detector Responses

It was mentioned above that the response of the PID detectors is momentum dependent. The Cherenkov detector can only identify positrons up to a momentum of about 4 GeV, because at higher momenta pions also emit Cherenkov light. The other detectors are efficient only at higher momenta, starting at about 5 GeV. For the particle identification the Cherenkov detector has the highest weight at low momenta whereas at higher momenta the TRD and the calorimeter are the most important detectors. Studies were performed to check if inefficiencies of these two detectors can lead to misidentification of particles. Comparing data from 1996 and 1997 one should know that detector calibration and the extraction of the PID values were done with different schemes in each year, but the 1997 PID uses parent distributions from 1996 data.

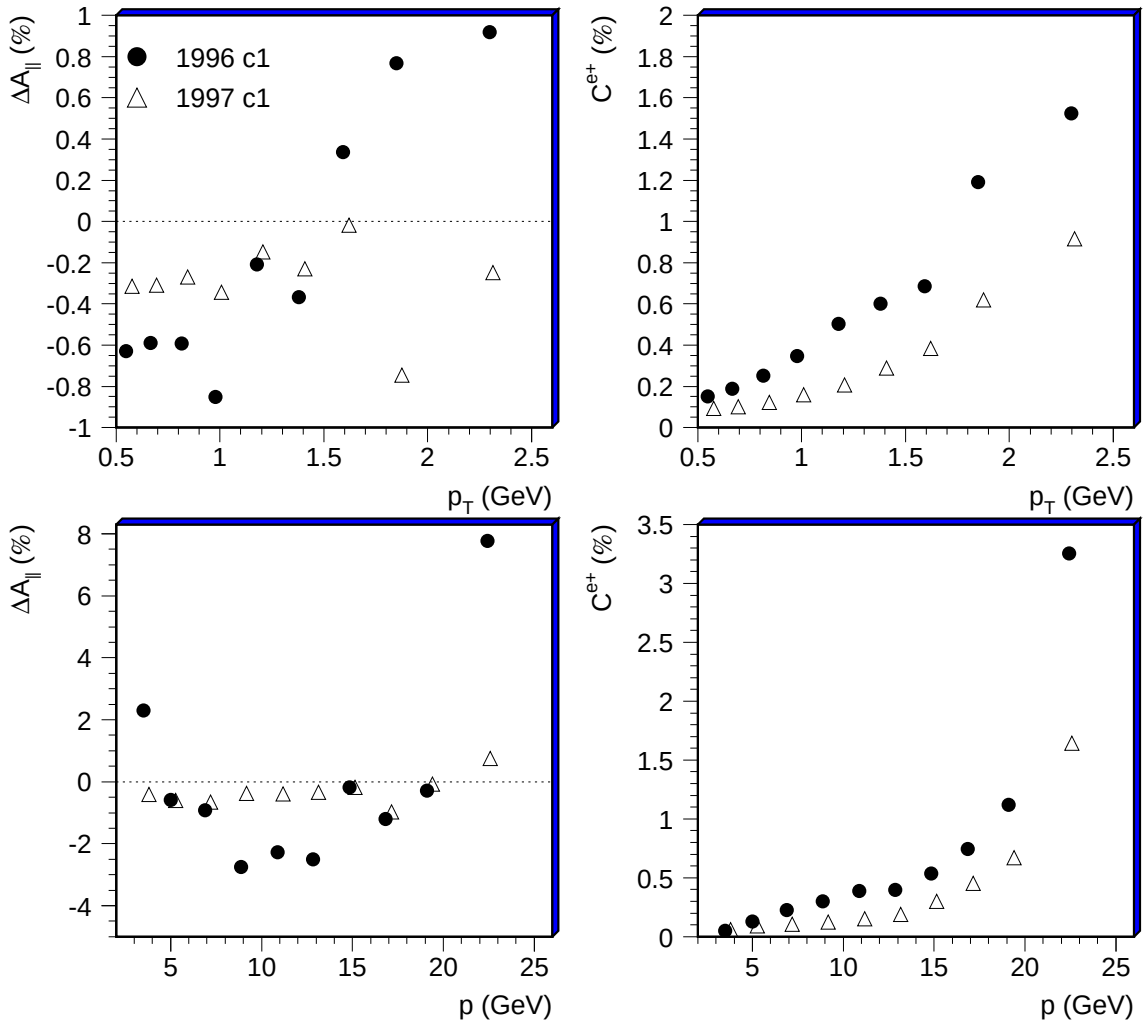

Figure 3.21: The effect $\Delta A_{||} = \frac{A_{||}^{corr}}{A_{||}} - 1$ of the correction to the positive hadron asymmetry with PID$\leq$-1. The correction is not more than 1% for PID$\leq$-1 for the p_T-asymmetry, and only slightly larger for the 1996 p-asymmetry. The contamination is shown on the right side, it is always more in 1996 than in 1997.

TRD Response for Hadrons

By imposing a cut on PID3<0 (the likelihood ratios of the Cherenkov-, calorimeter- and preshower responses) it is possible to identify hadrons independently of the TRD response and thus study the behavior of hadrons in the TRD (it should be noted that PID3<0 is a very loose cut, in order to get a clean hadron sample for the parent distributions hard cuts on the response of the three detectors are applied). The data were divided into top and bottom tracks and into momentum bins. The average pulse a hadron gives per TRD module (truncated mean) is around 11-12 keV. Figure 3.22 shows the average response per momentum bin. One can see that the truncated mean rises with momentum for positive as well as for negative particles, as it can be expected from the rise of $\frac{dE}{dx}$. At very high momenta the slope for positive particles becomes much steeper whereas for negative ones it does not. This is due to a contamination of the sample with DIS positrons. Especially for 1997, but also in 1996 there seems to be a difference in the response for the top and bottom TRD modules. The distributions are shifted to higher values (by about 1 keV) for the

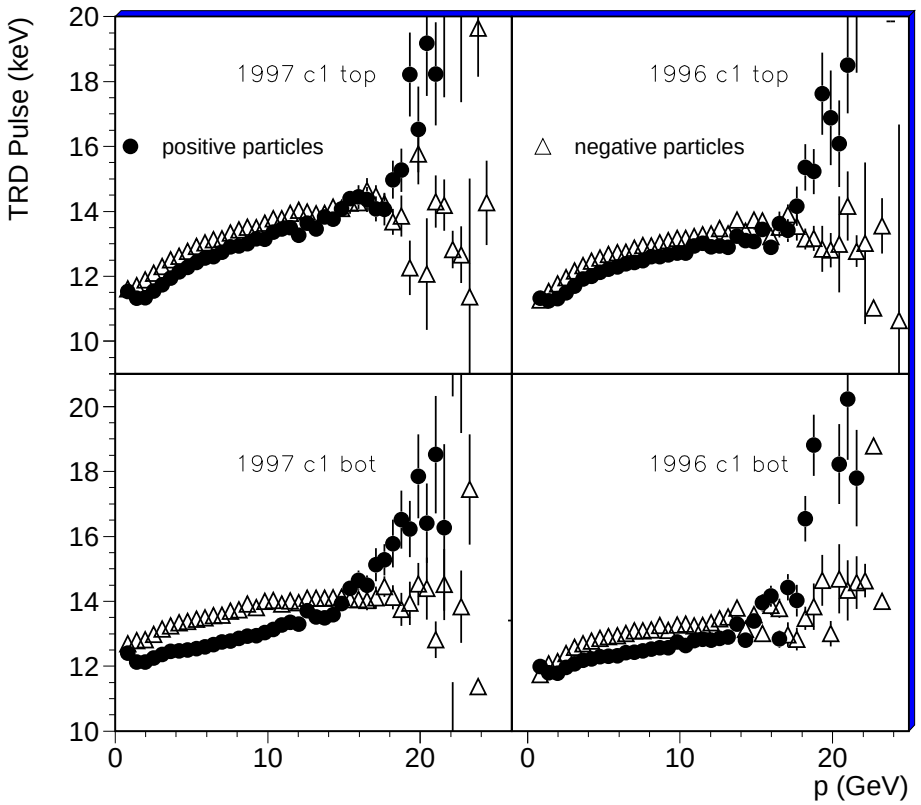

Figure 3.22: The the truncated mean response of the TRD modules for hadrons identified by PID3<0. In order to avoid difficulties arising from the production of high energy knock-on electrons by hadrons, the module with the highest signal is excluded from averaging. This reduces the long tail of the hadronic distribution at large response values.

bottom detector. This results in a shift in the PID5 (likelihood ratio for the TRD) of about one. The parent distributions from which the PID values are being extracted have not been calculated for top and bottom separately so far.

Calorimeter Response for Hadrons

Similarly to the TRD the calorimeter response to hadrons can be studied by selecting particles with PID5<0. On average at momenta higher than about 5 GeV hadrons deposit about one half of their energy in the calorimeter, so that $E_{calo}/p \approx 0.5$. At lower momenta the tail of the hadron distribution towards higher values of E_{calo}/p is much larger, and the mean of the response ratio is $E_{calo}/p \approx 0.7$. Electrons or positrons have $E_{calo}/p \approx 1$ throughout the entire momentum range, in a much narrower peak. The average calorimeter response versus momentum is shown in figure 3.23. No difference can be seen between bottom and top detector. The rise in the response for positive particles with momenta greater than 15 GeV is again due to contamination with DIS positrons (PID5<0 is not a very stringent cut on the hadron sample). The parent distributions for leptons as well as hadrons also show a long tail toward ratios $E_{calo}/p > 1$. With positrons this can happen quite naturally: If a bremsstrahlung photon is radiated off a highly energetic positron *before* the magnet, a lower positron momentum is determined but because of the small deflection angle at high momenta both the photon and the positron hit the same cells in the calorimeter. Their energy deposition cannot be distinguished, so in this case E_{calo}/p will be greater than one. Hadrons do not radiate bremsstrahlung, so it is not clear which mechanism can cause their E_{calo}/p to take values of up to 10 at low momenta, and still to about 1.5 to 2 for high momenta. This effects about 4% of

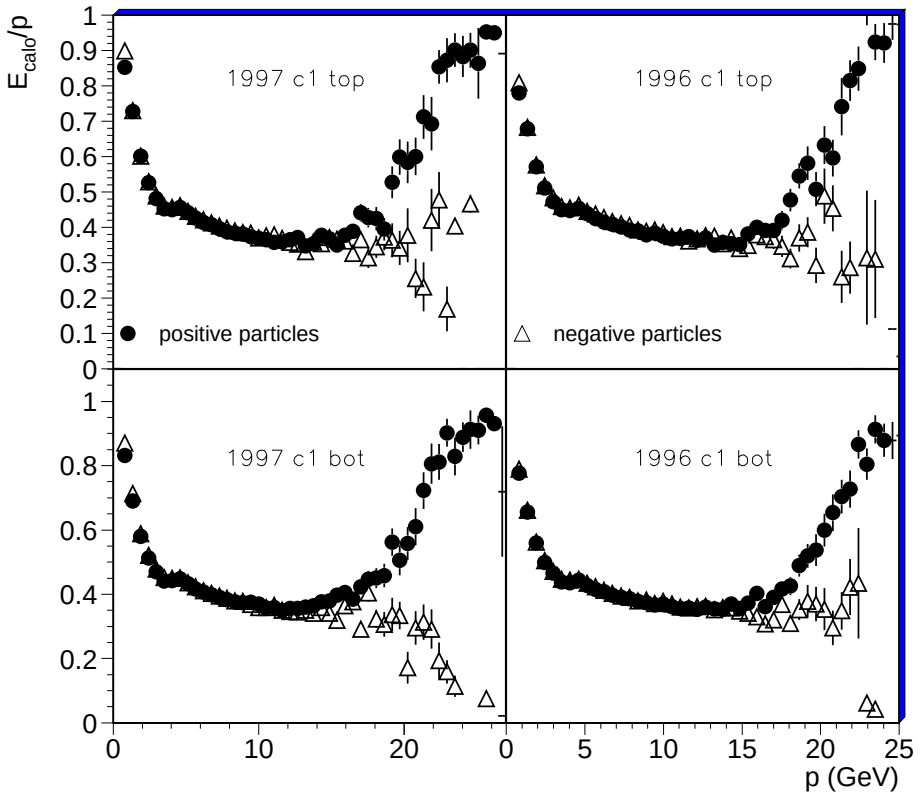

Figure 3.23: The ratio of deposited energy in the calorimeter to momentum E_{calo}/p for particles with PID5<0 . At low momenta, the average response is high and the peak is very broad, at higher momenta the average is lower and the peak is narrower.

the data. Depending on momentum, most of them will will get a PID2 (combined likelihood ratio of calorimeter and preshower) value identifying them as hadrons. Only at very high momenta there seem to be more of them among the positive particles which in the end up being identified as leptons.

Contradicting Responses

The final decision on whether a particle is a lepton or a hadron is made on the combined likelihood ratios of all PID detectors (sum of PID3 and PID5). This value can be lower than zero even if the two PID values have opposite signs, meaning that their responses contradict each other. This may be due to inefficiencies of one of the detectors involved or to the statistical nature of the interaction of particles with the detector material. For instance a hadron can start to shower in the TRD and thus leave more energy than expected in the modules, or the TR of a positron might not be detected. From figure 3.24 one can see that most of the particles (80-90%) with contradicting responses are identified as hadrons, many of them with a rather low PID3+PID5 value where the generically calculated contamination would be negligible. This effects about 10% of the data in 1996 and 6% in 1997. That there are less of these 'problematic' hadrons in 1997 is not because the detector response was different then but because new parent distributions were used to calculate the PID3 and PID5 values [Wen99]. One can for sure get a cleaner hadron sample if PID3<0 *and* PID5<0 are required, which makes it more likely that both detector combinations were working properly, and so decreasing the probability of misidentification of leptons as hadrons. The dependence of the data that are cut out by this additional requirement on several kinematical variables was checked. As an example, the ratio Δ of the number of cut out particles to the number of all particles with PID3+PID5<0 as a function of θ_y is compared to the average PID5 distribution in this variable in

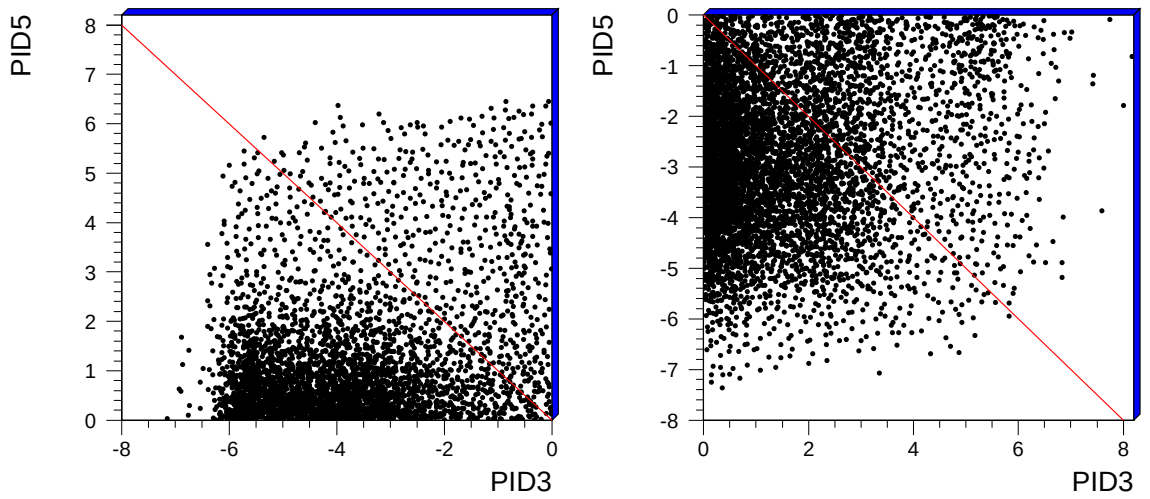

Figure 3.24: The distribution of data PID5 vs. PID3 for the two cases where contradicting responses are detected, PID5>0 and PID3<0 (left) and vice versa (right). The data below the lines have PID3+PID5<0. (These are 1997 data, but the problem exists in 1996, too.)

figure 3.25. For the 1997 data a correction of the TRD response in y was applied which explains

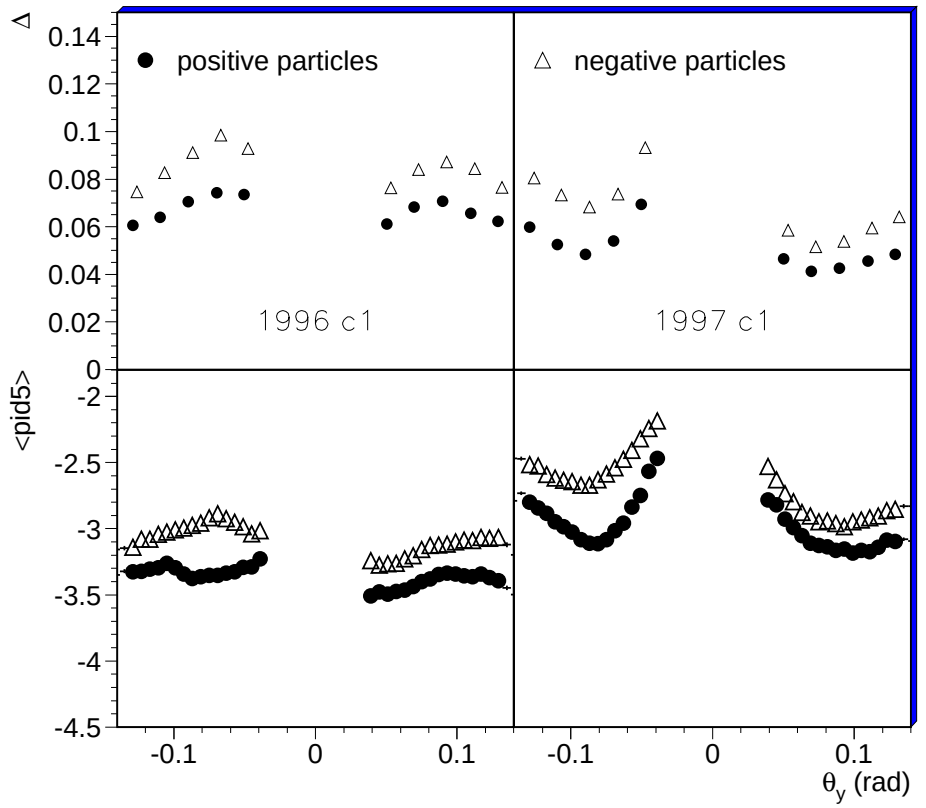

Figure 3.25: The ratio $\Delta = 1 - \frac{N_{new\ PID\ cut}}{N_{PID3+PID5<0}} = \frac{N_{cut\ out}}{N_{PID3+PID5<0}}$ versus θ_y. The shape of Δ is the same as the average PID5 in the lower two plots. The same feature shows up if one plots the θ_x distributions.

the difference in the shape of PID5 between 1996 and 1997. The same difference can also be seen for Δ, pointing to the possibility that the contradiction of the two PID values is a result of the

TRD calibration rather than a physical effect (There is a one-to-one correlation between the TRD truncated mean and PID5, the shapes look alike). The asymmetries compared before and after the cut show no significant effects. All asymmetries move because of the change in statistics, but only for the 96 asymmetry in p_T there might be a slight systematic shift to lower values, but which is still within the error bars.

3.4.5 Merging of the Hadron Asymmetries

In the last section several systematic studies of the two data sets of hadron asymmetries on hydrogen were described. Although there are discrepancies mostly in the positive hadron asymmetry which might be non-statistical, the χ^2, a measure of the compatibility of data sets, is mostly about one or lower, except for the positive hadron asymmetry versus p, where it is around 1.5. This means the probability that they represent the same physical quantity is high, around 0.9 (0.15 for the positive hadron asymmetry versus p). The experimental conditions and detector performance in 1996 and 1997 have been compared, but despite the fact that they were quite different no clear systematic effect could be seen. Thorough studies on similar differences in semi-inclusive hadron asymmetries have been carried out [Bai99] with the same conclusion. A slight effect was seen in [Bai99] due to the proton background, but it is not quite clear which mechanism should make it polarization dependent. It has been suggested that the *beam helicity*, which for most of the 97 data was opposite to that of 96, induces different *physics*. Studies on that issue have been done but due to the low statistics of the 1997 data with the same beam spin orientation as in 1996 no conclusion could be drawn.

Inclusion of all Available Data

As it was mentioned in the beginning of this section, for the comparison of the two years reduced data sets were used: The 1997 data had an additional y-cut on single tracks of $y \leq 0.85$ and for 1996 only data of the time when the calorimeter threshold for trigger 21 had been the same as in 1997, 1.4 GeV, has been considered. Statistics could be improved by including the data that were cut out. For 1997 this means that the statistics of the first two p-bins between 4 and 6 GeV become higher if the the cut on $y < 0.93$ is used instead of $y \leq 0.85$. There the asymmetry itself is almost zero. The effect on the two bins in p is clearly within the error bars. An even smaller effect is seen for the first two p_T-bins where the statistics also increases because of the correlation between p and p_T. The total change in statistics is around 10 %. For 1996, data from the first $\approx$ 500 runs are added, resulting in a p-dependent change in the statistics of 15-20 %. Trigger 21 is optimized for the signal of an electron or positron, which leaves all its energy in the calorimeter. A hadron only leaves $\approx \frac{1}{2}$ of its energy there, so there is no reason why a different trigger threshold should change any physics related to the hadrons, except that events with only one hadron with $p < 7$ GeV do not fire the trigger. Because of the change in statistics the data points of the 1996 asymmetries are allowed to move, any change is within their statistical error bars, as can be seen in figure 3.26. So for the merging the full datasets available from both years are used, each of the positive hadron asymmetries is corrected for the positron contamination.

Combination of the 96 and 97 Data

The data for each asymmetry are combined by calculating the error weighted mean and standard deviation using

$$A_{\parallel} = \frac{\frac{A_{\parallel}^{96}}{\sigma_{96}^2} + \frac{A_{\parallel}^{97}}{\sigma_{97}^2}}{\frac{1}{\sigma_{96}^2} + \frac{1}{\sigma_{97}^2}} \text{ and } \sigma^2 = \frac{1}{\frac{1}{\sigma_{96}^2} + \frac{1}{\sigma_{97}^2}} \tag{3.23}$$

The final results are shown in figure 3.27 and figure 3.28. For the systematic errors only the

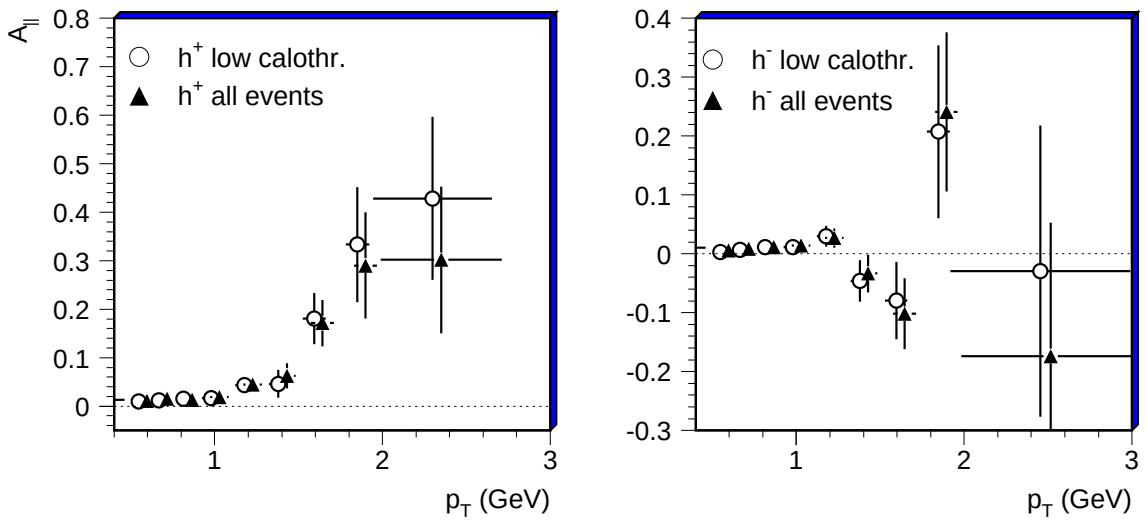

Figure 3.26: The positive and negative hadron asymmetries with all 96 data as compared to the data with calorimeter threshold of 1.4 GeV. All asymmetries move only within the error bars. The left plot shows the positive hadron asymmetry, the right one shows the negative hadron asymmetry.

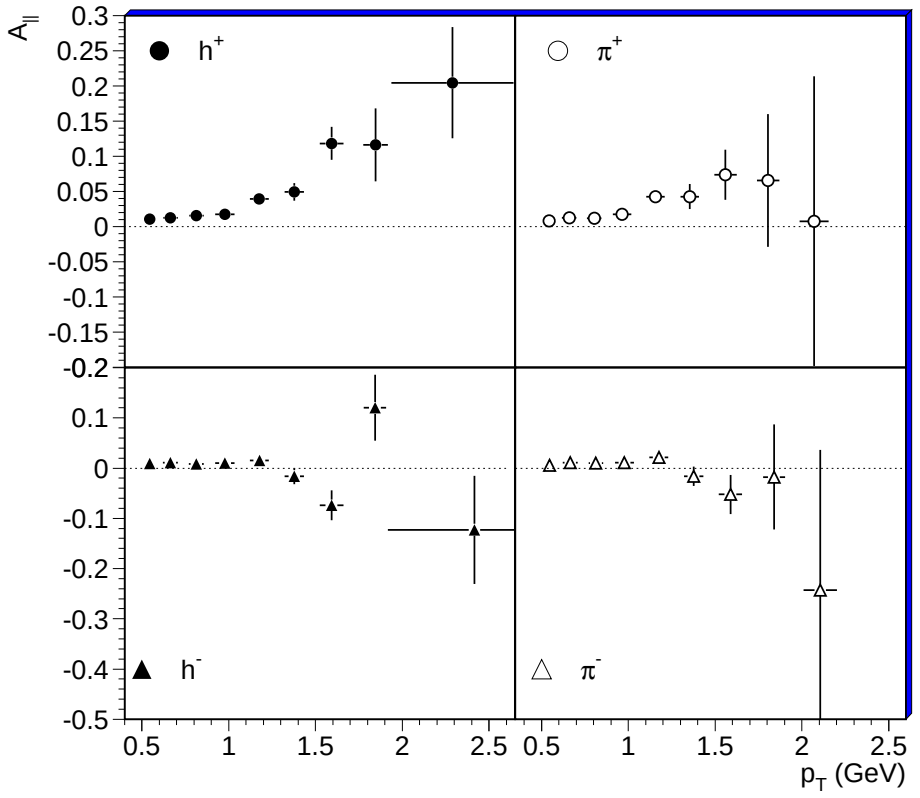

Figure 3.27: The merged hadron and pion asymmetries versus p_T. The error bars represent statistical errors only. The relative systematic error is $\simeq 6.0\%$, independent of p_T. The positive hadron asymmetry is corrected for positron contamination. Because of $p^\pi < 13$ GeV, the contamination for π^+ always stays below 0.1%, so no correction is applied for them.

polarization uncertainties are taken into account. The uncorrelated parts of the beam and target polarization errors for the total asymmetry are being calculated just like the error weighted mean,

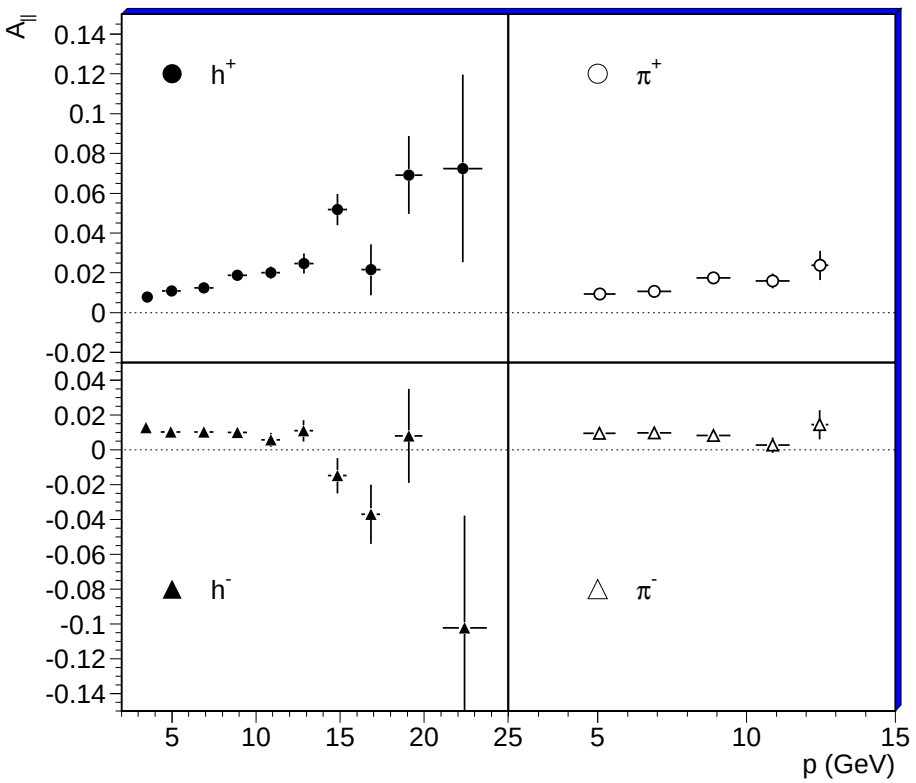

Figure 3.28: The asymmetries versus p. The positive hadron asymmetry is corrected for positron contamination. The errors are as in 3.27.

and then added in quadrature to the correlated systematic errors.

$$\left(\frac{\Delta A_{\parallel}}{A_{\parallel}}\right)^2_{sys} = \left(\frac{\Delta P_B}{P_B}\right)^2_{rise} + \left(\frac{\Delta P_T}{P_T}\right)^2_{97} + \left(\frac{\Delta P_B}{P_B}\right)^2_{point} + \left(\frac{\Delta P_T}{P_T}\right)^2_{norm}, \tag{3.24}$$

where $\left(\frac{\Delta P_T}{P_T}\right)^2_{97}$ is the part of the target polarization error arising from the target calibration scheme used in 1997. This error is common to both years because of the normalization procedure of the 1996 polarization described in the previous section and $\left(\frac{\Delta P_T}{P_T}\right)^2_{norm}$ is the error of the normalization factor for 1996. The exact values of the statistical and systematic errors are shown in tables 3.2 to 3.5.

p_T-Bin	h^+			π^+		
	$A_{\|\|}$	$\pm$ stat	$\pm$ sys	$A_{\|\|}$	$\pm$ stat	$\pm$ sys
1	0.0109	0.0013	0.0006	0.0083	0.0017	0.0005
2	0.0125	0.0014	0.0007	0.0126	0.0018	0.0007
3	0.0156	0.0021	0.0009	0.0119	0.0026	0.0007
4	0.0177	0.0031	0.0011	0.0176	0.0039	0.0010
5	0.0397	0.0062	0.0024	0.0428	0.0083	0.0026
6	0.0496	0.0126	0.0030	0.0428	0.0177	0.0025
7	0.118	0.023	0.007	0.0737	0.0356	0.0043
8	0.116	0.052	0.007	0.0656	0.0945	0.0037
9	0.205	0.079	0.012	0.0079	0.2062	0.0005

Table 3.2: The asymmetries for h^+ (π^+) vs. p_T.

p_T-Bin	h^-			π^-		
	$A_{\|\|}$	$\pm$ stat	$\pm$ sys	$A_{\|\|}$	$\pm$ stat	$\pm$ sys
1	0.009	0.0015	0.0006	0.0057	0.0019	0.0003
2	0.0113	0.0017	0.0007	0.0113	0.0020	0.0007
3	0.0083	0.0026	0.0005	0.0103	0.0030	0.0006
4	0.0096	0.0040	0.0006	0.0112	0.0045	0.0007
5	0.0153	0.0078	0.0009	0.0211	0.0092	0.0013
6	-0.0160	0.0156	0.0010	-0.016	0.019	0.001
7	-0.0739	0.0295	0.0044	-0.053	0.039	0.003
8	0.120	0.066	0.0072	-0.018	0.104	0.001
9	-0.123	0.108	0.0073	-0.243	0.280	0.014

Table 3.3: The asymmetries for h^- (π^-) vs. p_T.

p-Bin	h^+			π^+		
	$A_{\|\|}$	$\pm$ stat	$\pm$ sys	$A_{\|\|}$	$\pm$ stat	$\pm$ sys
1	0.0078	0.0022	0.0005			
2	0.0109	0.0013	0.0007	0.0093	0.0016	0.0006
3	0.0125	0.0016	0.0007	0.0108	0.0019	0.0006
4	0.0188	0.0023	0.0011	0.0174	0.0026	0.0010
5	0.0202	0.0033	0.0012	0.0159	0.0038	0.0010
6	0.0247	0.0050	0.0015	0.0237	0.0074	0.0014
7	0.0518	0.0079	0.0031			
8	0.0215	0.0128	0.0013			
9	0.0692	0.0196	0.0041			
10	0.0724	0.0472	0.0043			

Table 3.4: The asymmetries for h^+ (π^+) vs. p.

p-Bin	h^-			π^-		
	$A_{\|\|}$	$\pm$ stat	$\pm$ sys	$A_{\|\|}$	$\pm$ stat	$\pm$ sys
1	0.0127	0.0029	0.0007			
2	0.0102	0.0015	0.0006	0.0094	0.0018	0.0006
3	0.0102	0.0020	0.0006	0.0096	0.0021	0.0006
4	0.0099	0.0028	0.0006	0.0083	0.0030	0.0005
5	0.0057	0.0040	0.0003	0.0026	0.0043	0.0002
6	0.0109	0.0062	0.0007	0.0144	0.0084	0.0009
7	-0.0149	0.0101	0.0009			
8	-0.0370	0.0170	0.0022			
9	0.0080	0.0270	0.0005			
10	-0.102	0.0645	0.0061			

Table 3.5: The asymmetries for h^- (π^-) vs. p.

Chapter 4

Results and Interpretation

4.1 Further Studies on the Charged Hadron Asymmetries

In the previous chapter, several systematic checks on the charged hadron asymmetries of both 1996 and 1997 were described which showed their stability with respect to changes in the experimental conditions, PID calibrations etc. The HERMES data are consistent with those of the SLAC E155 experiment [Ant99], as is shown in figure 4.1.

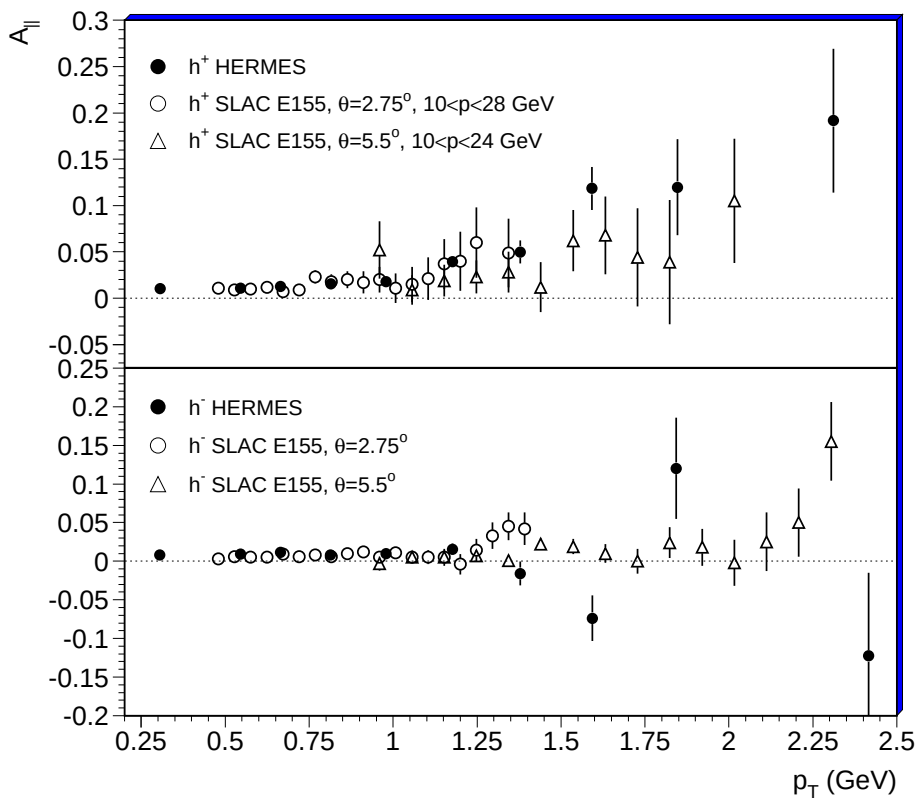

Figure 4.1: The inclusive charged hadron asymmetries on hydrogen. The data from HERMES are from1996 and 1997. Note that, as opposed to HERMES where p and θ are integrated to give p_T, E155 measured at fixed angles 2.75° and 5.5°.

4.1.1 Invariant Mass

It has been argued that the HERMES photoproduction data will be overwhelmingly dominated by contributions from resolved photon processes, mainly VMD (see section 1.2.3.). A VMD process often results in the production of a vector meson (ρ^0, φ) or a nonresonant, but correlated $q\overline{q}$ state. These states decay into rather low mass h^+h^--pairs which in the case of the vector meson decays $\rho^0 \to \pi^+\pi^-$ and $\varphi \to K^+K^-$ form a peak around the invariant mass of 0.77 GeV and 1.02 GeV respectively. The φ can also decay into $K^0_L K^0_S$, in which case a peak at 0.5 GeV can be seen coming from $K^0_S \to \pi^+\pi^-$. Figure 4.2 shows the invariant mass distribution for hadrons with $p_T > 0.5$ GeV, with the assumption that $m_h = m_\pi$. Clear peaks can be seen at the ρ and K^0_S masses. With higher p_T-cuts, the significance of the peaks becomes less, although they do not completely vanish except for the highest $p_T > 2$ GeV. It might be possible to reduce the contribution from VMD to

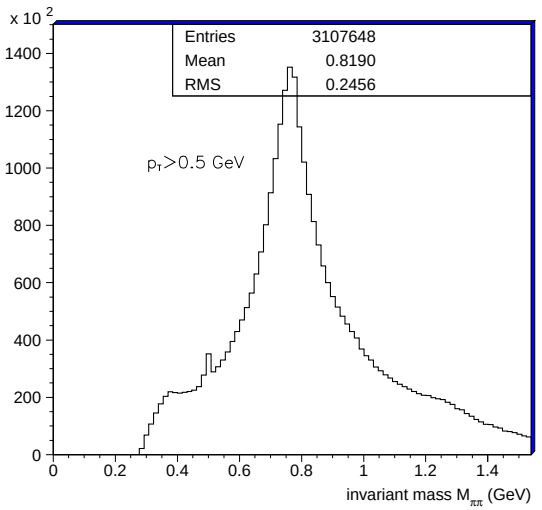

Figure 4.2: The invariant mass of a $\pi^+\pi^-$-system assigned to hadrons coming from events with at least two oppositely charged hadrons. Of the 9.1 million hadrons with $p_T > 0.5$ GeV about 3.1 million come from events where such an invariant mass could be calculated.

the asymmetries by excluding the resonance region below $M = 1$ GeV. Under the assumption that both hadrons are pions, the invariant mass peak of the K^+K^- from the φ will be reconstructed at values below 1 GeV. For the comparison in figure 4.3 the invariant mass $M_{\pi\pi}$ of each h^+h^- in an event was calculated with a pion mass assumption. Compared are the asymmetries where there was a hadron pair with $M_{\pi\pi} < 1$ GeV in the event to those where no such pair was found. Apart from the change in statistics no significant difference between the asymmetries can be seen. If the part of the asymmetry coming from VMD is zero[1], one could expect the asymmetry with $M_{\pi\pi} > 1$ GeV to be higher than the one with $M_{\pi\pi} < 1$ GeV because the latter would have a larger dilution from VMD. On the other hand, if the VMD asymmetry $A_{\|}^{VMD}$ was nonzero, then at least it should be the same for both charges. This is definitely not the case for $p_T > 1$ GeV, as can be seen when comparing the asymmetries with $M_{\pi\pi} < 1$ GeV for h^+ and h^-. Of course the cut on $M_{\pi\pi} > 1$ GeV is a rather crude estimate, it could well be that the invariant mass region for the resolved photon processes extends to much higher values or that within the HERMES acceptance a VMD process is only partly correlated to the detection of a h^+h^- pair. Whether $A_{\|}^{VMD} \neq 0$ in the photoproduction regime is presently unknown and still needs to be investigated.

4.1.2 Sensitive Kinematic Regions of the Asymmetries

From the comparison of the asymmetries for identified pions with those for all hadrons (cf. figure 3.9), and also from comparing the E155 data with those from HERMES (figure 4.1) it becomes clear that the asymmetry does not only depend on p_T but also on an additional kinematic variable like p or θ. With the statistics available so far it is not possible to calculate double differential

[1] First results from an analysis performed by K.Negodaeva on the asymmetry of photoproduced ρ^0s indeed indicate that it is zero.

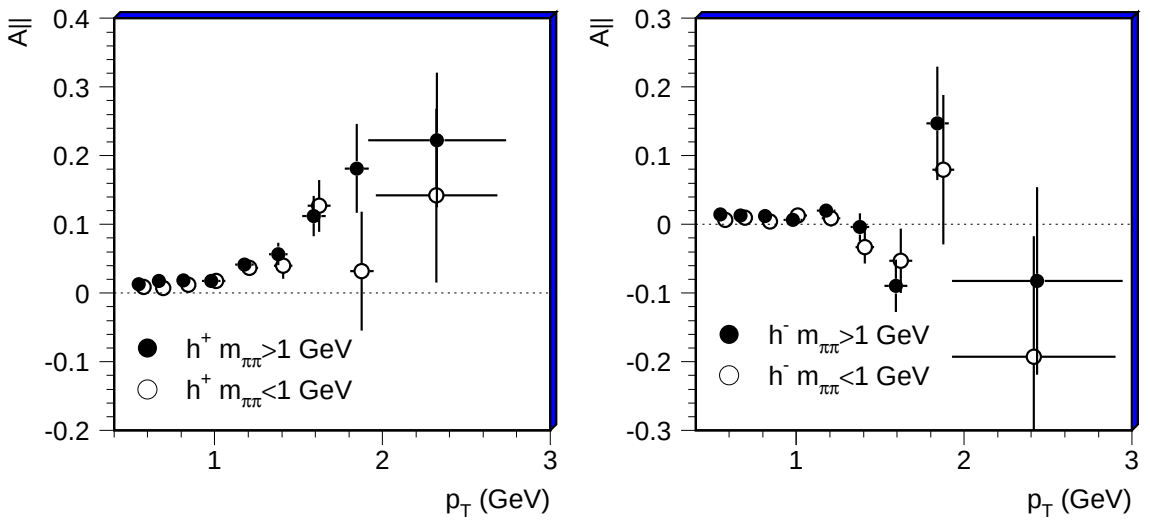

Figure 4.3: Comparison of the charged hadron asymmetries with cuts on the invariant mass $M_{\pi\pi}$ lower and higher than 1 GeV. The invariant mass was only calculated for oppositely charged hadrons. If no such hadrons were found, the event was accepted for the asymmetry with $M_{\pi\pi} > 1$ GeV.

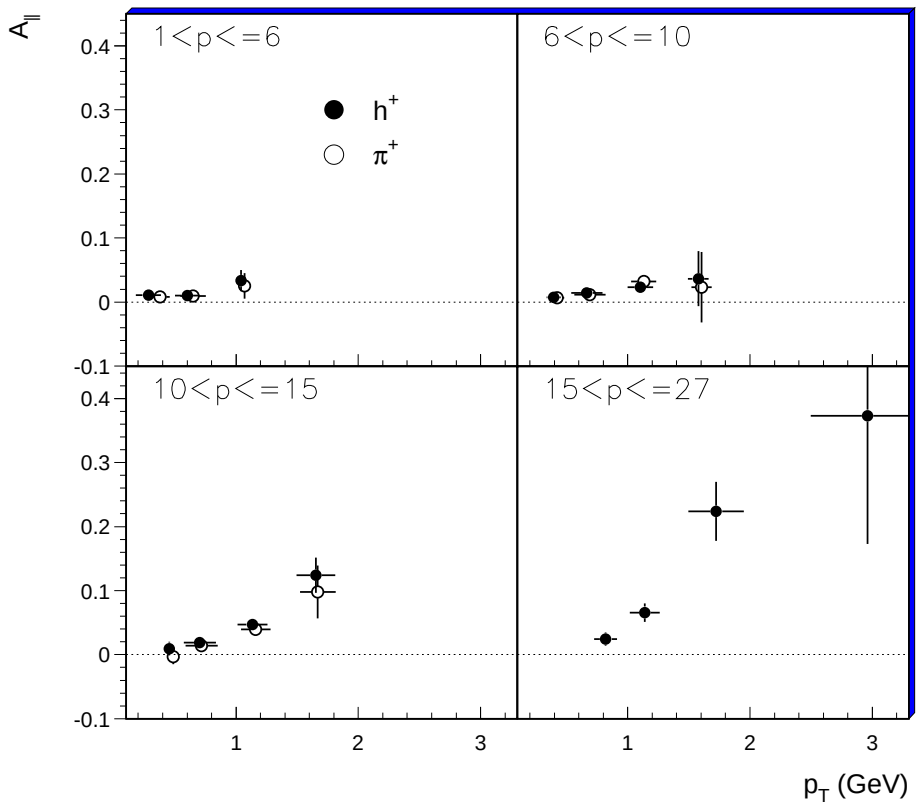

Figure 4.4: The inclusive positive hadron asymmetry vs. p_T in four momentum bins. The error bars are statistical only. The asymmetry has not been corrected for e^+ contamination, which is 1% at maximum in the two highest p_T-bins at $15 < p < 27$ GeV. The bins in p_T are: 0 to 0.5, 0.5 to 1, 1 to 1.5, 1.5 to 2.5 and 2.5 to 5 GeV.

asymmetries as in the case of the inclusive DIS asymmetry. Nevertheless, the asymmetry was calculated with a reduced binning in p_T but additional bins in p. The momentum range of 1 to 27

GeV was split into four bins, while p_T was subdivided into five bins including the bin from 0 to 0.5 GeV. The results of this double binning is shown in figures 4.4 and 4.5 for positive and negative hadrons respectively.

The positive hadron asymmetry clearly becomes much more significant with growing momentum

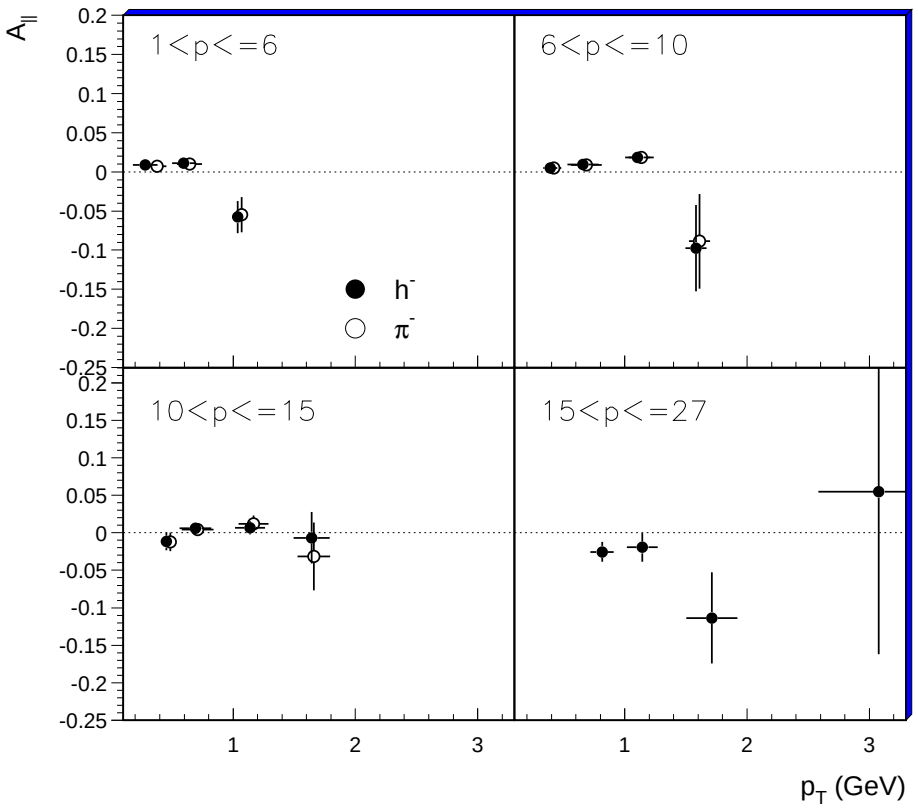

Figure 4.5: The inclusive negative hadron asymmetry vs. p_T in four momentum bins. The error bars are statistical only. The binning is the same as for the positive hadrons.

for $p_T > 1$ GeV. The negative hadron asymmetry seems to be subdivided into two regions of phase space where it becomes negative, the region below $p = 10$ GeV and that with p above 15 GeV. Theoretical predictions of [Afa98] are that $A_{||}$ may change sign, so the region from 10 to 15 GeV might turn out to be a transition region. On the other hand, detector effects cannot be excluded completely. In the one-dimensional h^- asymmetry vs. p_T there was a jump to positive values in the bin with p_T between 1.75 and 2 GeV. Shifting the bins a little or cutting away statistics (as for the invariant mass cuts) did not affect the jump. It is very questionable that this is only a statistical fluctuation which should change when statistics are changed but rather points to a not yet known systematic effect in the detector. This issue needs to be investigated further.

A binning in p and p_T of course restricts the θ-range probed, because $p_T = p \sin\theta$. The average θ rises with p_T in each momentum bin but falls with momentum for each p_T. Still the overlap in θ between adjacent p_T bins is quite large. Another possibility to study the variation of $A_{||}$ would be for instance to plot it versus θ with a cut on $p > 10$ GeV and $p_T > 1$ GeV, where a significant asymmetry is seen for positive hadrons. This was done using three bins in θ with the results shown in figure 4.6. Surprisingly, the asymmetries do hardly depend on θ despite the fact that the average p_T goes up with increasing θ. That the negative hadron asymmetry is zero might be understood from the fact that between 10 and 15 GeV it is also zero when plotted vs. p_T (cf. figure 4.5). The positive hadron asymmetry is also lower than one might expect when averaging over the two highest momentum bins in figure 4.4. The reason for this may become clear when

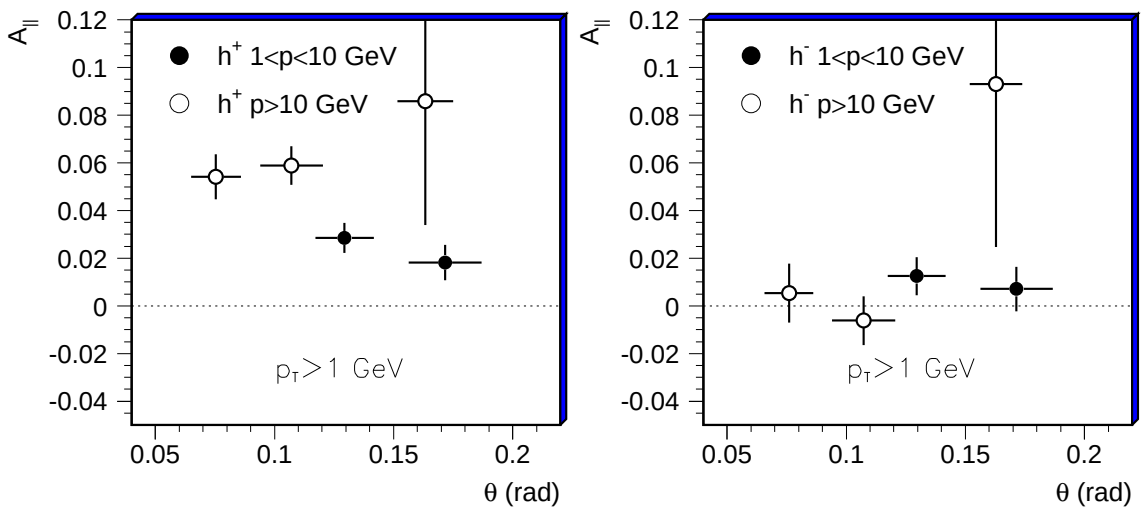

Figure 4.6: Positive and negative hadron asymmetries vs. θ, with a cut on $p_T > 1$ GeV and $p < 10$ GeV or $p > 10$ GeV. The bins in θ used are: 0.04 to 0.09 rad, 0.09 to 0.15 rad and 0.15 to 0.22 rad.

looking at figures 4.7 and 4.8, where the distributions of p_T and θ are shown for the two cases (binning in θ and binning in p_T), respectively. The figures show that with each binning 'mode'

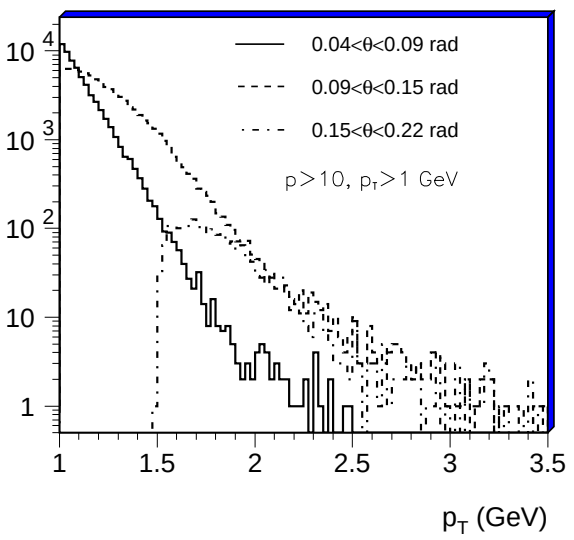

Figure 4.7: The p_T distribution for the asymmetry binned in θ with $p > 10$ GeV and $p_T > 1$ GeV.

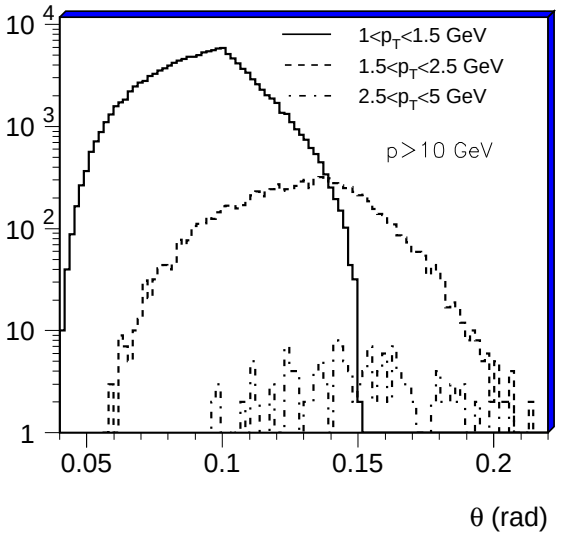

Figure 4.8: The θ distribution for the asymmetry binned in p_T with $p > 10$ GeV and $p_T > 1$ GeV.

a different data sample is selected. The θ-binning in figure 4.7 introduces a lower cutoff in p_T resulting in a growing average p_T. On the other hand 4.8 shows that the θ-distributions of the p_T-bins overlap to a large degree. Thus, for the same average p_T in both asymmetries, the average momentum of the hadrons will be higher when binning is done in p_T, because smaller angles are allowed.

The previous considerations suggest that the two variables to which $A_{||}$ is most sensitive to are p, which is also related to ν, and p_T, to which a correlation to the scale of the hard process may be expected.

4.1.3 Q^2 dependence of the Asymmetries

As described in section 1.2.3., the measured asymmetry in quasi-real photoproduction comes from an admixture of different processes, among them also the subprocess $\gamma^* q \to q$ underlying the DIS process. A subprocess asymmetry coming from this type of events would always be sensitive to the polarization of the quarks. Of course this virtual photoabsorption process can happen at much lower Q^2 than $Q^2 > 1$ GeV^2, the cut normally used in HERMES analyses on inclusive and semi-inclusive DIS. The cut used in this analysis, to reject every event with a positron in the detector, can thus not exclude the contribution from DIS. It can only help to reduce the 'contamination' from events with higher Q^2, which are more likely to come from scattering off a quark. In section 3.4.1. a comparison of the asymmetries calculated with this cut to the ones where the cut was released to also include hadrons from semi-inclusive events is shown (cf. figure 3.15). The results of a more detailed study are presented in figure 4.9. The top two plots show the relative deviations

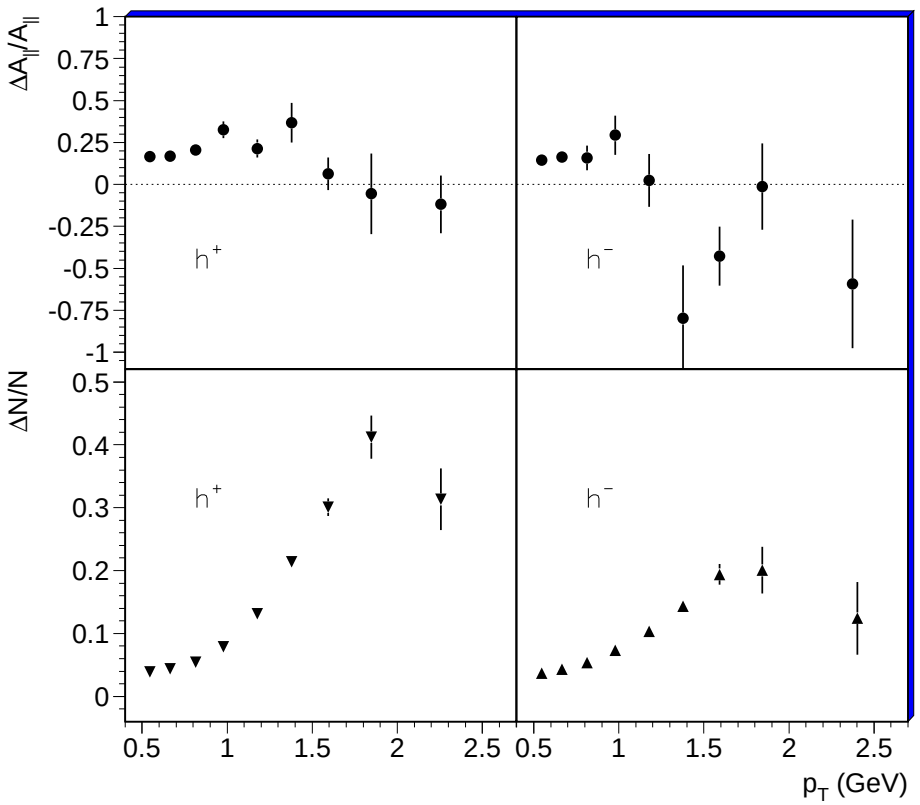

Figure 4.9: The relative deviation $\Delta A_{||}/A_{||}$ of the of the totally inclusive asymmetry to the standard one used for the analyses (top), and the relative increase in the statistics $\Delta N/N$ for the totally inclusive asymmetry (bottom).

$\Delta A_{||}/A_{||}$ of the totally inclusive asymmetry $A_{||}^{inc}$ which contains all events, from the standard one, $A_{||}^{std}$, with the high-Q^2 events cut out. The bottom row shows the relative difference in the yields per p_T-bin. $\Delta A_{||}/A_{||}$ and its error are calculated as follows [Gär00]:

$$\frac{\Delta A_{||}}{A_{||}} = \frac{A_{||}^{inc} - A_{||}^{std}}{A_{||}^{std}}; \qquad \delta\left(\frac{\Delta A_{||}}{A_{||}}\right) = \frac{\sqrt{|\sigma_{inc}^2 - \sigma_{std}^2|}}{|A_{||}^{std}|}. \tag{4.1}$$

If the compared asymmetries were to be consistent, meaning that they contain the same physics, the data points would be allowed to move according to the (relative) change in statistics. This change is represented in $\Delta N/N = (N^{inc} - N^{std})/N^{std}$. For $p_T < 1$ GeV, the increase in statistics

is about 5% to 10% for both charges, while the inclusive asymmetry is 20% to 30% higher. The fraction of high-Q^2 events is clearly increasing with p_T, at high p_T it is about a factor two higher for positive than for negative hadrons. Despite this fact, the asymmetry for positive hadrons remains unchanged for $p_T > 1.5$ GeV, whereas for negative hadrons the inclusive asymmetry rapidly changes towards less negative values between 1 and 1.5 GeV, even when considering the error bars. At low p_T the changes are the same for both charges. These observations may be interpreted as follows:

- It is very likely that a u quark was struck if a positive hadron or pion is detected, because the hadronization of a $u \to \pi^+(u\overline{d})$ goes via the 'favored' fragmentation function. Since both QCDC and LO DIS are sensitive to $\Delta q/q$, the similarity of the positive hadron asymmetries may be due to the fact that both processes measure $\Delta u/u$. Even if DIS would be suppressed at low Q^2 and high p_T, the asymmetry would then still be dominated by QCDC.

- The fewer statistics from high-Q^2 events for the negative hadrons as opposed to the positive ones may be explained by the ratio $e_d^2/e_u^2 = 1/4$, the suppression factor for scattering off a d-quark instead off a u-quark. If a d-quark is struck, it is likely to fragment into a negative hadron or pion - this would again be due to the 'favored' fragmentation function. On the other hand, from the HERMES semi-inclusive analysis it is known that even when detecting a negative pion it is more likely that it comes from a u-quark than from a d-quark [Ack99]. This is due to the u-quark dominance in the proton, which even enhances the 'unfavored' fragmentation function for $u \to \pi^-(\overline{u}d)$. For semi-inclusive negative pions the asymmetry is positive vs. x, whereas $\Delta d/d$ is negative. If the asymmetry would turn to negative values in the quasi-real photoproduction regime even when quark scattering (DIS or QCDC) is still dominant, it must be because the ratio of 'favored' to 'unfavored' fragmentation functions changes.

- Provided that the gluon polarization is positive, any asymmetry sensitive to that should be negative (cf. section 1.2.3.). If the negative hadron asymmetry at high-p_T and low-Q^2 would be sensitive to $\Delta G/G$, the fact that it is less negative at high-Q^2 would point to an enhanced contribution of PGF to the low Q^2 cross section.

To clarify these and the other questions raised above it is necessary to perform Monte Carlo studies with respect to the contribution of processes in different kinematic regimes and the fragmentation processes in the photoproduction limit.

4.2 Comparison of the Data with Different Theoretical Models

4.2.1 Theoretical Calculations

According to their method described in [Afa99], Afanasev et al. calculated asymmetries for the HERMES kinematic region, with a beam energy of 27.5 GeV and at $\theta = 12°$. They also calculated the cross sections for each of the different subprocesses. The results are presented in figure 4.10.
'Fragmentation' processes in the notation used by this group are the direct processes in the notation of this thesis (PGF and QCDC). The 'direct' process in their notation is a so-called 'isolated', or 'short range' process, where the scattered quark does not fragment but forms a hadron via a short range interaction. The diagram for this process is shown in figure 4.11. According to [Afa99] the nonzero asymmetry at $p_T > 2$ GeV is entirely due to quark polarization. At these high p_T values the 'direct' process is dominant, which is sensitive to $\Delta q/q$ like QCDC. The sensitivity of $A_{||}$ to $\Delta G/G$ at $1 < p_T < 2$ GeV is washed out by a large dilution from VMD, whose asymmetry is assumed to be zero. Especially when looking at the negative hadron asymmetry one can see that there are quite large deviations for the different polarized parton distributions used. If the model of Afanasev et al. proves to be consistent with the data, it might be possible to narrow down the possible sets of polarized quark distributions. The signs of both asymmetries agree with the

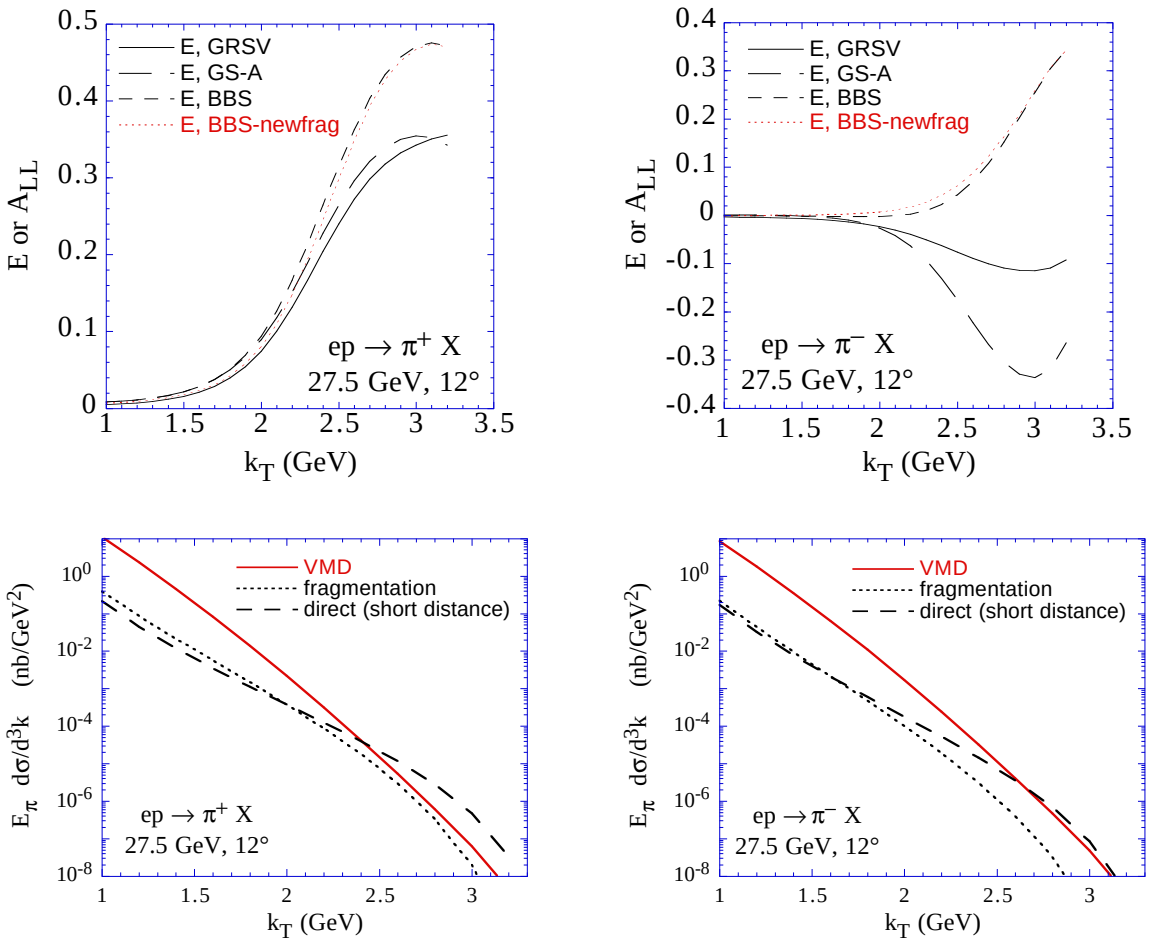

Figure 4.10: Theoretical calculations for $A_{||}$ from Afanasev et al. The top left is $A_{||}$ for positive pions, the top right is the same for negative pions. The bottom shows the corresponding cross sections for the subprocesses. The various curves for the asymmetries are for different input parton distributions (which ones have been used is described in [Afa99]).

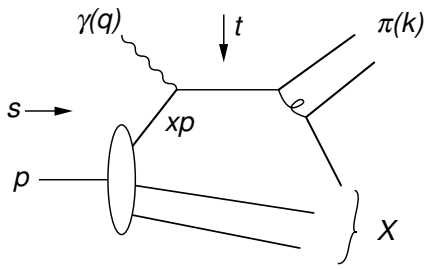

Figure 4.11: The 'direct' process in the notation of [Afa98]. Here the quark does not undergo a fragmentation, but forms a pion via a short range process.

data, when the one-dimensional asymmetries are considered. Unfortunately it is very difficult to actually compare the shapes of the asymmetries because the $\theta = 0.2$ rad is just the upper limit of the HERMES acceptance. For comparison, in figure 4.12 the asymmetries are plotted vs. p_T in a θ-range from 0.16 to 0.22 rad. Within the statistical error bars these asymmetries are consistent with the theory in the range $1 < p_T < 2$ GeV. For $p_T > 2$ GeV, where the start of a nonzero

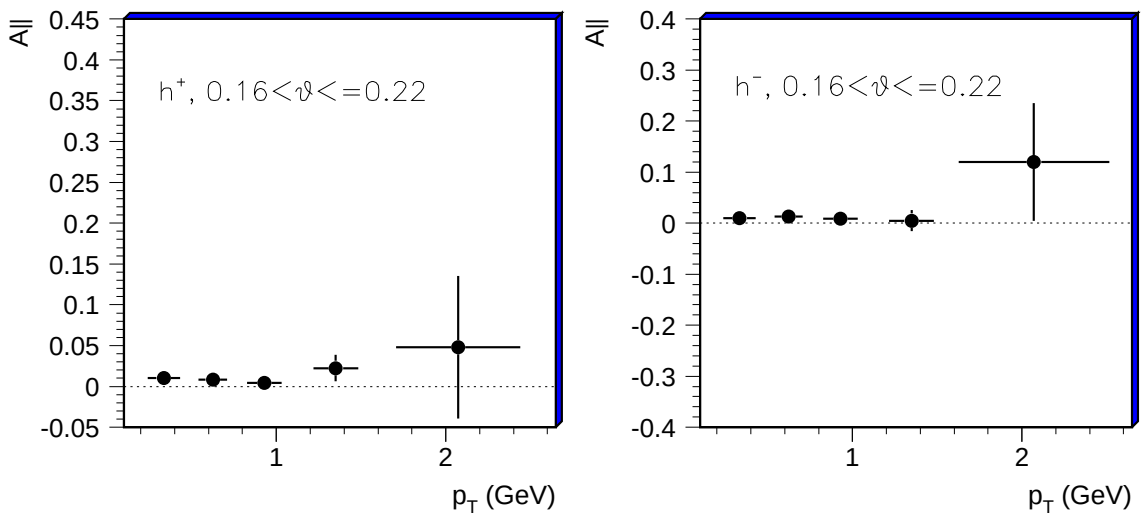

Figure 4.12: Asymmetries for positive and negative hadrons vs. p_T, calculated for $0.16 < \theta < 0.22$ rad. The bins in p_T are 0 to 0.5, 0.5 to 0.8, 0.8 to 1.2, 1.2 to 1.8 and 1.8 to 5 GeV.

asymmetry is seen in the calculations, no statistics is available in the present data sample. For this restricted θ-range thus no conclusion can be made, until the data of the years 1998 to 2000 are analyzed.

4.2.2 Monte Carlo Simulations

For the Monte Carlo studies the PYTHIA 6.1 generator was used. This new version of PYTHIA includes an option to generate $\gamma^* p$ events according to the model described in [Sjö00]. Their approach is to mix the processes that contribute to the total $\gamma^* p$ cross section in such a way, that a smooth transition from real to virtual photons is achieved. The parametrization used for this model is described in [Fri00], see also section 1.2.3. It includes a Q^2-dependent mixture of processes like VMD and GVMD (generalized VMD, an intermediate process between VMD and the anomalous photon), the direct photon processes and DIS. Apart from small modifications in some parameters, this model will be used for the studies of the fractions of processes for the quasi-real photoproduction of hadrons. The default settings for kinematic cutoffs, fragmentation parameters and the cuts used for the classification of events have been tuned to fit data from LEP and TEVATRON with c.m. energies of a few hundred GeV. It can be expected that some of these values cannot be used in the analyses at HERMES energies. The tuning of the parameters is still ongoing, and only first results can be presented here. It is essential for the tuning to get the shapes of the p_T and p distributions of hadrons in agreement with the data. As described in section 1.2.3, the p_T distribution is sensitive to several quantities such as the p_T width in the string fragmentation, the fraction of each subprocess, the intrinsic k_T of the proton *and* the photon. Some of the settings used for this study are shown below.

MSTP(58)=3	maximum number of quark flavors used for parton distributions
MSTP(14)=30 and MSEL(1)=2	use full mixture of processes for $\gamma^* p$
MSTP(15)=5	use larger p_{Tmin} (minimum p_T) for anomalous component than for VMD; $p_{Tmin} = 1$ GeV
PARP(15)=0.5 GeV	cut on k_T used to separate VMD and GVMD processes; minimum p_T for direct processes
PARP(91)=0.44 GeV	primordial k_T of the proton (Gaussian width)
PARP(99)=0.44 GeV	primordial k_T of the photon (Gaussian width)
PARP(111)=1 GeV	minimum invariant mass of the remnant hadronic system, after the interacting partons have been taken away
PARJ(21)=0.4 GeV	width of the p_T-distribution of the primary hadron in string fragmentation
PARJ(33)=0.27 GeV	minimum energy for which the fragmentation of a jet system is stopped
PARJ(41)=1	parameter a for the LUND symmetric fragmentation function
PARJ(42)=0.7	parameter b for the LUND symmetric fragmentation function

The LUND symmetric fragmentation function gives the probability density that a hadron with given z will be produced in the fragmentation process:

$$f(z) \propto z^{-1}(1-z)^a \exp\left(-\frac{b\, m_T}{z}\right) \qquad \text{with } m_T^2 = m_q^2 + p_T^2.$$

The parameters a and b are free, and p_T here represents the Gaussian width of the fragmentation. Several features that are only relevant at higher energies like QCD initial- and final state radiation and multiple interactions have been turned off. The parton distributions used are the 'CTEQ set 1 MS' for the proton and 'SaS 1D' (PYTHIA default) for the photon.

In principle with the HERMES Monte Carlo software it is possible to simulate the tracking and particle identification features of the spectrometer. At the moment, however, only a cut on the box acceptance of the detector and a lookup table for the momentum dependent acceptance of the spectrometer magnet is being used. This should be a good approximation, although for a final study also corrections for efficiencies and smearing as well as radiative corrections have to be applied. For the comparison of the distributions, a cut on $p > 3$ is applied in order to avoid effects from the reduced detector efficiency for low momentum hadrons (e.g. the calorimeter threshold of 1.4 GeV for trigger 21 - which translates into a threshold of $\simeq 3$ GeV for a hadron). Both the Monte Carlo and the data sample are required to have no positron in the acceptance. For HERMES it is known that 1 million DIS positrons which fulfill certain kinematic cuts ($Q^2 > 1$ GeV^2,$W^2 > 4$ GeV^2, $y < 0.85$) correspond to an integrated luminosity of 21.8 pb^{-1}. The number of DIS positrons found in a certain time period can be used to normalize the data. The ratio of the number of hadrons to DIS positrons in PYTHIA 6.1 is about a factor of 2 too low compared to the data. The reason for this has not yet been investigated. Thus for now it is only possible to compare the shapes of the spectra. This is done by normalizing the area of each of the spectra to one. Figure 4.13 shows a comparison of the p_T and p spectra for the above settings.

The momentum distributions agree quite well with each other, which confirms the above statement that for $p > 3$ GeV effects from detection efficiencies at lower momenta are only small. The p_T distributions, on the other hand, clearly deviate from each other. The slope of the Monte Carlo distribution is steeper than that of the data, so that too few high-p_T hadrons are generated. As stated before, several quantities may have to be tuned to give the right p_T-slope. Some more checks showed that changing the fragmentation parameters within a reasonable range only results in small changes of the p_T-distribution, and this even only for $p_T < 1.5$ GeV. This is the same region in which the semi-inclusive data can be tuned for DIS Monte Carlo. Switching on and off the hard QCD subprocesses coming from the anomalous photon (such as $qg \to qg$) has a noticeable effect.

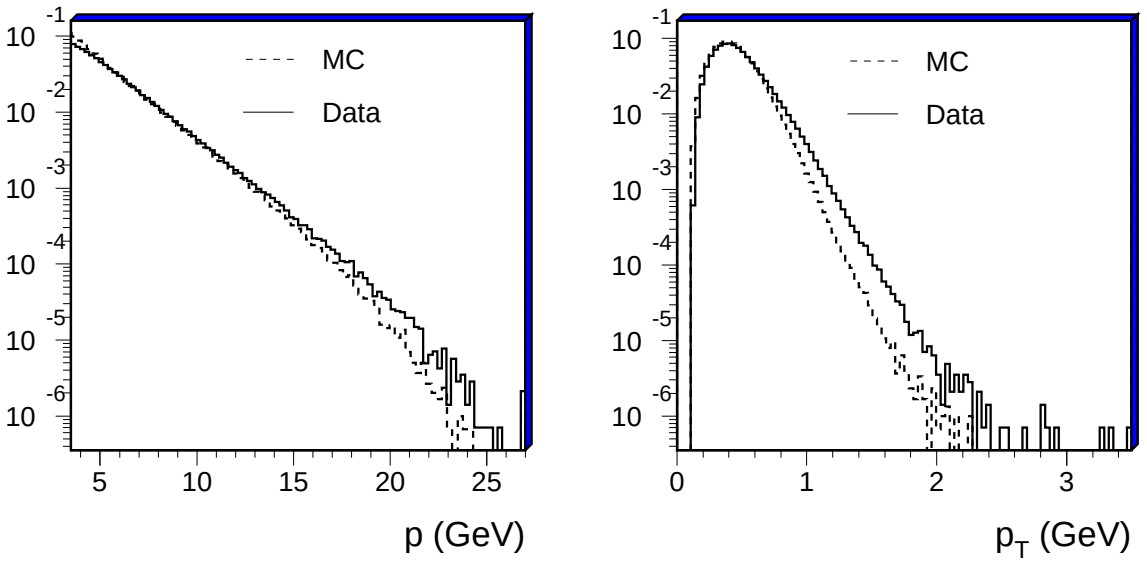

Figure 4.13: The normalized hadron distributions vs. p (left) and p_T (right) for data and Monte Carlo.

With these subprocesses turned on, the distribution is broadened in the region between 1 and 2 GeV. Hence, presumably also the mixture of processes needs to be tuned in order to reproduce the p_T-slope of the data.

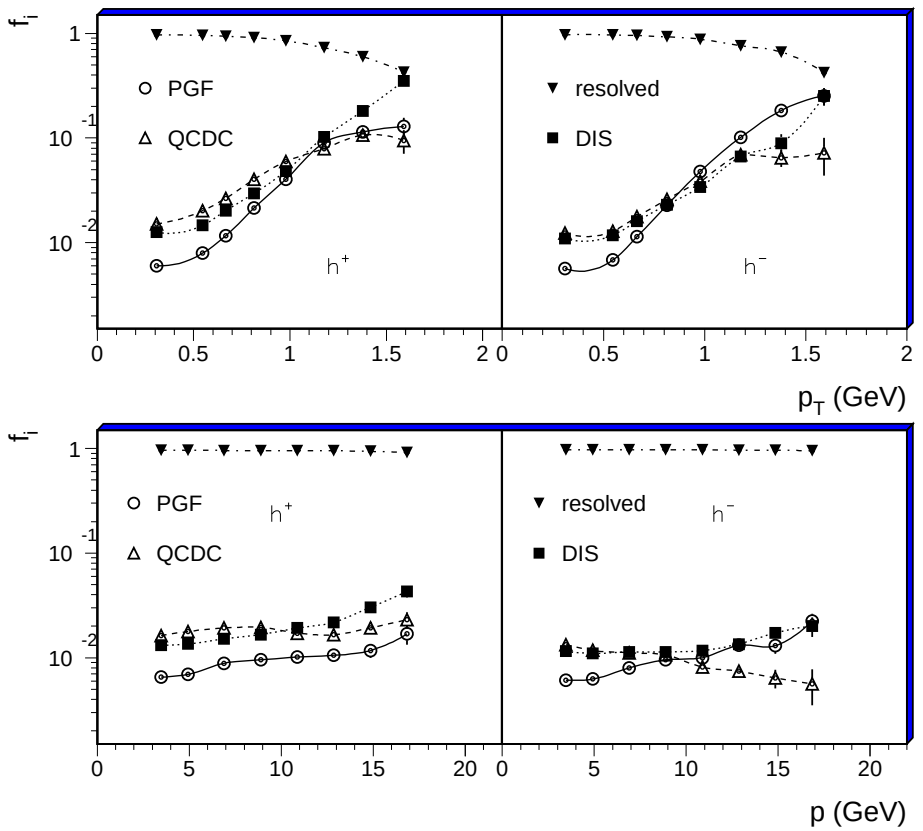

Figure 4.14: The fractions f_i of the different event classes for positive and negative hadrons vs. p_T and p. The same cuts as used in the data for the asymmetries are applied to select the hadrons. The binning is the same as for the one-dimensional asymmetries.

Figure 4.14 shows the fractions f of the different classes of processes versus p and p_T separately for positive and for negative hadrons. The direct class is divided into PGF and QCDC, the resolved photon class includes VMD and GVMD as well as non-diffractive, low-p_T processes and the anomalous photon ones. Although the exact composition of processes still needs to be tuned, some general features can already be inferred from these first results. As can be seen, the fractions of the direct class processes rises with p_T for both charges. The fraction of PGF is a little higher for negative hadrons than for positive ones. The fraction of DIS processes is about a factor of two larger than that of the direct ones, at high $p_T > 1.5$ GeV it becomes even larger than the fraction of the resolved photon processes. If this is true, then the high-p_T requirement for the hadron asymmetries may well suppress the resolved photon fraction, but not the DIS processes. The increase of the fraction of the higher-Q^2 events with p_T seen in figure 4.9 is compatible with these Monte Carlo predictions. The tail in the hadron p_T-distribution in $\gamma^* q \to q$ events, coming from the squared sum of the primordial k_T of the partons and from the fragmentation process would then overlap with the p_T coming from hard QCD subprocesses, because at the HERMES energies their p_T range is the same.

An increase in the significance was seen for the two dimensional asymmetries, when momentum cuts where used in addition to the bins in p_T (cf. figures 4.4 and 4.5). The same two dimensional binning was used in figures 4.15 and 4.16 for the Monte Carlo subprocess fractions.

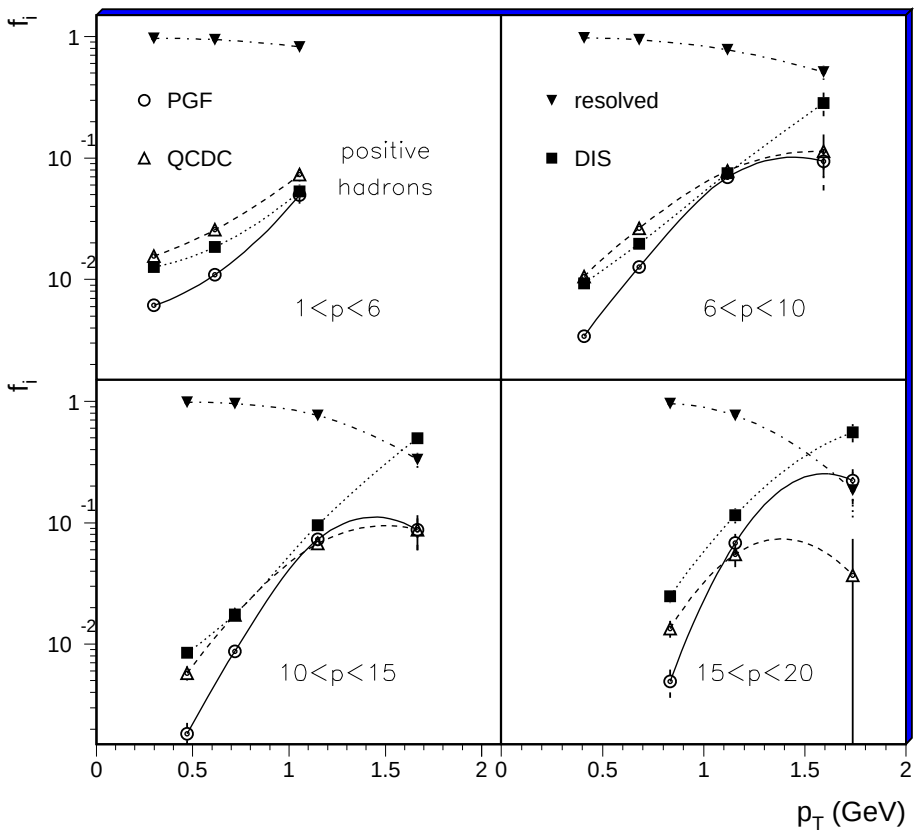

Figure 4.15: Fractions of subprocesses for positive hadrons with the same bins in p_T and p as used for the two dimensional asymmetries in figure 4.4.

For $p > 10$ GeV and $p_T > 1$ GeV the fraction of the resolved photon processes becomes smaller for both charges, but the decrease is more pronounced for the positive hadrons. The fractions of DIS and QCDC on the other hand are more suppressed for negative hadrons in the same kinematic region. The DIS subprocess is clearly the dominating one in this region for positive hadrons, which could account for the large positive asymmetry seen there (cf. figure 4.4).

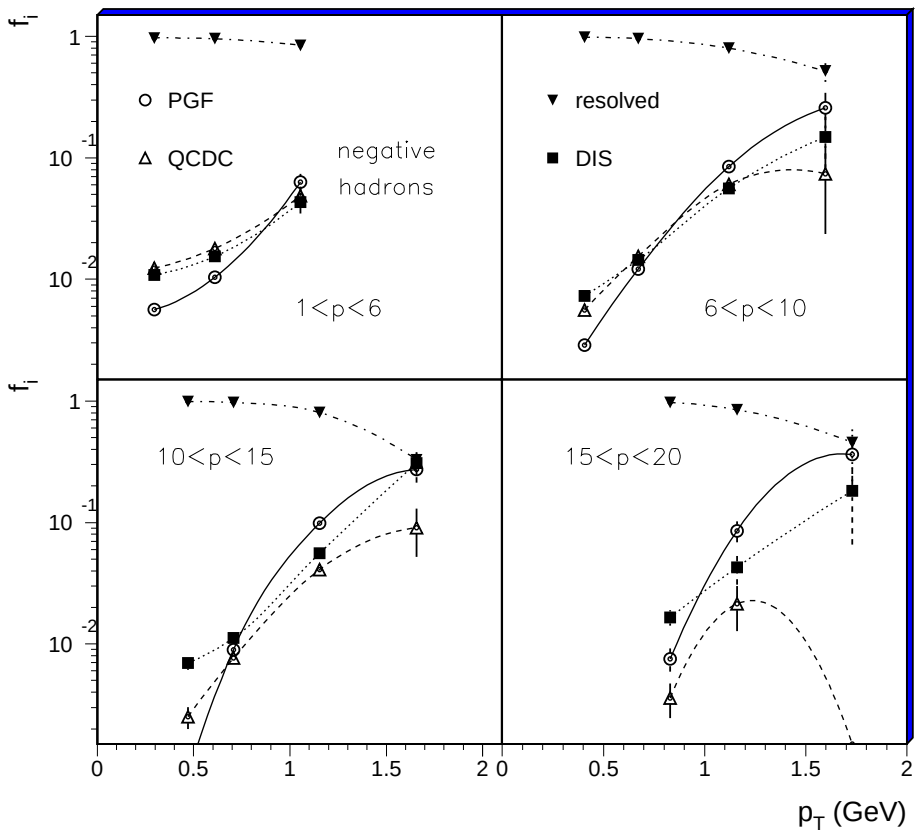

Figure 4.16: Fractions of subprocesses for negative hadrons with the same bins in p_T and p as used for the two dimensional asymmetries in figure 4.4.

With the present data it is only possible to perform consistency checks on the kinematic distributions and the normalized hadron multiplicities in order to find the right parameters for the Monte Carlo model. The sensitivity to cutoff parameters needs to be checked in particular. For example it was found that by lowering the minimum invariant mass of the remnant (PARP(111)) from the default of 2 GeV to 1 GeV, the cross sections for the direct processes increase by a factor of 2. The tuning of the fragmentation and cutoff parameters must be done with care in order to be able to describe the data consistently and finally to get reasonable answers for the photoproduction processes. Eventually further theoretical input will be needed to be able to interpret the data in the HERMES kinematic region.

Summary and Outlook

This thesis describes the analysis of spin asymmetries of single high-p_T hadrons in quasi-real photoproduction at HERMES. The analysis was done using data from 1996 and 1997 taken with a hydrogen target. A number of systematic checks were performed on the data. The results of both years were found to be stable with respect to the varying experimental conditions and to different selection criteria.
The asymmetries were calculated as functions of the transverse momentum and the momentum of the hadron. The results show that they are charge dependent, and deviate significantly from zero for $p_T > 1$ GeV. The positive hadron asymmetry rises with p_T to positive values, whereas the negative hadron asymmetry goes to negative, but less significant values for high-p_T. The shape and sign of the asymmetries is consistent with theoretical predictions. An essentially similar behavior is seen for the asymmetries when calculated as functions of momentum. The negative hadron asymmetry is clearly different from the semi-inclusive hadron asymmetry, which is positive for negative hadrons. The significance of the positive hadron asymmetries can be enhanced when both high momentum and high-p_T are required.

For the interpretation of the data in terms of the contribution of different processes to the cross section and to the asymmetries a thorough Monte Carlo study is needed. Here only first results of the comparison of p_T and p spectra could be presented, which essentially show that much more effort needs to be put into the tuning of the Monte Carlo parameters. The final goal is to find those parameters that describe the properties of the data. A consistent picture should be achieved that also includes the data on the high-p_T hadron pairs. The hadron pairs are in a sense a cleaner sample because the DIS process is much more suppressed when *two* high-p_T hadrons are required. On the other hand the statistics of single hadrons is superior to that of the pairs. Knowing the fractions of PGF and QCDC from a best fitting Monte Carlo model will give access to the quark- or gluon polarization. This holds for both the analyses on single and pairs of hadrons, provided that the statistical errors of the asymmetries and the theoretical uncertainties in the fractions are not too large. The current Monte Carlo settings predict an increase in the fraction of direct and DIS processes with increasing $p_T > 1$ GeV, the same region where the nonzero asymmetries are seen. However, there are still too many uncertainties in the Monte Carlo parameters and in the underlying theoretical model itself that no conclusion can be made so far, to what extent gluon and/or quark polarization is responsible for the hadron asymmetries.

Bibliography

[Ack98] K.Ackerstaff et al., The HERMES Collaboration, *The HERMES Spectrometer*, DESY 98-057, Nucl. Instr. Meth. **A 417** (1998) 230.

[Ack99] K.Ackerstaff et al., The HERMES Collaboration, *Flavor Decomposition of the Polarized Quark Distributions in the Nucleon from Inclusive and Semi-inclusive Deep-Inelastic Scattering*, Phys.Lett. B 464 123-134 ,(1999)

[Afa98] A.Afanasev,C.E.Carlson,C.Wahlquist*Measuring polarized Gluon and Quark Distributions with Meson Photoproduction*, Phys.Rev. D58(1998) 054007.

[Afa99] A.Afanasev,C.E.Carlson,C.Wahlquist*Soft Contributions to Hard Pion Photoproduction*, Phys.Rev. D61(2000) 034014.

[Air00] A. Airapetian et al., The HERMES Collaboration, *Measurement of the Spin Asymmetry in the Photoproduction of Pairs of High-pT Hadrons at HERMES*, Phys. Rev. Lett. 84 (2000) 2584-2588.

[Ama97] M.Amarian et al., *The HERMES Charm Upgrade Program: Measurement of the Double Spin Asymetry in Charm Leptoproduction*, Proposal to the DESY-HERA PRC, HERMES Internal Report 97-004 (1997).

[Ant99] P.L.Anthony et al., The E155 Collaboration, *Inclusive Hadron Photoproduction from Longitudinally Polarized Protons and Deuterons*, Phys.Lett.B 458, 536-544, (1999).

[Bai99] B.Bains, M.Beckmann, H.Ihssen, H.Kobayashi, M.McAndrew, M.Ruh, H.Tallini, *Determination of the charged hadron asymmetries from the 1997 data*, HERMES Internal Report 99-015 (1999).

[Bar94] D.P. Barber et al., *The First Achievement of Longitudinal Spin Polarisation in a High Energy Storage Ring*, Physics Letters B 343, 436-443, (1995).

[Bau98] C.Baumgarten, *The HERMES Internal Polarized Hydrogen and Deuterium Targets* Conference Proceedings of the 13th International Symposium on High Energy Spin Physics (SPIN 98), Protvino, Russia, Sep 8 - 12, (1998).

[Bec00] M.Beckmann, Extraction of Polarised Quark Distributions of the Nucleon from Deep *Inelastic Scattering at the HERMES Experiment*, Dissertation, Albert-Ludwigs-Universität Freiburg.

[Ben98] T.Benisch, *Polarisierte Bhabha-Streuung und Luminositätsmessung im HERMES Experiment*, Dissertation, Friedrich-Alexander-Universität Erlangen, (1998).

[Bra80] R. Brandelik et al., The TASSO Collaboration,*Evidence for a Spin One Gluon in Three Jet Events*, Phys.Lett. B 97, 453, (1980).

[Bra98] A. Bravar, D. von Harrach, A. Kotzinian, *Gluon Polarization from Correlated High p_T Hadron Pairs in Polarized Electroproduction*, Phys.Lett. B 421, 349-359, (1998).

[Fri00] C.Friberg, T.Sjöstrand, *Total Cross Sections and Event Properties from Real to Virtual Photons*, submitted to J. High Energy Phys., JHEP 0009,010, (2000).

[Gär00] Y.Gärber, *Messung des Strukturfunktionsverhältnisses $\frac{g_1^p}{f_1^p}$ bei kleinen Q^2 und Bjorken-x mit dem HERMES Experiment*, Dissertation, Humboldt-Universität zu Berlin, (2000).

[Geh96] T.Gehrmann, W.J.Sterling, Phys. Rev. D 53, 6100, (1996).

[Gup97] S.Gupta, P.Mathews, *J/Ψ Spin-Asymmetries in the Colour-Octet Model*, Phys. Rev. D55 (1997)

[Hal84] F.Halzen, A.D. Martin, *Quarks and Leptons: An Introductory Course in Modern Particle Physics*, Johm Wiley and Sons, New York, (1984).

[Hen00] M.Henoch, *The sampling correction on α_r for 1997*, HERMES Internal Report 00-004 (2000).

[Ing97] G.Ingelman, M.Thunman, *Signals for Intrinsic Charm in High Energy Interactions*, Z.Phys.C73:505-515, (1997).

[Jap99] G. Japaridze, W.-D. Nowak, A. Tkabladze, *Color Octet Contribution to J/ψ Photoproduction Asymmetries*, Phys.Rev. D 62(2000), 034022.

[Kai97] R.Kaiser, F.M. Menden, M.C.Vetterli, *Probabilty Analysis of the TRD Response and the Contribution of Flux Ratios to HERMES Particle Identification*, Internal Report 97-036 (1997)

[Kol98] H.Kolster, *The HERMES Gaseous Internal Polarized Proton Target and its use in the HERA Positron Storage Ring*, Dissertation, Ludwig-Maximilians-Universität Muenchen (1998).

[Mar00] J.W.Martin, *Measurement of the Spin Asymmetry $A_{||}$ in the Photoproduction of High-p_T Hadron Pairs*, Dissertation, Massachusetts Institute of Technology, Boston, (2000).

[Mei00] F. Meissner,*Measurement of the J/ψ Cross Section and Double-Spin Asymmetries in Vector Meson Production in Polarised Lepton-Nucleon Scattering at HERMES*, Dissertation, Humbolt-Universität zu Berlin (2000).

[Sjö00] T.Sjöstrand et al., *High-Energy-Physics Event Generation with PYTHIA 6.1*, hep-ph 0010017, (2000).

[Vet98] M. Vetterli, *The Spin Structure of the Nucleon*, Main Lectures at the Lake Louis Winter Institute, published in World Scientific, hep-ph/9812420, DESY 98-211

[Wen99] J.Wendland, *Improved Particle Identification at HERMES and Polarised Valence Quark Distributions in the Proton*, Thesis, Simon-Fraser-University (1999).